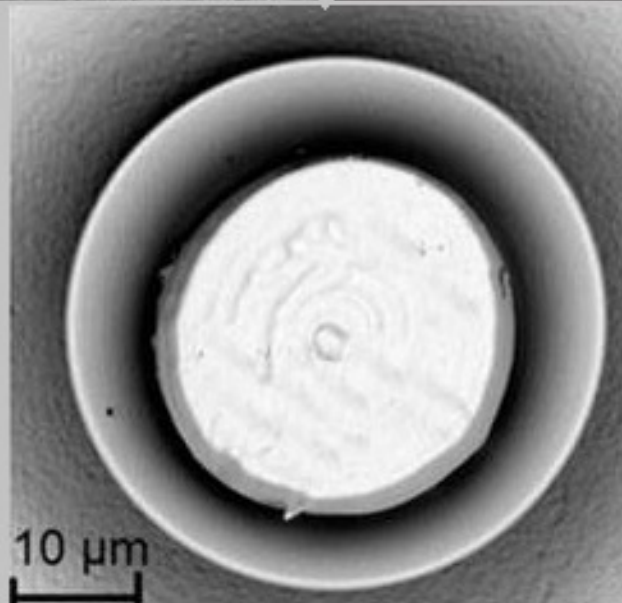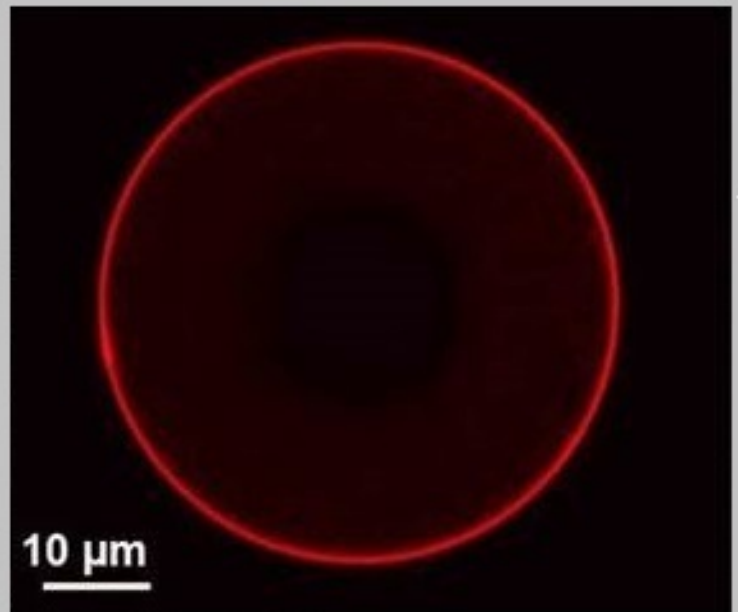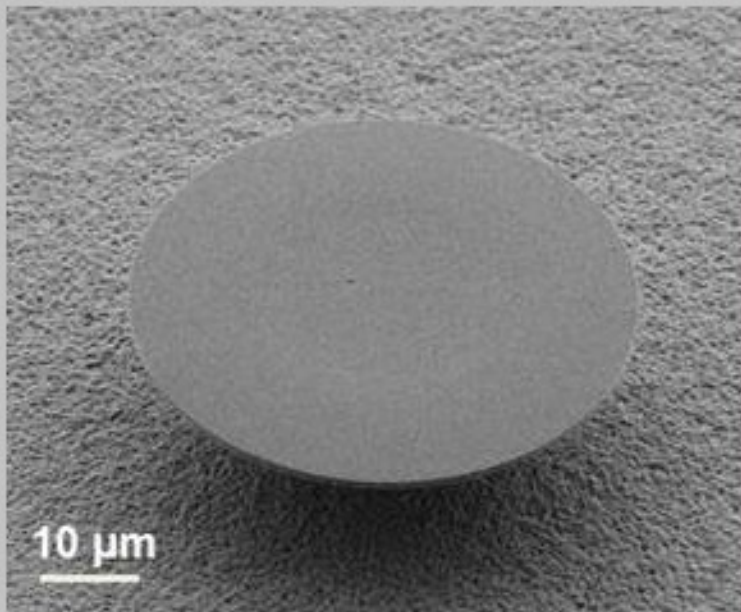# Active Polymeric Whispering Gallery Mode Resonators

Assegid Mengistu Flatae

Active Polymeric Whispering Gallery Mode Resonators

Zur Erlangung des akademischen Grades eines
DOKTORS DER NATURWISSENSCHAFTEN
von der Fakultät für Physik
des Karlsruher Instituts für Technologie (KIT)

genehmigte

DISSERTATION

von

M.Sc. Assegid Mengistu Flatae
aus Addis Ababa/Ethiopia

Tag der mündlichen Prüfung : 28.11.2014
Referent   : Prof. Dr. Heinz Kalt
Korreferent   : Prof. Dr. Diederik Wiersma

Declaration of Authorship

I, Assegid Mengistu Flatae declare that this thesis and work presented in it are my own and has been generated by me as the result of my own original scientific work. I confirm that, to the best of my knowledge, my thesis does not infringe upon anyone's copyright nor violate any proprietary rights. Any ideas, techniques, quotations, or any other material from the work of other people included in my thesis, published or otherwise, are fully acknowledged in accordance with the standard referencing practices.

Signed:
Assegid Mengistu Flatae

Date:

Prüfungskommission:

Prof. Dr. Heinz Kalt
Prof. Dr. Diederik Wiersma
Prof. Dr. Dieter Zeppenfeld
Prof. Dr. Gerd Schön
Prof. Dr. Francesco Cataliotti
Dr. Costanza Toninelli
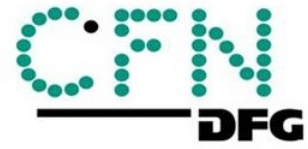
Karlsruhe Institute of Technology (KIT)
Institute of Applied Physics
Wolfgang-Gaede-Strasse 1
76131 Karlsruhe
http://www.aph.kit.edu/kalt

Assegid Mengistu Flatae
assegid.flatae@kit.edu

KSOP
Karlsruhe School of Optics & Photonics

CFN
DFG

Education and Culture DG
ERASMUS MUNDUS

euroPHOTONICS
ERASMUS MUNDUS

LENS
European Laboratory for
Non-Linear Spectroscopy

Contents

II

Chapter 1

Introduction

In the last few years small modal volume (high spatial confinement) and high quality factor (high temporal confinement) resonators have been studied for their potential applications as laser resonators [1], filters [2], modulators [3], bio-sensors [4] and for the fundamental study of cavity quantum electrodynamics (weak and strong coupling between emitters and cavity modes) [5, 6]. Different resonator geometries and light confining mechanisms have been developed for these studies, for instance, plasmonic cavities [7], Fabry-Perot cavities [8], distributed feedback resonators [9] and whispering gallery mode (WGM) resonators [10].

Because of their ultra-high intrinsic quality factor (Q-factor), their small modal volume, and their easy integration into on-chip devices, WGM resonators are well suited for all the applications and fundamental studies mentioned above. WGMs are specific eigenmodes (resonances) of the electromagnetic field circulating around a rotationally symmetric cavity surface by total internal reflection. After the light travels a complete trip around the cavity, it interferes with itself. The constructive interference (resulting in WGMs) is due to the returning of the light wave to the same point with the same phase (or multiple of 2π) and forms standing waves.

Recently, different techniques for the fabrication of high-Q WGM resonators have been developed. A surface-tension induced reflow (STIR) process (first demonstrated for silica microspheres [11,12]) leads to near-atomic smoothness of the surface of the cavity and low intrinsic losses resulting in ultra-long life times of the photons in the resonator. The STIR process of a silica microdisk on a silicon pedestal is accomplished by surface-normal irradiation of the disk resonator with a CO_2 laser [13]. Irradiating the microdisk with CO_2 laser of about 100 MW/cm^2 melts the silica. Due to surface tension the melted silica forms a smooth toroidal shape at the edge of the microdisk. The inner part of the disk is unaffected due to the fast heat transfer of

the silica to the silicon post, which exhibits a higher heat conductivity. The high CO_2 laser power used for STIR process produces high temperatures on the chip, which limits the integration of other optical components and quantum emitters. In addition, each resonator needs to be irradiated separately, which is time consuming and makes mass production quite difficult.

Large scale production and easy integration of quantum emitters are possible using thermoplastic polymers such as poly (methyl methacrylate) (PMMA). This thermoplastic polymer has a low glass-transition temperature around 110 °C. This makes the heat reflow process quite easy and creates significantly less heat as compared to the CO_2 laser used for silica. Furthermore, PMMA is a low cost material and allows the functionalization of the resonators for microlasing [14, 15], biosensing [16], and for the formation of photonic molecules [17].

For the realization of active resonators (microlasers) the integration of a gain medium into high-Q resonators is indispensable. Due to their near-unity quantum yield and their compatibility with the the polymer host matrix, organic laser dyes are ideal gain medium in polymeric cavities. Solid-state organic dye lasers are nonvolatile, nontoxic, mechanically stable and show a long operational time and can be made in compact forms [18]. Polymeric microcavities doped with organic dyes (e.g. rhodamine 6G and pyrromethene 597) show low threshold lasing (in few nJ/pulse [19]).

The other best suited emitters are colloidal quantum dots (QDs) that show size-dependent spectral tuning. These emitters show better temperature stability and narrower emission linewidths owing to their carrier confinement. Quantum dot lasing was achieved in the early 1990s [20] and there has been significant improvement in lowering the threshold energy and increasing the temperature stability of the laser. In colloidal QDs the competition between radiative and non-radiative relaxation mechanisms have a role on the optical gain required for lasing. They are typically related to the size and the surface property of the QDs.

There are many studies on the optical properties of colloidal QDs in WGM resonators [1, 21, 22] but research on the coupling of strongly confining bare core QDs (e.g. bare core CdTe QDs), to the eigenmodes of the WGM cavities is still challenging. This is due to the quick bleaching of the QDs and show negative response to lasing for both continuous wave (cw) and pulsed pumping as the damage threshold of this type of QDs is much lower than the threshold energy necessary for lasing [21–23]. The other reasons are the typically low quantum efficiency of the emitters associated with carrier trapping by surface defects of the bare core QDs and the loss mechanisms introduced due to the small size of the nanocrystals (Auger decay) [24]. This work investigates and shows the possibility to achieve lasing from strongly confined bare core nanocrystal quantum dots in polymeric microresonators (without any surface

functionalization and tedious sample preparation). Also it shows different techniques for the realization of room temperature core/shell QD-lasers on a silicon chip.

So far an obstacle which effectively limits some of the application of WGM resonators is the limited tunability of the cavities. Tunable resonators create possibilities for all optical control in photonic devices, enabling controlled interaction between emitter modes and cavity resonances in light-matter interaction of cavity quantum electrodynamics (c-QED). In semiconductor WGM resonators tuning of the resonance modes is achieved via temperature, electric field and carrier induced change of optical properties (thermo-optic and electro-optic effects) [25–28]. Liquid WGM resonators have been tuned by changing the size of the droplet resonators [29] or by mechanical size stretching [30–32] as the resonance condition depends on the radius of the cavity. But in general functional facility and reversibility are difficult to attain. Using the birefringence and electric field induced structural deformation of liquid crystals (LCs), researchers have shown shifting of cavity modes using LCs as a cladding layer [33], or using LC-droplet resonators [34] and also by immersing semiconductor microcavities in LC solutions [35]. However these methods do not show controlled reversible tunability and are not suitable for on-chip integration. Perfectly controlled and reversibly-tuned WGM resonators, with the tuning mechanism maintaining the ultra-high Q-factor of the resonator, is indispensable. In this work the fabrication and optical characterization of optically controlled, reversibly-tuned stable polymeric microcavities (lasers) is presented.

The general objective of this work is the utilization of ultra-high Q-factor polymeric microresonators for the realization of microlasers based on semiconductor colloidal quantum dots as a gain medium. The optical properties and characterization of passive resonators are discussed and the different techniques for the integration of emitters and experimental approaches are presented. Also a possibility for reversible, dynamic tuning of polymeric WGM resonators is presented. This tunability is based on the photo-induced size control of goblet resonators using artificial smart materials.

Organization of the thesis

This thesis is organized into six chapters. In chapter 2, an introduction into WGM resonators is presented. Mode nomenclature and modal structure of WGMs is discussed. The loss mechanisms and the limitations of the Q-factor are theoretically presented and the fabrication process of polymeric microresonators along with its optical characterization is shown.

A general description of optical and electrical properties of semiconductor nanocrystal quantum dots as a gain medium for the realization of quantum dot lasers is

presented in chapter 3. For the integration of quantum dots into polymeric microresonators three different techniques are discussed: sandwiching of QDs between polymer layers, core/shell/PMMA hybrid particle doping and highly localized quantum dot deposition using dip-pen nanolithography.

High quantum yield organic dyes as a gain medium for polymeric resonators are discussed in chapter 4. The electrical and optical properties and the conditions leading to optical gain for developing dye lasing are presented.

In chapter 5, photo-responsive artificial smart materials (namely liquid crystal elastomers) are introduced. The optical and structural properties of liquid crystal elastomers as micro-actuators are presented. The fabrication process and the different monomer mixtures of the liquid crystal elastomers are discussed. For photo-induced controlled tuning of microresonators, special type of azo-dye (photo-responsive) comprising liquid crystal elastomer microcylinders are fabricated and incorporated into goblet resonators. The integration process and the optical characterization of elastomer/polymeric resonators are discussed. Finally the tuning mechanism is presented.

Chapter 6 summarizes the most important part of this thesis, draws conclusions and gives an outlook for ongoing work in the future.

Chapter 2

Optical Properties of Polymeric Whispering Gallery Mode Microcavities

This chapter provides a fundamental insight into polymeric whispering galley mode resonators. Mode classification, modal structure and the loss mechanisms limiting the quality factor of (polymeric) microresonators are discussed. The fabrication process and optical characterization of the resonators will also be presented. The optical properties and its characterization provide a frame work for the active resonators presented in the next chapters.

2.1   Whispering Gallery Mode Resonators

Whispering gallery mode (WGM) phenomena were initially explained by Lord Rayleigh around 1910 based on the observation of acustic waves, whispers, under the dome of St. Paul's Cathedral in London [36, 37] (Fig. 2.1). It was observed that a whisper uttered at one end of the dome is heard at the other end away from the source (hence the name whispering gallery mode). The sound wave seems propagating only in a narrow layer near the surface of the dome due to repeated reflection. In free space the sound intensity decreases with the square of the distance $I \propto \frac{1}{r^2}$ but in the concave wall of the gallery the intensity decreases with distance according to $I \propto \frac{1}{r}$ [38] , hence the sound wave is heard even for longer distance around the dome.

Similar WGM phenomena were also observed for electromagnetic waves [39] by confining light in a rotationally symmetric curved boundaries. This is achieved by using

Figure 2.1: (a) St. Paul's cathedral church in London (flickr.com). (b) The whisper at
one end of the wall is heard at the other end due to the repeated reflection of the acoustic
wave near the the curved boundary of the wall (wanderstories.com).

a medium which has a larger index of refraction as compared to the surrounding
medium. Therefore, the light will be trapped inside the curved surface by total
internal reflection. After a complete trip the light will interfere with itself construc-
tively and destructively. It is the constructively interfered waves that developed the
condition for standing waves and the WGM resonances. For rotationally symmetric
microcavity of radius R and index of refraction n, the constractive interferance of
the azimuthally propagating light wave leading to WGM resonances is given by:

$$2\pi R = m\frac{\lambda_0}{n} \tag{2.1}$$

where m is integral azimuthal mode number describing the number of wavelength
of the WGM within the cavity boundary and λ_0 is free-space resonance wavelength.

So far different rotationally symmetric WGM cavity geometries have been introduced
as depicted in Fig. 2.2. Microtoroid [40,41], miscrosphere [42–44], microdisk [45–47],
and microgoblet [10] resonators are the most common ones. In this work polymeric
microdisk and microgoblet resonators are used. Fig. 2.2 (c) and (d) showing scanning
electron micrograph images of PMMA-based microdisk and microgoblet resonator
on a silicon pedestal. Since the light is trapped in the rim of the resonator, most of
the electromagnetic field and optical energies are found around the circumference of
the curved surface. Even if most part of the optical energies are confined within the
boundary of the cavity, a small fraction of the field will leak-out of the resonator
as an evanescent field as shown in Fig. 2.3. This leaky field (evanescent field) is
exploited for coupling of wave guides (e.g tapered fiber, prism coupling), quantum
emitters and also play a significant role in sensing applications via its interaction
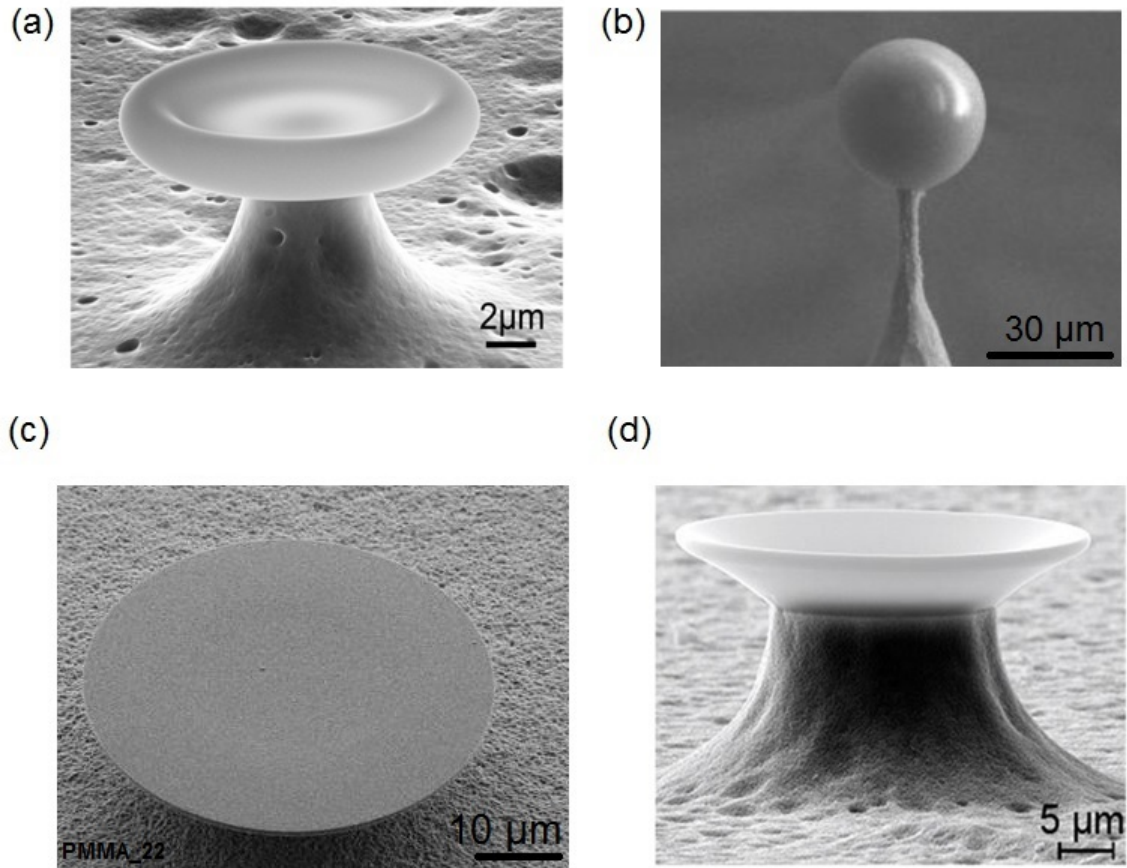
Figure 2.2: Scanning electron micrograph images of WGM resonators: (a) Silica microtoroid [50]. (b) Silica microsphere [51]. (c) Polymeric microdisk. (d) Polymeric microgoblet [50].

with the environment [4, 48, 49].

2.2   Classification and Optical Properties of WGMs

2.2.1   Mode classification

In this section some general theory of WGMs in ideal microdisks based on a simple approach to solve Maxwell's equations is presented. In charge- and current-free
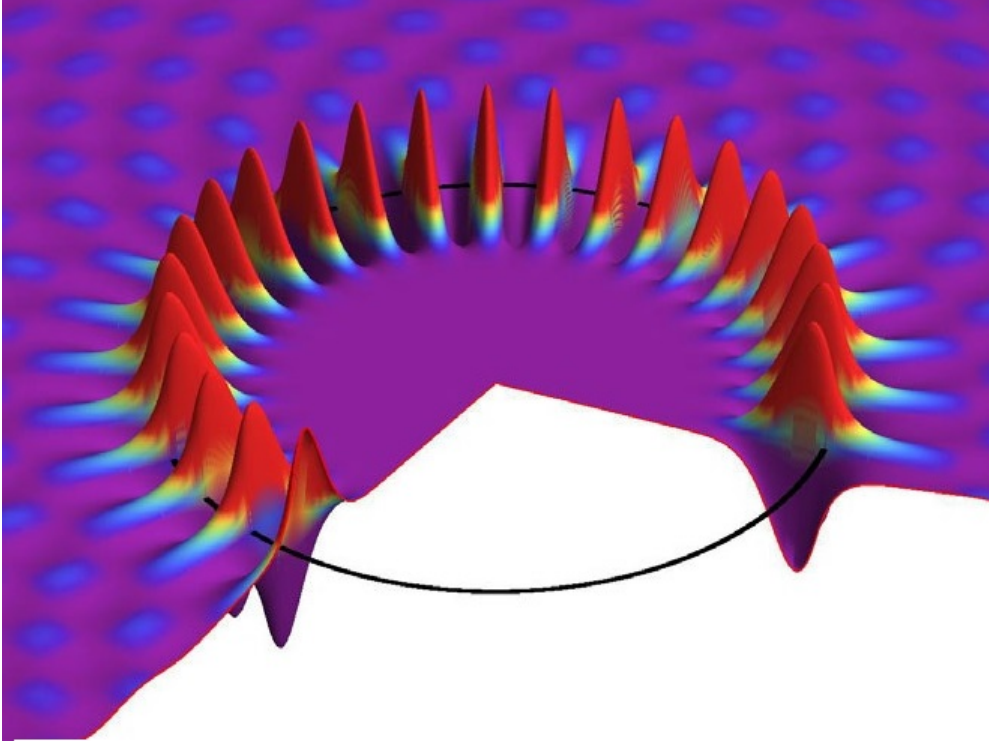
Figure 2.3: The electric field and the exponentially decaying evanescent tail of electric field as a function of radius r and angle ϕ, for azimuthal mode number m= 30. The black line represents the edge of the resonator [50].

microdisk resonators, the Maxwell equations are given by:

$$\vec{\nabla} \cdot \vec{D}(\vec{r}, t) = 0 \tag{2.2}$$

$$\vec{\nabla} \cdot \vec{B}(\vec{r}, t) = 0 \tag{2.3}$$

$$\vec{\nabla} \times \vec{E}(\vec{r}, t) = -\frac{\partial \vec{B}(\vec{r}, t)}{\partial t} \tag{2.4}$$

$$\vec{\nabla} \times \vec{H}(\vec{r}, t) = \frac{\partial \vec{D}(\vec{r}, t)}{\partial t} \tag{2.5}$$

where the electric displacement field $\vec{D}(\vec{r}, t)$ and the magnetic field density $\vec{B}(\vec{r}, t)$ are defined by $\vec{D}(\vec{r}, t) = \epsilon(\vec{r})\vec{E}(\vec{r}, t)$ and $\vec{B}(\vec{r}, t) = \mu(\vec{r})\vec{H}(\vec{r}, t)$ respectively. $\epsilon(\vec{r})$ and $\mu(\vec{r})$ are the permittivity and permeability of the medium. The geometry of the disk imposes the boundary conditions. Considering a time dependence of the electric- and magnetic fields $\sim \exp{(-i\omega t)}$ and following standard derivation as shown in [52], the

above equations can be simplified to the following symmetrical Helmholtz equations:

$$\vec{\nabla}^2 \vec{E}(\vec{r}) + k_0^2 n^2(\vec{r}) \vec{E}(\vec{r}) = 0 \tag{2.6}$$

$$\vec{\nabla}^2 \vec{H}(\vec{r}) + k_0^2 n^2(\vec{r}) \vec{H}(\vec{r}) = 0 \tag{2.7}$$

The symmetry leads to an easy approach. Modes whose electric field is dominantly polarized perpendicular to the plane of propagation are termed as transverse magnetic (TM) modes and modes whose magnetic field is dominantly polarized perpendicular to the plane of propagation are transverse electric (TE) modes. In the next part only completely polarized TM and TE modes are considered. For these particular modes only the z-component of $\vec{E}$ field or z-component of $\vec{H}$ field has a finite value and the other components vanish. This allows us to solve Helmholtz equations for the z-component of the field. Since a microdisk has cylindrical symmetry, the above equations can be written as:

$$\left[\frac{\partial^2}{\partial \rho^2} + \frac{1}{\rho} \frac{\partial}{\partial \rho} + \frac{1}{\rho^2} \frac{\partial^2}{\partial \phi^2} + \frac{\partial^2}{\partial z^2} + k_0^2 n^2(\rho, z) \right] \zeta(\rho, \phi, z) = 0 \tag{2.8}$$

where $\zeta(\rho, \phi, z)$ refers to E_z or H_z accordingly. Using separation of variables techniques, one can replace $\zeta(\rho, \phi, z) = U(\rho)\Phi(\phi)Z(z)$. Hence the equation takes the form:

$$\frac{\partial^2 U}{\partial \rho^2} + \frac{1}{\rho} \frac{\partial U}{\partial \rho} + \left(k_o^2 n_{eff}^2 - \frac{m^2}{\rho^2} \right) U = 0 \tag{2.9}$$

$$\frac{\partial^2 \Phi}{\partial \phi^2} + m^2 \phi = 0 \tag{2.10}$$

$$\frac{\partial^2 Z}{\partial z^2} + k_0^2 \left(n^2(z) - n_{eff}^2 \right) Z = 0 \tag{2.11}$$

Solving the above equations leads to ρ, ϕ and z dependent functions:

ϕ-dependance

The ϕ-dependent equation has a solution of the form:

$$\Phi(\phi) \propto e^{\pm im\phi}, \ \ m \in \mathbb{N} \tag{2.12}$$

The solution is twice degenerate with $+m$ and $-m$, which corresponds to the modes propagating in clockwise and counter-clockwise direction around the microdisk. Imperfections and unavoidable irregularities on the surface of the resonators during the fabrication process can lift the degeneracy and leads to splitting of the modes [45].

z-dependance

The solution for $Z(z)$ can be computed as shown in ref. [53]. Inside the microdisk the fields are varying sinusoidal and decay exponentially outside the disk surface. Using the boundary conditions at the interface of the disk, the effective index n_{eff}, which is an important parameter for finding the resonance frequencies, can be determined.

For TE modes $Z(z)$ takes the form:

$$Z(z) = A\sin(az), \ \ |z| \leq \frac{d}{2} \tag{2.13}$$

$$Z(z) = Be^{-b(|z|-d/2)}, \ \ |z| \geq \frac{d}{2} \tag{2.14}$$

where

$$a = k_0\sqrt{n_{Disc}^2 - n_{eff}^2} \tag{2.15}$$

$$b = k_0\sqrt{n_{eff}^2 - n_0^2}. \tag{2.16}$$

ρ-dependance

The solution for $U(\rho)$ is given by Bessel functions of the first kind and Hankel functions of the second kind for the region inside and outside the microdisk respectively. The Hankel function can be approximated by an exponentially decaying term $\beta = k_0\sqrt{n_{eff}^2 - n_0^2}$ [54]. Hence $U(\rho)$ turns out to be:

$$U(\rho) \propto J_m(k_0 n_{eff}\rho), \ \ \rho \leq R \tag{2.17}$$

$$U(\rho) \propto J_m(k_0 n_{eff}R)e^{-\beta(\rho-R)}, \ \ \rho \geq R \tag{2.18}$$

Mode nomenclature

In the previous section it is shown that even a simple picture of the microdisk shows complex modal structures. Different modes exist for each field-polarization and quantum numbers (e.g azimuthal quantum number m). In practice each mode is named by its polarization, azimuthal mode number m, the axial mode number l and the radial mode number n. The quantum number l and n denotes the number of maxima of the energy density minus one in ρ- and z direction respectively. The notation refering to the modes used in this work will be $TE_{n,l}^m$ or $TM_{n,l}^m$ respectively.
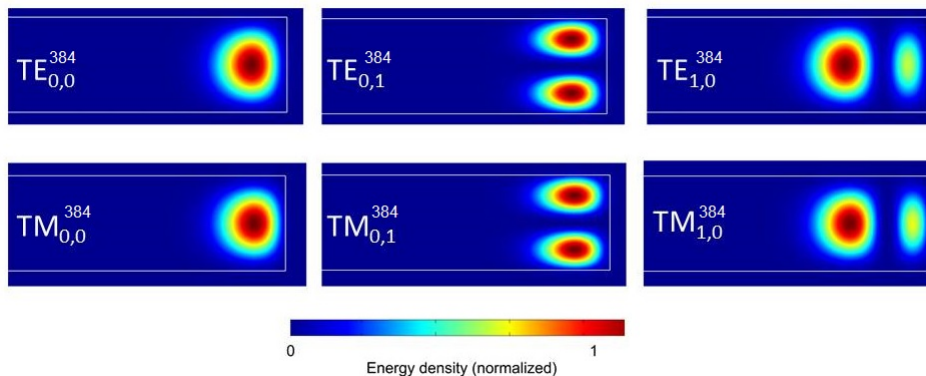
Figure 2.4: Mode classification and electric energy density distribution in a microdisk resonator. The fundamental modes of both polarization (TE and TM) are confined on the rim of the resonators and the higher order modes are far away from the rim depending of the quantum numbers. The electric energy density distribution and resonance wavelength of the WGMs were calculated with `JCMResonance`. The azimuthal mode number of the presented WGMs is $m = 384$.

In this work the typical microcavities have a diameter of $45-49 \ \mu m$, and thickness around $1.2 \ \mu m$. Fig. 2.4 shows the field pattern of the energy density of $TE_{n,l}^m$ or $TM_{n,l}^m$ modes of microdisk cavity of $49 \ \mu m$ and $1.2 \ \mu m$ thickness.

The fundamental mode, namely $TE_{0,0}^m$ ($TM_{0,0}^m$), as shown in Fig. 2.4, is confined on the rim of the resonator, while the other modes with more than one energy density maxima are higher order modes and their confinement is far from the very rim of the cavity. Even if the electric energy density distribution of same quantum number TE and TM modes looks the same, the resonance wavelength has a slight difference.

2.2.2 Optical properties of microresonators

Mode volume

The mode volume is the measure of the spatial confinement of a mode in a microresonator. It is considered as the volume in which the main part of the modal energy is stored. It can be defined by relating the total energy within the region of interest to the maximum value of the energy density [55].

$$U = \int_V \epsilon(\vec{r})|\vec{E}(\vec{r})|^2 dV = V_m \cdot \max\left(\epsilon(\vec{r})|\vec{E}(\vec{r})|^2\right) \tag{2.19}$$

where V_m is the mode volume.

According to this expression mode volume is the ratio of total energy stored inside
the resonator in that mode and the maximum energy density of the mode.

The lasing characteristics of the resonator (containing gain medium) depend on the
mode volume as stimulated/spontaneous emission rate are inversely proportional to
mode volume and lasing threshold is directly proportional to it [56]. Small mode
volume cavities are also most important for non-linear and quantum electrodynamics
studies. The common units for mode volume is cubic wavelength $(\lambda_0/n)^3$ or μm^3.

Free spectral range

The free spectral range is the spectral distance between adjacent modes. As it is
explained in the previous section, the modal structure of WGM resonators is complex
and it is difficult to find two adjacent modes as they are differently polarised and
also have different quantum numbers l, m, and n. However, it is quite possible to
approximate the spacing between two modes of different azimuthal mode numbers
$(m, m + 1)$ while the polarization, the radial and axial mode numbers are fixed. In
this case the free spectral range can be derived from equation 2.1 [57] and takes the
form:

$$\delta\lambda_{FSR} = \frac{\lambda_0^2}{2\pi Rn + \lambda_0} \approx \frac{\lambda_0^2}{2\pi Rn} \qquad (2.20)$$

The approximation is valid for $R \gg \lambda$. This holds true for all the cavities used in
this work.

Q-factor

The quality factor is the measure for the temporal confinement of the energy within
the cavity. It relates the energy stored inside the cavity to the energy loss due to
different loss mechanisms [52]:

$$Q = \omega_0 \frac{U}{P_{loss}} = -\omega_0 \frac{U}{dU/dt} = \omega_0 \tau \qquad (2.21)$$

where U is the total energy stored in the cavity, ω_0 is the resonance frequency and
P_{loss} is the power loss of the cavity. The Q-factor also relates to the photon lifetime
τ, which is the time that a photon remains inside the cavity before it is lost due to

different loss mechanisms discussed in the next subsection. Using equation 2.21, the total energy in the resonator decays according to:

$$U \propto e^{-\omega_0 t/Q} \tag{2.22}$$

which provide time dependence electric field $(U(t) \propto | E(t) |^2)$ inside the cavity:

$$E(t) = E_0 e^{-\omega_0 t/2Q} e^{-i(\omega_0 + \delta\omega)t} \tag{2.23}$$

where $\delta\omega$ is the shift of the resonance frequency by the loss mechanisms. A Fourier transform of this equation gives the spectral shape of the resonance:

$$|E(\omega)|^2 \propto \frac{1}{(\omega - \omega_0 - \delta\omega)^2 + (\omega_0/2Q)^2} \tag{2.24}$$

The expression shows a Lorentzian line-shape with a full-width at half-maximum $\Delta\omega = \omega_0/Q$ or $\Delta\lambda = \lambda/Q$. Hence:

$$Q = \frac{\lambda}{\Delta\lambda} \tag{2.25}$$

This expression provides a simple technique to determine the life time of photons inside the cavity only by measuring the linewidth of the cavity mode at a particular resonance wavelength.

Finesse $\mathcal{F}$

Finesse $\mathcal{F}$ of the cavity is defined as the ratio of the free spectral range $\delta\lambda_{FSR}$ to the linewidth $\Delta\lambda$ of a resonance mode.

$$\mathcal{F} = \frac{\delta\lambda_{FSR}}{\Delta\lambda} \tag{2.26}$$

Using the definition of the Q-factor, $\mathcal{F}$ can also be written as $\mathcal{F} = \frac{Q}{m}$. The higher the finesse of a microresonator, the wider is the spacing between adjacent modes as compared to their linewidth.

2.2.3 Loss mechanisms and the limitations of the Q-factor

The power loss in microcavities are mainly due to absorption, radiation, surface scattering and loss due to coupling. Assuming that each losses are independent of each other, the total power loss is given by : $P_{total} = \sum_i P_i$. According to equation

2.21 a Q-factor Q_i can be defined for each loss mechanism and the total Q-factor
becomes:

$$\frac{1}{Q_{total}} = \sum_i \frac{1}{Q_i} \tag{2.27}$$

The expression tells the high Q-factor of the loss mechanism, the less it contributes
to the total Q-factor and to the linewidth of the mode.

Radiation losses

Due to the curved surface a small part of the light is lost due to radiation. This
loss can also be interpreted as tunnelling of photons through a potential barrier.
Radiation loss is mainly dependent on the curvature of the surface, hence on the
radius R and azimuthal mode number m. For a given wavelength and radius, the
number of energy density maxima goes with $2m$. Hence, the total energy stored
in the resonator depends on the azimuthal mode number m. Numerical calculation
shows the radiation Q-factor Q_{rad} increases exponentially with m [58,59]. Using the
WKB method [58] it is shown that:

$$Q_{rad} \propto e^{2mh} \tag{2.28}$$

where h $= \tanh\sqrt{1 - 1/n_{eff}^2} - \sqrt{1 - 1/n_{eff}^2}$. For a given wavelength m scales ap-
proximately proportional to R (see equation 2.1) hence the same behaviour is ex-
pected for the R-dependence of the radiation Q-factor.

Resonators used in this work has radius greater than R= $20\,\mu m$, $m > 280$ around
600 nm. Hence the radiation loss is negligible ($Q_{rad} = 10^{16}$) [19].

Absorption losses

The absorption of electromagnetic waves in bulk material is expressed in terms of
the absorption coefficient α or by the imaginary part n_i of the refractive index
$n = n_r + in_i$. Using the definition of a plane wave propagation:

$$E(x,t) = E_0 e^{i(kx-\omega t)} = E_0 e^{-\omega n_i x/c_0} e^{i\omega(n_r x/c_0 - t)} \tag{2.29}$$

and the absorption coefficient $I = I_0 exp(-\alpha x) \propto |E(x,t)|^2$, one can find:

$$\alpha = \frac{4\pi n_i}{\lambda_0}. \tag{2.30}$$

Using the fact that in the time t light travels a distance of $x = c_0 t / n_r$, the absorption Q-factor Q_{abs} can be defined by comparing equation 2.29 and equation 2.23:

$$Q_{abs} = \frac{2\pi n_r}{\alpha \lambda_0} = \frac{n_r}{2 n_i} \tag{2.31}$$

The resonators in this work are made from PMMA polymers which has low absorption in the visible wavelength range. In this type of microresonators, the absorption-limited Q-factor Q_{abs} possibly reach upto 10^8 at visible wavelengths and around 10^6 near the infra-red wavelength region [19].

Surface scattering

Surface scattering is one of the losses mechanisms induced by surface imperfections. Surface imperfections are mainly caused due to the fabrication process and in general difficult to avoid it. For instance the Q-factors of polymeric microresonators after lithographic fabrication is found to be between 10^4 and 10^6 [10, 60].

The effect can be reduce by increasing the dimensions of the microresonators. Numerical calculations shows the dependency of the surface-scattering limited Q-factor Q_{ss} to the radius of the resonator [45]. Instead of increasing the size, a well known process called surface-tension induced reflow process leads to ultra smooth surfaces. Q-factors above 10^{10} were reported using CO_2 laser for atomic surface finish (surface-tension induced) reflow process [40]. As it is discussed on the introduction part, this process has huge limitations but for polymeric cavities which are discussed in this work uses relatively low temperature thermal reflow process to reduce the loss introduced by surface scattering.

2.3 Fabrication of Polymeric Microcavities

Polymeric PMMA resonators are fabricated in a simple four-step process as discussed in ref. [10]. At the beginning a 1-1.5 μm thick PMMA layer (polymer matrix, MicroChem PMMA 950k A7, in anisol is used) is spin coated on a silicon substrate. To reduce the solvent the sample is baked at 110 °C. When the sample cool down, stress between the PMMA and the silicon substrate is maintained due to the different thermal expansion coefficients of the two materials. The thermal expansion coefficient of PMMA is $300 \times 10^6 \, \mathrm{K}^{-1}$ [61] and $2.5 \times 10^6 \, \mathrm{K}^{-1}$ for silicon at room temperature [62]. Then PMMA resonator disks are patterned using e-beam lithography (Fig. 2.5 (a)).
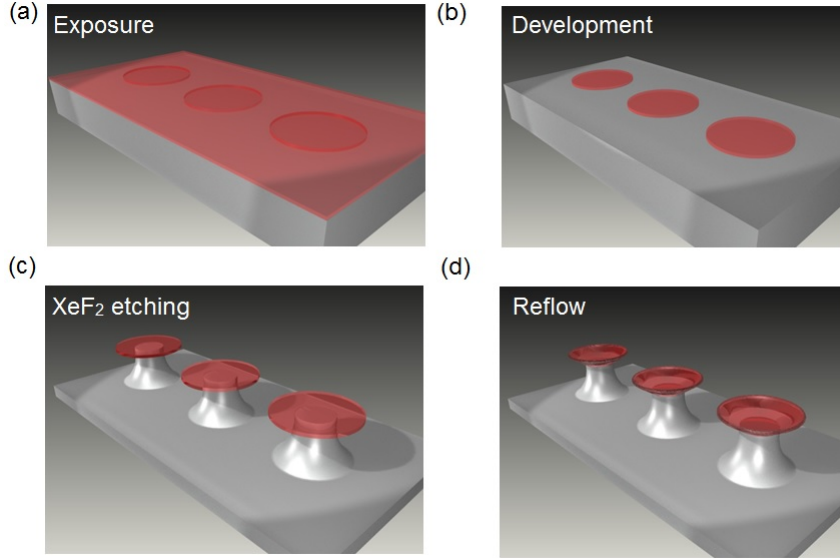
Figure 2.5: Fabrication of polymeric microresonators. (a) Disks on a PMMA coated
silicon wafer are patterned by e-beam exposure. (b) Chemical development of the exposed
PMMA. (c) The silicon is isotropically etched using XeF_2 result in microdisks standing
on silicon pedestals. (d) A thermal reflow process leads to surface-tension induced goblet
geometry microcavities.

After chemical development (Fig. 2.5 (b)) and isotropic etching with XeF_2, PMMA-
based microdisks are standing on silicon pedestals (Fig. 2.5 (c)). Heating the sample
for 30 s at a temperature of 125 °C slightly above the glass-transition temperature
T_{gt} of PMMA ($T_{gt} \simeq$ 100 °C- 110 °C), leads to a smooth surface-tension induced
goblet resonator geometry.

Fig. 2.6 (a) and (b) show scanning electron micrograph images of polymeric mi-
crodisk and microgoblet resonators respectively. Unlike microtoroids and other re-
sonators discussed in the introduction part, PMMA-based polymeric resonators can
be fabricated in a large scale on a chip. Since the thermal reflow process can be
done at much smaller temperatures as compared to silica toroids, the integration of
other optical components and also emitters is possible.

(a)

(b)

10 µm

5 µm
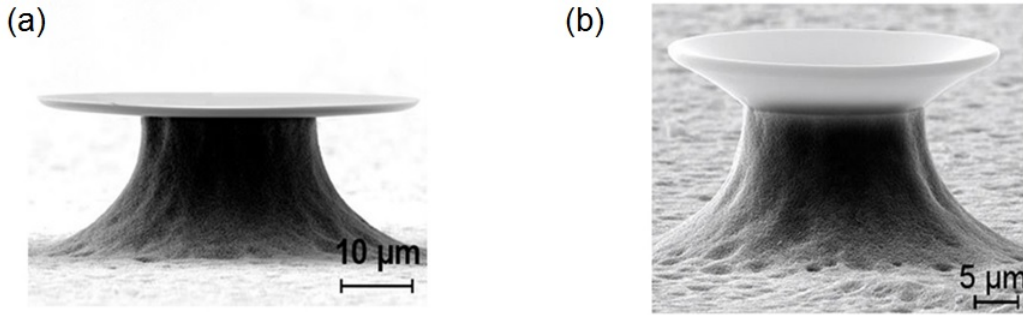
Figure 2.6: (a) Scanning electron micrograph image of PMMA microdisk resonator [50]. (b) The heat reflow process leads to smooth-surface goblet resonator geometry [50]

.

2.4   Resonator-Waveguide Coupling

This section provides the theoretical description of evanescent wave coupling into microresonators and also describes the experimental approach used to excite whispering gallery modes of polymeric microcavities. For the coupling-experiment a tapered single mode optical fiber is used.

2.4.1   Analytical approach for tapered optical fiber coupling

Phase-matching between the cavity resonance mode and the wave guide mode is indispensable for the efficient coupling of waves into and out of the microcavity. Due to the different phase velocity of the electromagnetic waves in air and in the PMMA material of the resonators excitation of WGMs via free-space excitation is practically difficult. Phase velocities are determined by the effective index of refraction of the optical mode. In order to achieve efficient phase-matching conditions, prism coupling and tapered wave guide coupling are ideal candidates. In a tapered fiber wave guide, the evanescent field of the resonator and the coupler is made to overlap significantly by adjusting the distance between them [13, 63]. This enables the tunnelling of the field from the wave coupler to the cavity and vice versa (it is completely analogous to quantum tunnelling in quantum physics).

When the fiber is tapered adiabatically, only few fundamental modes propagates through the core of the fiber. Conditions for adiabatic tapering of an optical fiber are discussed in the next subsection. In a tapered optical fiber, the evanescent field of the light can stretch out. When this evanescent field is brought to overlap with the evanescent field of the cavity efficient coupling occurs. Another important

condition for efficient coupling of a tapered fiber and a cavity is the matching of
internal resonator loss and wave guide coupling loss. These create critical coupling
and the resulting transmission at the output of the fiber goes to zero on resonance,
hence all the energy pumped inside the fiber gets transferred to the resonator.

Considering the coupling of modes in- and out of the cavity in time and space a
matrix model of the coupling amplitudes [64] describes the coupling behaviour. If
the coupling is weak, the time rate and the spatial rate of change of the amplitudes
of coupled modes can be expressed by first order derivatives (higher order derivatives
are negligible). When the rate of change per cycle or per wavelength is small, as
it is used in this research work, weak coupling is a good approximation. So using
coupling-of-mode formalism [65] in slowly varying amplitude (i.e $E_c(t+\tau) - E_c(t) \approx
\tau \frac{d}{dt} E_c(t)$, where $E_c(t)$ is the field inside the cavity and τ is the cavity round-trip
time) it is possible to express the master equation describing the dynamics of the
mode in and outside of the cavity. For the resonance frequency of the cavity ω_0,
intrinsic cavity loss $1/\tau_0$, and coupling loss due to coupling of wave guide $1/\tau_{ex}$, the
master equation takes the form [65]:

$$\dot{a} = i\omega_0 a - \left(\frac{1}{2\tau_0} + \frac{1}{2\tau_{ex}} \right) a + \kappa b \tag{2.32}$$

Here the resonator excitation is denoted by a (is called the cavity mode), where as
the wave guide mode is represented by b. Using time reversal symmetry [65] the
coupling coefficient κ can be expressed by:

$$\kappa^2 = \frac{1}{\tau_{ex}} \tag{2.33}$$

It is worth to mention that $|a|^2$ refers to a normalized energy, where as $|b|^2$ refers to
a normalized power.

The energy loss of the resonator without the coupler effect is calculated from the
master equation 2.32 and is given by:

$$\frac{d}{dt} |a|^2 = -\frac{1}{\tau_0} |a|^2 \tag{2.34}$$

Hence the intrinsic Q-factor take the form $Q = \omega_0 \tau_0$, which is in agreement with
equation 2.21. For the same frequency and $b \propto \exp(i\omega t)$, the response will be given
according to equation 2.32. And one can express a interms of b as:
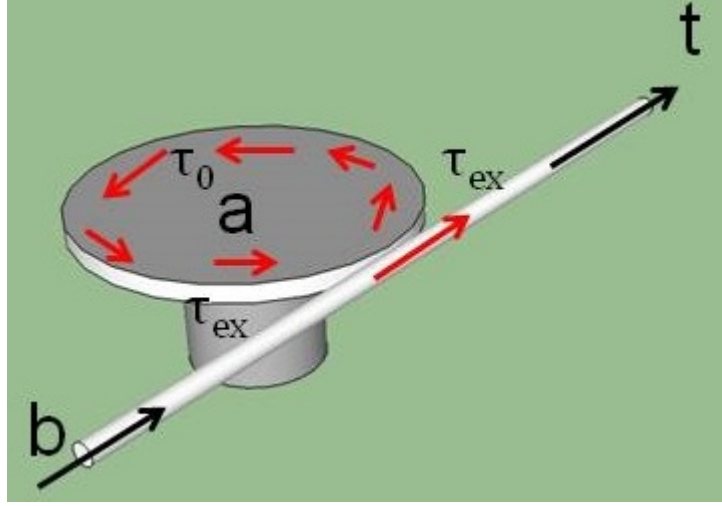
Figure 2.7: Schematic diagram of wave guide-resonator coupling. Part of the wave guide mode b is coupled in the resonator mode a. The transmitted light t is a superposition of the transmitted part of b and the part of a coupled back from the resonator into the fiber.

$$a = \frac{\kappa b}{i(\omega - \omega_0) + (2\tau_0)^{-1} + (2\tau_{ex})^{-1}} \tag{2.35}$$

The transmitted light t in the coupled wave guide (see Fig. 2.7) is the result of the transmitted waveguide mode (part of b) and part of a which is coupled back from the cavity into the wave guide coupler. Energy conservation leads the transmission $T = |t|^2$ to take the form [65]:

$$T = \left| \frac{\tau_{ex}^{-1} - \tau_0^{-1} - 2i(\omega - \omega_0)}{\tau_{ex}^{-1} + \tau_0^{-1} + 2i(\omega - \omega_0)} \right|^2 \tag{2.36}$$

$$= \left| \frac{Q_{ex}^{-1} - Q_0^{-1} - 2i(\omega - \omega_0)}{Q_{ex}^{-1} + Q_0^{-1} + 2i(\omega - \omega_0)} \right|^2. \tag{2.37}$$

The coupling-limited Q-factor is determined by the coupling efficiency $Q_{ex} = \omega_0 \tau_{ex}$.

Equation 2.37 shows that the transmission spectrum near the resonance frequency ω_0 has a Lorentzian-shaped linewidth. If the coupling losses are low so that $Q_{ex} \gg Q_0$, the regime is called under-coupled and the intrinsic cavity Q-factors Q_0 can be easily inferred from the full-width at half maxima of the Lorentzian-shaped dip of a mode in the transmission spectrum. If $Q_0 \gg Q_{ex}$ the system is said to be in the over-coupled regime and the loaded Q-factor $Q_l^{-1} = Q_{ex}^{-1} + Q_0^{-1}$ can be significantly
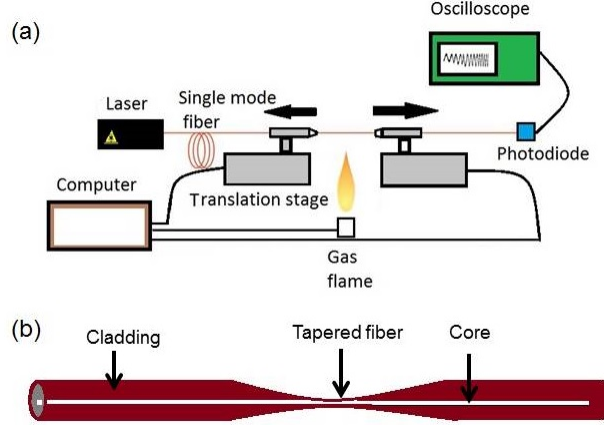
Figure 2.8: (a) Schematic diagram of the experimental setup for fiber tapering (flame
brushing technique). (b) After flame brushing and stretching, the tapered part of the fiber
becomes an air-guided region and it is this part of the fiber which couples light into the
microresonator (Modified from [66]).

lower than the intrinsic Q-factor. If $Q_0 = Q_{ex}$, the system is critically-coupled and
the transmission goes to zero at the resonance frequency ω_0. The dropping of the
transmission spectrum to zero is the result of the destructive interference of the equal
magnitude and phase shift π exhibited by the cavity leaky field and transmitted field
through the fiber [67].

To access all three regimes of coupling (under-coupled, over-coupled, and critically-
coupled regime) and to control the coupling coefficient κ and also the coupling
limited Q-factor Q_{ex}, the distance between the cavity and the fiber coupler can be
varied. In this work the coupling distance between fiber coupler and the resonator
distance is varied until WGMs of the cavity are efficiently excited. To do so the
tapered optical fiber is placed on a nm scale resolution translational stage. Next
the fabrication process of optical tapered fiber and the experimental setup for the
transmission spectrum is discussed.

2.4.2 Experimental tapered optical fiber coupling

A single mode optical fiber can be adiabatically tapered to few μm in diameter
(usually $1\,\mu m$) which allows only a fraction of the propagating fundamental mode in
the core of the fiber extends outside. It is this field that tunnels into the cavity for
the excitation of WGMs. It is approximated as an exponentially decaying optical
field. The propagation constant, which determines the phase matching condition
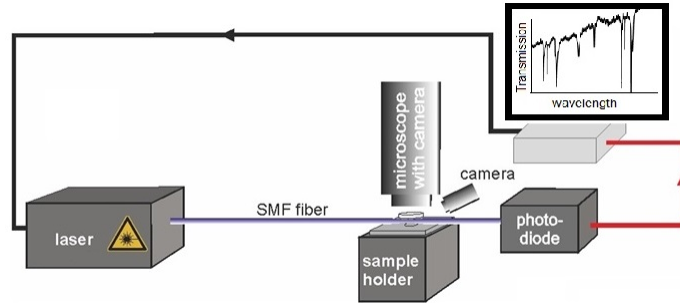
Figure 2.9: Schematic of measurement setup for optical fiber coupling for the excitation of WGMs.

varies with position along the taper transition region, hence it is a function which also depends on the taper diameter. In this work the tapered optical fibers were prepared from SMF-28 (for propagation of 600 nm light; $8.2 \, \mu m$ core diameter and $125 \, \mu m$ cladding diameter) commercially available optical fibers. About $2 \, mm$ of the cladding of the fiber is stripped (jacket removed). Then the stripped portion is cleaned and stretched while being heated by a flame (flame brushing technique, Fig. 2.8). The heating flame was controlled by a flow meter. To control the stretching a linear motor was used. A LabVIEW program controls the motion (the speed and time) of the linear motor and the flame. This allows for control of the tapered waist and stretching length. The two linear motors pull the fiber in opposite directions results in two taper transitions with a region of constant diameter. While tapering the fundamental mode, which was guided by the difference in the index of refraction between core and cladding, undergoes adiabatic transition to air-guided mode. As the stretching starts during flame brushing process, the air-guided region supports multiple modes. To be sure that the tapered region supports only single mode, the transmission signal is monitored by the oscilloscope as shown in Fig. 2.8. In this work the minimum tapered waist diameter is about $1 \, \mu m$.

For the transmission spectra measurement, the tapered fiber was placed on a five-axis positioning stage (with a resolution of 20 nm) and two cameras are used from the top and the side to monitor the exact position as depicted in Fig. 2.9. At first the fiber is coupled to a tunable diode laser. The tunable diode laser (New Focus Velocity TLB 6304) has a tuning range from 632.5 nm- 637 nm. The linewidth is less than 300 kHz (<0.3 fm) and the fine frequency range is 80 GHz (0.11 nm) with the maximum coarse tuning 6 nm/s and the typical wavelength repeatability is 0.1 nm. The tapered part of the fiber, coupled to the tunable diode laser, is brought close to
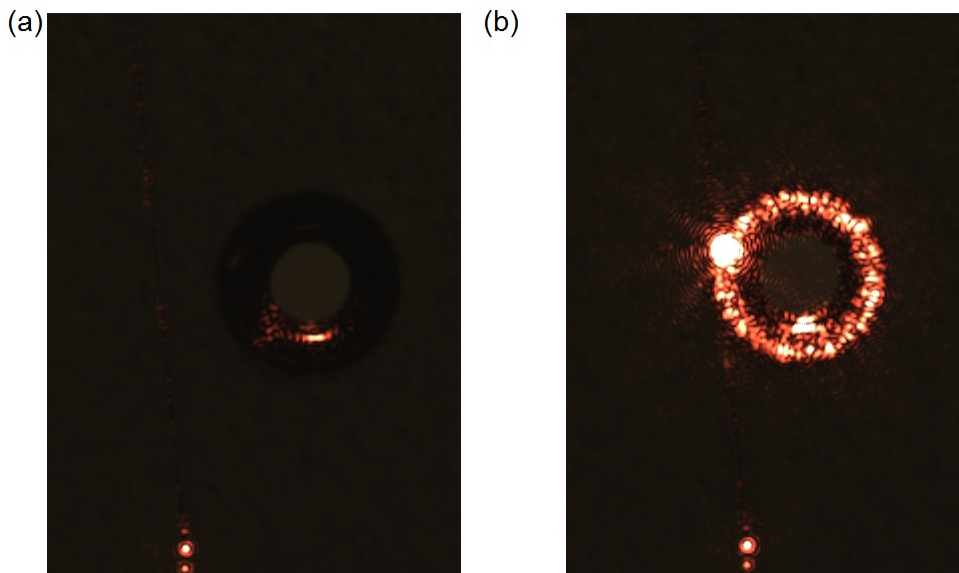
Figure 2.10: Microscope images of tapered fiber-resonator coupling. (a) Top view of the tapered fiber and the microresonator before coupling. (b) Light from the tunable diode laser (632.5-637.0 nm) is coupled into the resonator and the coupling is manifested by the observation of circulating light around the rim of the resonator.

the cavity. The transmitted light is collected via a photo-diode and the spectrum is analysed with a LabVIEW program on the computer. The resonator-tapered fiber distance was adjusted until the WGMs appeared as sharp dips in the transmission spectrum. Also on the camera the coupling is observed when the light is circulating around the rim of the resonator as shown in Fig. 2.10 (b).

Q-factor of polymeric resonators

The transmission spectra collected from the fiber (superposition of the incident light from the fiber and the light coupled out of the resonator) shows complex WGMs structures. The Q-factor measurement is conducted in the under-coupled regime to reduce the coupling losses due to the waveguide [11]. Inorder to avoid thermal effects due to the high field build up in the cavity, the power of the tunable diode laser was kept below several μW.

Fig. 2.11 shows the transmission spectrum of a microgoblet resonator of diameter $45\,\mu m$ near $630\,nm$ wavelength region. The modal spectrum shows a complex WGMs
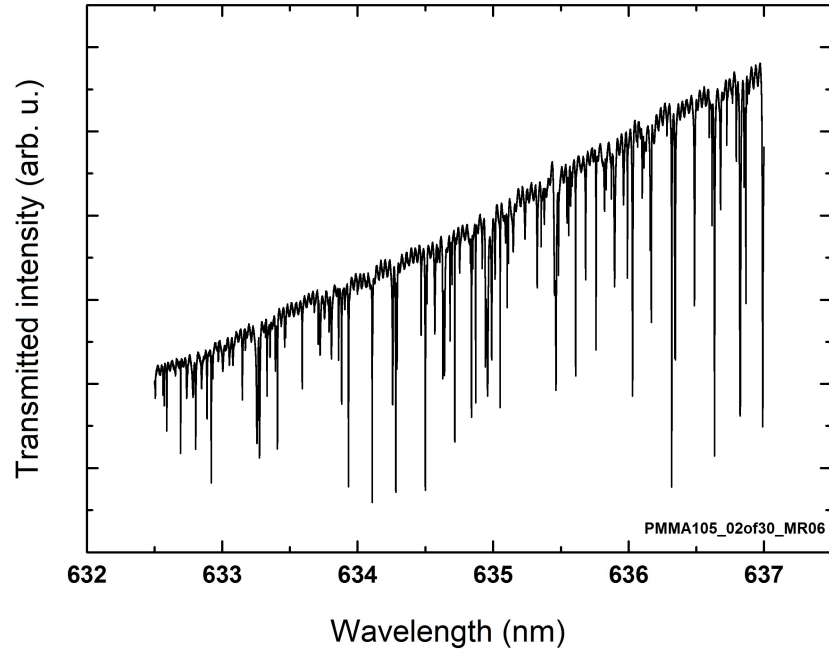
Figure 2.11: The transmission spectrum from evanescently coupled tapered fiber shows complex WGM structures of goblet resonator.

of different polarization. The Q-factor of the microgoblet resonators are about one order higher than the microdisk resonator. This must be due to the heat reflow process which induces smooth surface and reduces the scattering loss. The Q-factors of the WGMs are determined from the FWHM of the Lorentzian-shaped resonances observed in the dip of the transmission spectrum. The Q-factor of passive goblet resonators reach more than 10^7 [66] as depicted in Fig. 2.12.

Modal structure of goblet resonators

For the realization and understanding of the mode structures and the spatial distribution of the WGMs in microgoblets, finite element (FEM) simulations were performed. To Solve Maxwell equations for microdisk and microgoblet geometry (of similar size and thickness as used in the experiment) eigen solver JCMResonance, part of simulation software package JCMSuite from JCM wave is used. Interested readers on the simulation methods and solving techniques can read [19].

Fig. 2.13 shows the intensity distribution of energy density of the fundamental and
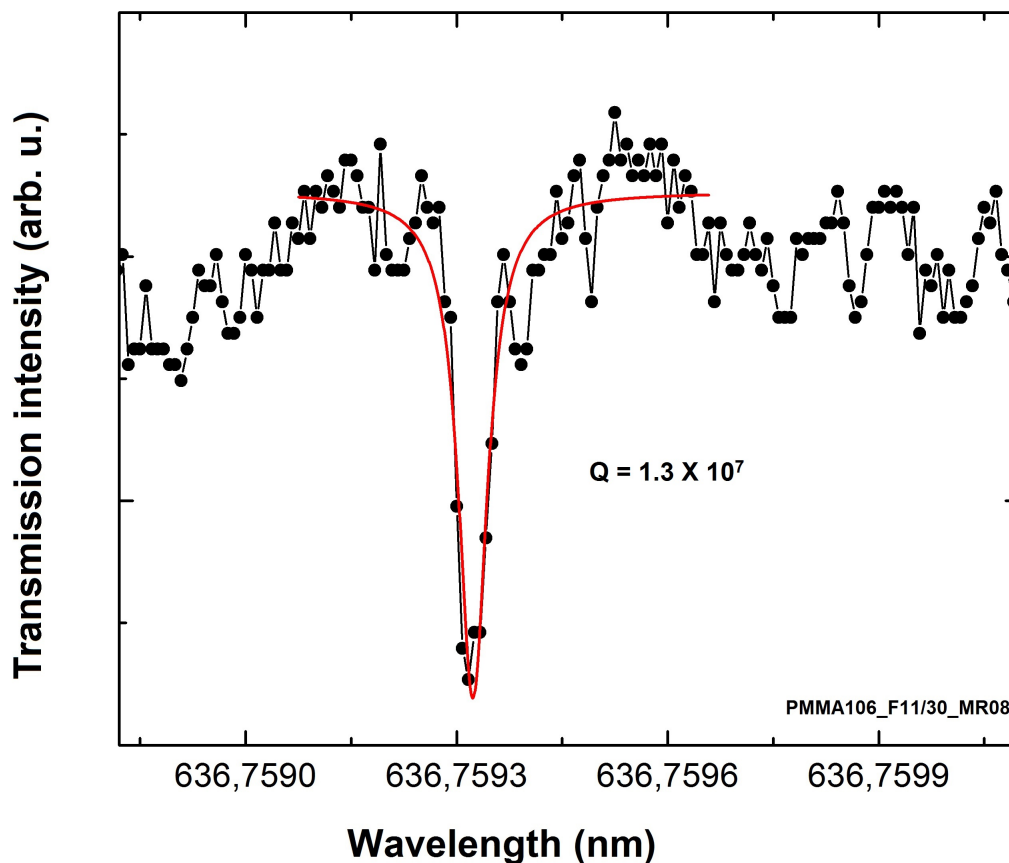
Figure 2.12: Polymeric goblet resonators have a Q-factors reaching up to 1.3×10^7 near 655 nm wavelength region. The Q-factor is inferred from the FWHM of the Lorentzian fit of the resonance in the under-coupled regime [66].

higher order modes of microgoblet resonator. The fundamental mode $TE_{0,0}^{381}$ are located on the rim of the resonator as shown in Fig. 2.13 (similar to disk resonators, see Fig. 2.4). As the mode numbers increases, the maximum of intensity moves away from the very rim of the resonator. The azimuthal quantum number of microgoblets is relatively smaller than the disks due to the decrease in the size of the goblet resonator during the heat reflow process. Again like polymeric microdisks TE and TM modes of similar radial and angular quantum numbers show slight resonance wavelength difference but the spatial energy density distribution is similar.
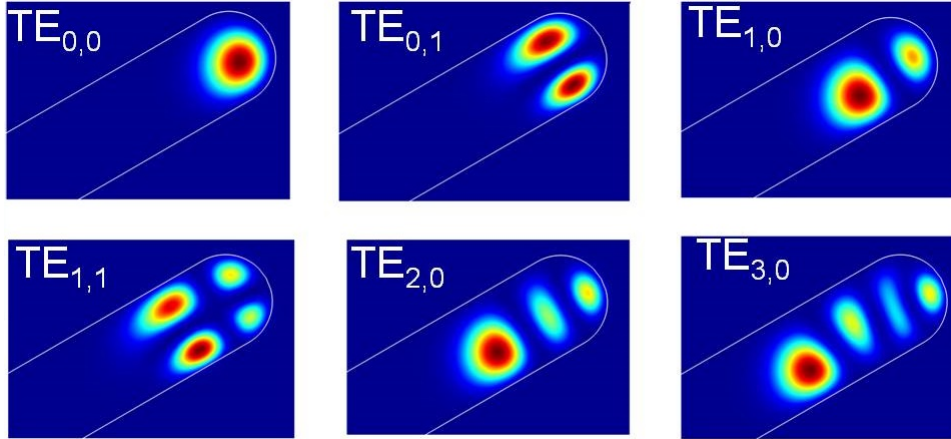
Figure 2.13: The intensity distribution of the electrical energy density of different WGMs in microgoblet resonator.

2.5   Summary and Conclusions

In this chapter, WGM resonators were introduced and the fabrication process of polymeric microdisk and microgoblets were presented. PMMA-based polymeric resonators were fabricated in a large scale on a chip. Surface-tension induced heat reflow process of polymeric disk resonators led to smooth surface goblet resonators geometry. Since the thermal reflow process were done at much smaller temperatures as compared to silica toroids, the integration of optical devices and quantum emitters (which will be presented in the next chapters) are possible. For evanescent coupling of light into the resonator, tapered fiber was used for the phase matching conditions. The excited WGMs showed complex modal structure with a Q-factor reaching more than 10^7. Simulation results also showed the spatial mode distribution of the WGMs.

Chapter 3

Quantum Dots in Microcavities

Semiconductor nanomaterials are widely used as gain medium in both electrically and optically pumped lasers. Two dimensional step-like density of electronic states of quantum wells enables higher concentration of carriers contributing for the band-edge emission and results in a narrow emission lines and a reduced lasing threshold [68]. A further enhancement in the density of band edge states and also improved temperature stability are obtained using two- and three spatial-dimension confined excitons (quantum wires and quantum dots (QDs) respectively). Semiconductor QDs are among the most promising emitters as the spacing of the electronic states is much bigger than existing thermal energy which inhibit thermal depopulation of the lowest electronic states. This results in temperature insensitive physical properties like lasing threshold [69].

In bulk semiconductors the band gap, the energy separation between the conduction and valence energy bands, determines the wavelength of the light emitted by the semiconductor material. The band gap is a fixed parameter determined solely by the identity of the material. However, when the size of the semiconductor is in few nanometres (with sizes smaller than about 10 nm) the nanocrystal is described in the regime of quantum confinement. This is the regime in which the spatial extent of the electronic wave function is comparable with the size of the nanocrystal size. This geometrical constraints leads to a quantum adjustment of the energy levels (quantum-size effect) similar to the situation in a particle in a box model. Size-dependent quantum confinement effect leads to variations in their electrical [70], optical [71], mechanical [72] and thermodynamical [73] properties. This is due to the increase in the confinement of carriers (electrons and holes) with the decrease in cluster size causing an increase in the band gap of the nanocrsytal and also quantization of electronic levels. This property makes QDs a bridge between solid state and single atoms (hence the name artificial atoms). Size tuning leads to spectral

tunability over a long range of the visible spectrum.

In this chapter the electronic structure, the gain and loss mechanisms relevant for lasing are discussed. The integration of QDs into polymer matrix is difficult due to the phase separation of the emitters from the polymer host matrix. The techniques presented in this chapter show different route to achieve efficient coupling of QDs emission (in the strongly confined regime) with the eigenmodes of microcavities. Different approaches for the realization of QD lasers are presented. In the first approach, quantum dot/polymer sandwich microcavity structures are presented, in this approach the colloidal quantum dots are embedded between PMMA layers without any surface functionalization of the emitters. The second approach uses doping of specially prepared quantum dots (core/shell/PMMA hybrid particles) into polymer host matrix before processing of the microresonators. The third approach utilizes dip-pen nanolithography (DPN) for highly localized deposition of quantum dots on the rim of the resonator. All the presented approaches open new techniques for the integration of quantum emitters into high-Q polymer resonators.

3.1   Nanocrystal Quantum Dots as a Gain Medium

3.1.1   Basics of nanocrystal quantum dots

In this section the overall basics of quantum dots as a gain medium is discussed. The text is mainly based on the detailed investigation performed on the charge carrier dynamics and optical gain conditions in nanocrystal quantum dots presented in the work of V. I. Klimov et al [24] and [74, 75].

In semiconductors the periodic crystal potential imposes restrictions on the wave vector (k-vector) of de-localized electron wave functions according to the Bragg conditions. This results in a band gap or forbidden states between the highest occupied valence band and the lowest unoccupied conduction band. In a macroscopic scale, the energy states within each band are closely spaced and considered as continua. In this case the carrier distribution (which is described by the density of states) increases for both bands with distance from the band edges. The carrier occupation probability in such bulk semiconductors is given by the temperature-dependent Fermi-Dirac distribution. At thermal equilibrium, there will be a few free electrons at the lowest conduction band and holes at the highest edge of the valence band.

Carriers (electrons or holes) excited across the forbidden band gap by photons of sufficient energy. After the excitation fast thermal interaction leads to freezing of the excited electron to the band edge states by carrier and phonon interactions and

finally results in the recombination of the electron and hole via the emission of a photon with the same energy as the band gap. This process is only efficient in direct band gap semiconductors (where the lower conduction band and the top of the valence band have similar wave vector, k) due to momentum conservation. The temperature-sensitive carrier distribution makes unstable emission characteristics and leads to temperature-dependent (sensitive) physical properties like threshold of lasing. When the size of the crystal is decreased (few nanometre scale), the spacings between electronic energy levels increase. The transition into this quantum confined regime is not sharp. In principle a natural length scale is defined to estimate the size of the crystal size in which the quantum effects start to play a role. When an electron-hole (e-h) pair is created, the two carriers interact through Coulomb force (the e-h pair is called exciton) and can analogously be described like the proton and electron in a hydrogen atom. The distance between electron and hole is referred to as the exciton Bohr radius (a_{eh}) and is given in terms of hydrogen Bohr radius (a_H) as:

$$a_{eh} = \varepsilon \frac{m_e}{\mu_{eh}} a_H \qquad (3.1)$$

here m_e is the electron mass, μ_{eh} is the reduced effective mass of the exciton and ε is the dielectric screening of the electric field. For instance, consider CdSe QDs, using the effective masses of the electron 0.12 m_e and hole 0.45 m_e, the reduced exciton mass is 0.095 m_e. Applying the dielectric constant of CdSe, $\varepsilon \approx 9.7$ [76] and the hydrogen Bohr radius $a_H = 52.9$ pm, the exciton Bohr radius is found to be 5.4 nm. When the crystal size of CdSe is below this value, the exciton enters the regime of strong confinement in which the crystal boundaries play a role in the physical properties of the semiconductor. Two of the most common features are band gap broadening and quantization of electronic energy levels. Some of the quantum effects are also possibly apparent even in a weak confined regime where the crystal size is still greater than the exciton Bohr radius (few nanometre bigger than a_{eh}).

The energy states of a QD can be modelled by considering the effect of crystal lattice and the boundary conditions. With in the effective mass model the conduction and valence bands can be approximated by isotropic bands and a simplified picture of the entity as a free particles (electron or hole) describes the influence of the potential of the periodic crystal by their effective mass, which is the measure of their band curvatures. Then the carrier wave functions can be expressed as a series of Bloch functions with unit cell coefficients including the periodicity of the crystal lattice. The unit cell components can be determined from the bulk model. The other part of the wave function is in the form of a particle in a sphere model. The electron and hole treated as free particle in a spherical box of infinite potential barrier. And the envelop function satisfying the spherical boundary condition of the quantum dot is given as a product of spherical Bessel functions, $j_l(r)$, and spherical

harmonics,$Y_l^m(r,\theta,\phi)$ [77]:

$$\psi(r,\theta,\phi) = A\frac{j_l(k_{n,l},r)Y_l^m(\theta,\phi)}{r} \tag{3.2}$$

where A is a normalization constant. The spherical boundary condition imposes quantization of wave vector $k_{n,l} = \eta_{n,l}/a$, where $\eta_{n,l}$ is the nth root of $j_l(k_{n,l},r)$. For instance the first lowest roots takes the form $\eta_{0,0} = \pi$, $\eta_{0,1} = 4.49$, $\eta_{1,0} = 2\pi$.

In analogy to the atomic model the envelop function is characterized by quantum numbers n= 1, 2, 3..... , and l= $0 \rightarrow S$, $1 \rightarrow P$, $2 \rightarrow D$ . . . and m. The electron (hole) energy associated with the eigenstate described above takes the form:

$$E_{n,l}^e = \frac{\hbar^2}{2m_e}k_{n,l}^2 = \frac{\hbar^2}{2m_e}\frac{\eta_{n,l}^2}{a^2} \tag{3.3}$$

and

$$E_{n,l}^h = \frac{\hbar^2}{2m_h}k_{n,l}^2 = \frac{\hbar^2}{2m_h}\frac{\eta_{n,l}^2}{a^2} \tag{3.4}$$

These equations clearly show that the quantum energy levels of the quantum dots are proportional to $1/a^2$. There is also Coulomb attraction potential between the negatively charged electron and hole ($\propto 1/a$) in an exciton, which is smaller than the confinement energy ($\propto 1/a^2$) in the strong confined regime of the quantum dot. In this regime the electron and hole are treated independently and the Coulomb term E_c is simply considered as a first order energy correction for the total energy of the exciton.

Therefore the total energy of the exciton in a strongly confined regime is the sum of the band gap energy, the hole and electron confinement energies, and the Coulomb binding energy. Mathematically it is given by

$$E_{exc}(n_el_e, n_hl_h) = E_g + E_{n,l}^e + E_{n,l}^h - E_c \tag{3.5}$$

The energy states are described by the quantum numbers n_el_e, and n_hl_h for the electron and hole states respectively. The lowest excitonic state is labelled accordingly as $1S_e1S_h$.

To see the effect of the confinement energy, let us consider CdSe QDs of radius about 2.6 nm (similar to the size of QDs used in this work). The bulk band gap energy E_g of CdSe is 1.74 eV at room temperature and about 1.84 eV at 0 K. Using equation 3.3 and 3.4, the confinement energies of the hole and electron are 0.12 eV and 0.46 eV respectively. The Coulomb binding energy E_c for the first excited state is given
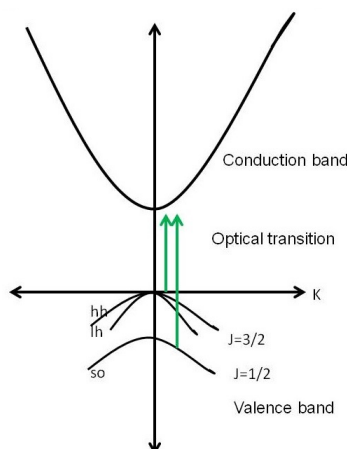
Figure 3.1: Bulk band structure of QDs assuming independent valence band states.

by $1.8e^2/4\pi\varepsilon\varepsilon_o a \approx 0.1$ eV [78]. Hence, the net increase in the energy of the quantum dot (blue shift of the band gap) due to the quantum size-confinement is around 0.48 eV. Further reduction in the size increases the effective band gap to cover the wide range of the visible spectrum [71].

Within the effective mass approximation the conduction band can be considered as simple parabolic band and its lowest electron states are given by 1S, 1P, and 1D. The valence band structure is much more complex and its description needs an additional quantum number $J = l + s$, where s is the spin quantum number. For instance, in the case of CdSe QDs there is a 6-fold degeneracy of the 4p atomic orbitals of Se in the diamond-like band structure. Due to the strong spin-orbit coupling, the degeneracy is lifted and splitting occurs by an amount $\Delta \simeq 0.42$ eV [79] into a band edge 4-fold degenerate $J_h = 3/2$ band and a split-off (SO) leading to 2-fold degenerate $J_h = 1/2$ band, as shown in Fig. 3.1. The notation $J_h = l_h + s_h$ is the quantum number for the total angular momentum (the hole orbit, $l_h = 1$, and spin $s_h = \pm 1/2$). The band edge state $J_h = 3/2$ band is again split into two sub-bands (the heavy-hole (hh) and light-hole (lh) band). For diamond-like crystals the hh and lh sub-bands intersect at k = 0 but quantum dots like CdSe has a Wurtzite hexagonal crystal structure leading to lifting of the degeneracy further by a small crystal field, resulting in a shift $\triangle_{cf} = 40$ meV [79].

In the above discussion each valence sub-bands are treated independently but in reality the hole states are mixed due to the underlying quantum mechanical coupling [74]. Hence, the quantum nummber J_h describing the individual sub-bands is not conserved. The total angular momentum of either electron or hole (M_e or M_h) has two contributions; (I) a unit-cell contribution (J) due to the underlying basis

which forms the bulk bands; and (II) an envelop function contribution (L) due to the particle in a sphere orbitals. In the previous description it is assumed that the quantum number describing each valence sub-band (J_h) and each envelop function L_h are conserved. However, when the Luttinger Hamiltonian, describing the bulk valence band, is combined with a spherical potential, mixing between bulk valence bands occur. This effect, origionally shown for bulk impurity centers, also mixes QD hole states [74]. Only parity and the total angular momentum defined by $M_h = J_h + L_h$ are conserved. The mixing occurs among states of common M_h and parity [74]. Each QD hole states with total angular momentum M_h is a mixture of three valence sub-bands (valence band mixing) and envelop function L_h and $L_h + 2$ (S-D mixing) [74].

The electronic structure of QD states is depicted in Fig. 3.2. Unlike valence band structure the conduction band has not involved in state mixing process and have more largely spaced energy levels. Fig. 3.2 shows the optical transition from 1S, 2S, and 1P transition. 1S transition is represented by excitonic notation of $1S_{3/2}1S_e$, and 2S and 1P are represented by $2S_{3/2}1S_e$ and $1P_{3/2}1P_e$ respectively.

Band edge optical properties of quantum dots are mainly dominated by optical transitions involving the first excitonic state, $1S_{3/2}1S_e$, usually known by the name band-edge exciton. 2-fold degeneracy from electron and 4 fold degeneracy ($2M_h+1$) from hole state lead to 8-fold degeneracy of the band-edge state. In practice, QDs like CdSe nanocrystal lift this degeneracy due to the crystal field of the Wurtzite lattice structure as discussed above and e-h exchange interactions as described in [80]. These result in a 5 fold exciton fine structure as shown in Fig. 3.2 inset.

Due to strong spatial carrier-overlap in smaller QDs, the exchange interaction between electron and hole is indispensable and cause the single carrier quantum numbers, M_h and M_e not to be conserved. In such situation one must consider the combined e-h angular momentum, $N = M_h + M_e$[1]. Since $M_h = 3/2$ and $M_e = 1/2$, N= 2 state leads to 5-fold band edge exciton state degeneracy and N= 1 state results in a 3-fold degenerate state. As the result of the hexagonal crystal lattice and imperfect spherical quantum dot shape, the isotropy is lifted and the projection of N along the nanocrystal axis then determines the energy states and characterizes the fine structure. For N= 2 the 5 energy states are labelled as $|N_m|=$ 0, 1, 2 and for N= 1 state $|N_m|=$ 0, 1. These energy levels are denoted by $|N_m|$ with a superscript $'U'$ for the upper N = 1 sub-level and $'L'$ for the lower N = 2 sub-level as shown in Fig. 3.2 inset. The band edge exciton exhibits two closely spaced energy states

---

[1]The total electron-hole pair angular momentum N has contribution from both electron M_e and hole M_h. Each carrier angular momentum M can be further broke down into a unit cell components J, due to the atomic basis l and spin s of the particle and an envelop function L due to particle in a sphere orbital.
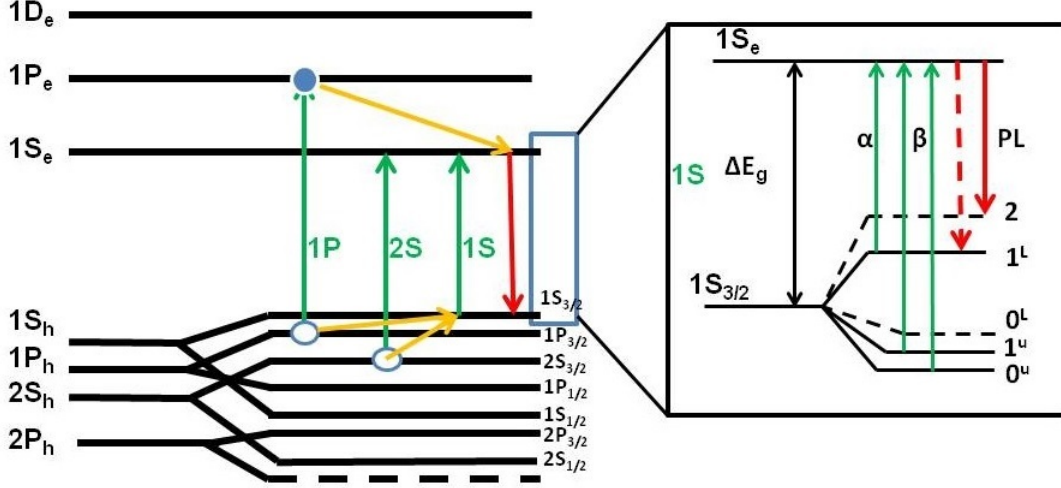
Figure 3.2: Electronic states and the corresponding optical transitions in CdSe QDs (including valence state mixing). The first lowest three transitions labelled 1S, 2S, and 1P and carrier relaxation are shown. Inset: Fine structure of band edge 1S exciton($1S_{3/2}1S_e$) transition. The dashed lines are optically passive states. The arrows show Optical transitions (green and red). α and β of 1S absorption band is represented by green arrows and the corresponding band edge PL emission is indicated by red arrows.

which depend on the size of the dot. The investigation of the fine structures and its dependency on the size of the dots is well-studied for CdSe NQDs [81]. Out of the described five sub-levels, the two sublevels 2 and 0^L, are optically passive and the rest sub-levels gives three absorption transitions: α absorption is a small contribution from 1^L and β absorption are the two largest contributions from 1^U and 0^U. This explains the observed fine structure in the first absorption band of the colloidal QDs (for more information read [81]).

The lowest hole state has a net spin projection $M_m = 2$ and photons have spin 1, hence selection rule dictates that after the hole has rapidly relaxed down into the 2-state, it cannot recombine with the electron. This optically forbidden transition is known as the dark-exciton state. It was observed that the dark state has a huge life time reaching up to $\sim 1~\mu s$ for CdSe at cryogenic temperatures, which is much more than the bulk life time of the semiconductor (~ 1 ns) [82]. At room temperature most of the holes are thermally transferred into the bright excitonic-state 1^L sub-level which results in PL emission with shorter lifetimes about 10-20 ns. The bright-exciton state transition is represented by a red dashed arrow in Fig. 3.2 inset. Its energy is the same as the α absorption line. Hence, there is a spectral overlap between absorption and emission at ambient room temperature conditions.

The spectral overlap between emission and absorption hinders the development of optical gain, which in turn prohibits lasing. A further red-shifting of the gain is practically possible by biexciton interactions as discussed in the next section.

3.2   Gain and Loss Mechanisms Relevant for Lasing

In the following section the development of optical gain, the loss mechanisms and also the technique to rise-up the stimulated emission build up time for strongly confined QD-lasing are discussed.

As it is described in ref. [83] the emission characteristics and the colloidal QDs absorption α_o with its $1S$ absorption peak is shown in Fig. 3.3 (a) for CdSe QDs of radius 2.5 nm. Pumping the sample with pulsed laser of relatively higher power leads to state-filling and the absorption line is reduced as indicated by α [83]. The gain which is indicated by the black area is around 1.95 eV and is Stoke-shifted from the 1S absorption line. The gain region is also red-shifted from the PL emission maxima. This justifies the observation of gain-induced amplified spontanous emission (ASE) in the lower energy side of the PL spectra. In Fig. 3.3 (a) the ASE and the PL emission peak is separated about 55 meV.

The observation of the relative change in the absorption with the increase in the pump power at 1S spectral absorption position (circles) and optical gain (squares) is depicted in Fig. 3.3 (b). The pump power is given in terms of excited e-h pairs per dot on average $\langle N_{eh} \rangle$, which is obtained from the absorption cross section σ_0 [84]. When the absorption change $-\Delta\alpha$ exceeds the ground-state absorption α_0, optical gain is developed as indicated by the horizontal line in Fig. 3.3 (b). The two band curves can be explained from the exciton fine structure state-filling arguments. As clearly explained in the previous section the band edge hole states are 4-fold degenerate (one absorbing and one emitting state) and the electron $1S_e$ state is a 2-fold spin degenerate state. The relative absorption change is given as the sum of electron and hole occupation numbers $< N_e >$ and $< N_h >$ respectively [75, 84]:

$$-\frac{\Delta\alpha}{\alpha_0} = < N_e + N_h >$$
(3.6)

The absorbing transition is mainly contributed from the 2-fold degenerate electron states contribute as the excited holes relax rapidly into the emission state. This re-
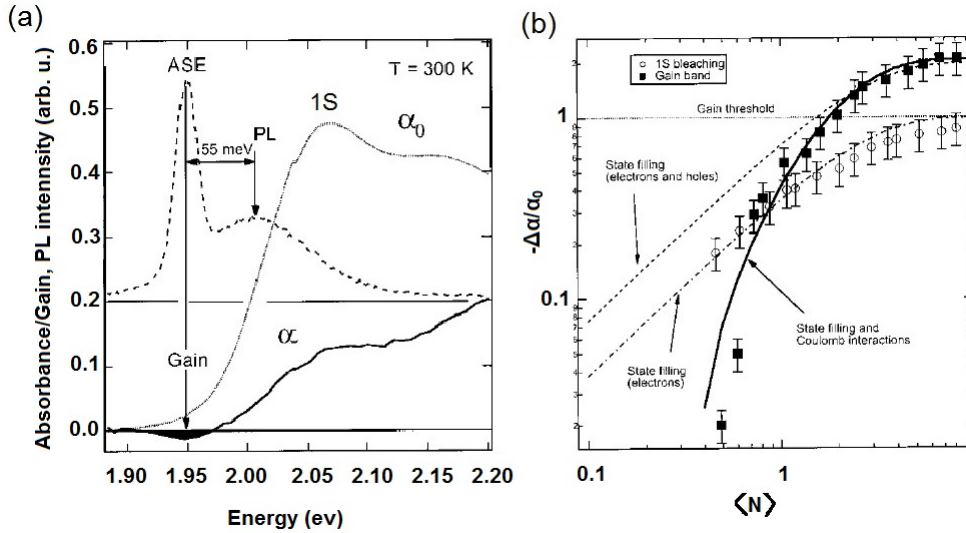
Figure 3.3: Biexcitonic optical gain in CdSe QDs. (a) Absorption spectrum of 2.5 nm radius closed-packed film of CdSe QDs. The pump-induced bleaching from initial state α_o to excited state α leads to gain represented by black area around 1.95 eV. The corresponding PL emission, dashed line, exhibit a clear red shifted amplified spontaneous emission (ASE). (b) Pump-intensity dependence of normalized absorption changes for a CdSe nanocrystal quantum dot of radius 2.5 nm measured at 80 K at the position of 1S absorption maxima (open circles) and the solid squares are maximum of the gain band. Experimental data are fitted by considering only state filling model alone (dashed and dashed-dotted lines) and also using state filling model along with coulomb interactions (solid line) (diagrams taken and modified from Klimov et al. [82, 83]).

stricts the state filling to a maximum of $< N_e >= 1$ and $< N_h >= 0$ and yields good fitting as indicated by dashed-dotted line in Fig. 3.3 (b) to the 1S absorption bleaching (circles) behaviour. The state-filling model for the emitting transition involving the 4-fold hole states shows the access of optical gain at a pump level starting from 1.55 excitons per dot on average. But the experimental data represented by circles show an increase in the absorption bleaching before optical gain is developed.

This effect can not be explained by the state-filling model alone. When more than one e-h pair is excited in a quantum dot, the enhanced quantum spatial confinement leads to Coulomb interactions between excitons. This interaction cause a shift in the energy of the excitons. In the most common case there are two e-h pair excited in a single dot. It is called biexciton.

The schematic diagram of exciton and biexciton states are shown in Fig. 3.4. The interaction between the two excitons reduces the biexciton energy E_{2x} by δE_{2x}.
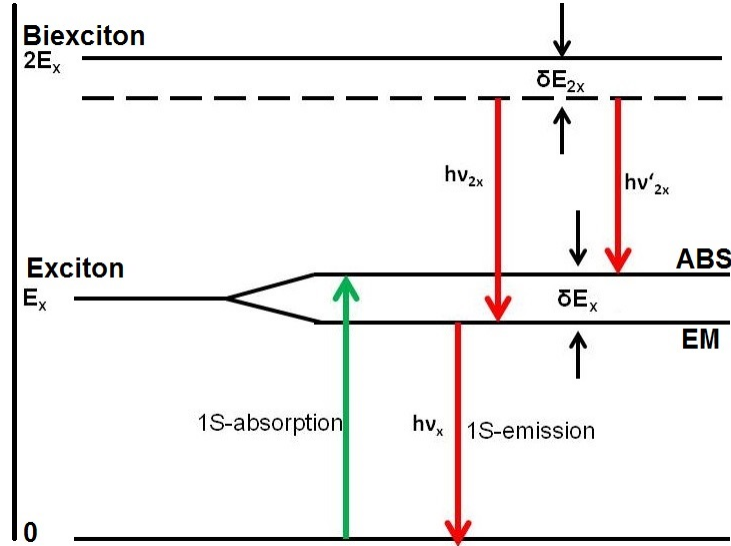
Figure 3.4: Energy level digram of biexciton transition. The Coulomb interaction between the two excitons reduces the biexciton energy E_{2x} by δE_{2x}. This decreases the biexciton emission $h\nu_{2x}$. A further reduction in the energy of the emitted photon occurs due to the the energy difference between the ground state and excited state exciton. This transition leads to an emission of low energy photon $h\nu'_{2x}$.

This results in a a decrease in the biexciton emission $h\nu_{2x}$. Further red shifting is possible due to both δE_{2x} and the energy difference between the ground-state and excited state exciton. This transition is accompanied by an emission of low energy photon $h\nu'_{2x}$. More than 2 electron-hole pairs in a single dot is unstable and all multi-excitonic states can be neglected [85]. In general these two basic mechanisms explains why the biexcitonic enhanced optical gain in strongly confined quantum dots is manifested at the lower energy side of the PL spectrum.

After the development of biexcitonic assisted optical gain, the observation of lasing depend on the loss mechanism of strongly confined quantum dots. As the size of the quantum dots decrease the spacing between the energy level become much bigger than available phonon energies. Hence carrier relaxing down to the band edge state for the population build-up is quite difficult. This well known effect is called phonon-bottleneck. This problem was investigated and it was found from ultrafast transient absorption (TA) pump-probe measurements that excited electrons in strongly confined QDs relax down to the band edge state via Auger type interactions in sub-ps scale [86]. This Auger type interaction is the dominant type of interaction in strongly confined quantum dots. Unlike the electronic states on the conduction band, the valence band has smaller spacing between energy levels and it was shown in ultra-fast PL experiments [87] that fast phonon-assisted hole relaxation is still
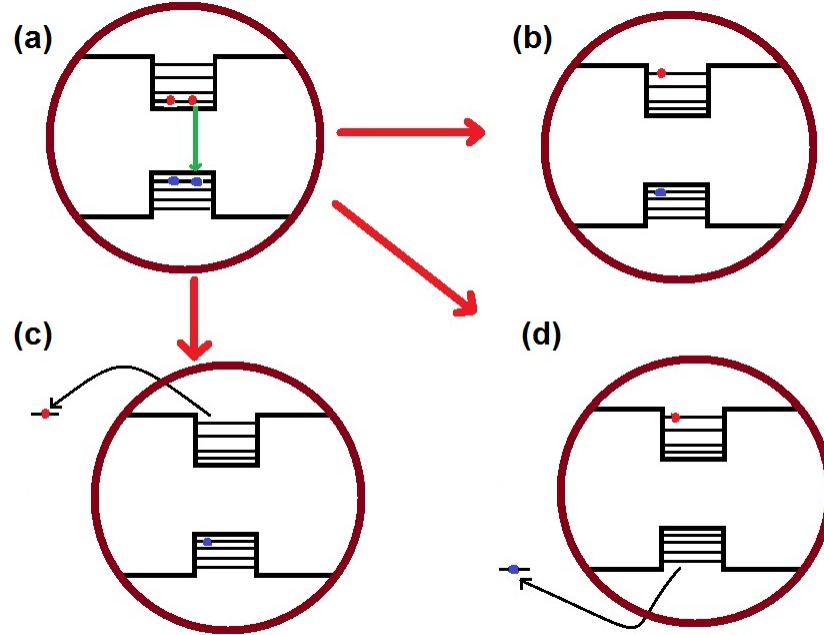
Figure 3.5: Auger process in biexcitons. Instead of the electron recombine with the hole radiatively (a) , the energy is given to the third particle (electron or hole) and the recombination become non-radiative. The third particle which gets the energy from the biexciton either re-excited to higher energy levels (b) or can also be ejected out of the dot. The latter is called Auger ionization (c) and (d).

active like in bulk semiconductors.

Another non-radiative loss mechanism that prevent lasing is carrier trapping by surface defects. Which is also the result of the high surface-to-volume ratio of QDs (due to their small sizes). This loss mechanism is the dominant effect for single excitonic state (at low excitation level). As reported from ultra-fast TA measurements, surface trapping can be overcome by surface passivation. Usually capping the QDs (e.g CdSe) by inorganic larger band gap semiconductors (e.g ZnS, CdS) results in a huge improvement on the effect of surface trapping by defect states [88]. It has also been reported from time-resolved PL measurements that surface losses are mainly dominated by hole trapping [87]. Surface trapping can also affect the optical gain by a process called photo-induced absorption [89]. Using TA pump-probe experiments the development of optical gain and the effect of photo-induced absorption was investigated. Since the pump power corresponds to the average excited e-h pairs per dot, its increase leads to the decrease of absorption at the emitting transition 1^L (Fig. 3.2 (b) inset) and then absorption is expected to decrease until optical gain is developed

(i.e. negative absorption is reached). In contrast, it was found that for QDs of size less than 2.3 nm in hexane solution [89] the increase in pump power leads to an initial decrease in absorption and after a while increased again before the gain is reached. This gain suppressing effect of surface traps could be reduced by inorganic surface passivation and also the change of surrounding medium. The surrounding medium (like the solvent used) has a role as it intermediates the coupling between a trapped carrier and an unoccupied state in the surrounding environment [89]. For larger quantum dot sizes the gain magnitude increases and optical gain can also occur at lower thresholds, hence surface trapping will have less effect as compared to smaller dots.

All the above loss mechanisms are contributing only partly and the most common effect that suppresses the gain and inhibits lasing is the multi-particle Auger process. It is a three particle process in which instead of the radiative recombination of an electron with the hole, the energy is transferred to a third carrier (electron or hole) leading to non-radiative relaxations. The third particle either re-excited to higher energy levels Fig. 3.5 (b) or can also be ejected out of the dot (Auger ionization) as shown in Fig. 3.5 (c) and (d).

The Auger process is insignificant in bulk semiconductors and weakly confined quantum dots. For bulk semiconductors on average there is one exciton per excitonic volume V defined by Bohr excitonic radius a_B ($V \sim a_B^3$). Above this number the carriers do not form exciton gas and a strong screening effect reduce the Coulomb interaction. But in strongly confined QDs where the radius is smaller than a_B many excitons can occupy a volume smaller than V. This leads to a decrease in the screening effect, an increase in the overlap of between carrier functions and enhanced Coulomb interaction. On the other hand due to the nanometre size of the QDs there is no wave vector carrier momentum conservation. Which is also interpreted as a breaking of translational-symmetry, enhancing also the Auger effect [90, 91]. The Auger decay is strongly dependent on the size of the emitter. Analytical investigation and a physical solution for overcoming this non-radiative process for developing optical gain and lasing was well investigated by Klimov and co-workers [24] as discussed below.

Considering that the Auger process is a three particle process, its decay rate is proportional to the density of carriers n_{eh}^3, and the life time τ is given by:

$$\frac{d}{dt} n_{eh} = -C_A n_{eh}^3 \tag{3.7}$$

$$\tau = \frac{1}{C_A n_{eh}^2} \tag{3.8}$$

where C_A is the Auger constant. As the carrier density decreases the life time increases. If the QD size is only a few nm of radius a, only a small number of excitons can be excited at the same time. Hence Klimov and co-workers [24] considered the Auger decay as a quantized steps. By labelling each exciton number, N_{eh}, a corresponding lifetime τ_N, and using the fact that $n_{eh} = N_{eh}/V_{QD}$, it is clear that the decay life time varies as $1/N_{eh}^2$ and with the size of the QD as a^6. However in QDs it has been found that the Auger constant follows a^3 proving that the constant depend on the size of the dot as a^3:

$$\tau = a^3 \tag{3.9}$$

$$C_A \propto a^3 \tag{3.10}$$

It was reported that Auger constants of about 2-70 nm^6/ps were obtained by changing the radial size of the QD between 1.2 and 4.1 nm respectively [85]. It was also shown that the non-radiative Auger life time of doubly excited QDs can be shortened from 360 to 6 ps as the radial size of the QD decreases from 4.1 to 1.2 nm. The biexcitonic life time defined by τ_2, is similarly expressed as $\tau_2 = \beta a^3$, where $\beta = 4\pi^2/9\gamma \approx 4.4$ $psnm^{-3}$ [85]. An Auger constant of 19 nm^6/ps and the associated biexcitonic decay time $\tau_2 \approx 80$ ps is observed for CdSe QDs of radius about 2.6 nm. The higher exciton numbers, 3- and 4-excitons states, are unstable and have a decay time about 35 and 25 ps respectively [85]. This explains the fact that major contribution from higher excitonic states are dominantly from biexcitons.

Population inversion and the development of optical gain are only possible when the relaxation down to the emitting ground state is faster than the Auger process time. Despite very short time constants the Auger process does not inherently inhibit lasing. Lasing can still be optimized via stimulated emission if its build-up time is faster than the Auger biexcitonic decay. The rate of stimulated emission build up is proportional to the concentration of the QDs (incoming photon flux). Klimov et al [24] derived a lower limit of the concentration of the dots necessary for the build up of stimulated emission faster than the Auger process by comparing the associated life times. The Auger decay time of strongly confined CdSe biexcitons can be described as $\tau_2 = \beta a^3$. The stimulated emission build-up time, which is defined by τ_s, is inversely proportional to the gain magnitude g and is given by $\tau_s = n/gc$, where c is the speed of light in vacuum and n is the index of refraction of the media. The gain coefficient is a function depending on the concentration n_{QD} of the quantum dot as $g = \sigma_g n_{QD}$, where σ_g is the gain cross-section. Hence the stimulated emission build-up time can be expressed using the volume fraction of semiconductor material in the sample ($\xi = 4\pi n_{QD}a^3/3$) as:

$$\tau_s = \frac{4\pi a^3}{3}\frac{n}{\xi\sigma_g c} \tag{3.11}$$

Assuming that the gain decay is mainly due to the intrinsic two-pair Auger recombination τ_2, stimulated emission can only be occurred if its build up time τ_s is less than τ_2. This leads to the expression for the concentration threshold condition for lasing (defined by the volume fraction):

$$\xi > \frac{4}{3\sigma_g c\beta} \tag{3.12}$$

From previous studies, $\beta \sim 5$ ps nm^{-3} and using the gain cross section $\sigma_g \approx 2 \times 10^{-17} cm^2$, calculated for QDs of radius 1.3 nm, it is found that the required volume fraction of the semiconductor material is $\xi > 0.2$ %. Therefore with concentrations satisfying the above conditions one can overcome the Auger process and the development of stimulated emission and lasing is possible. The next section discusses the techniques to integrate different QDs into microcavities for the realization of QD-lasers.

3.3   Colloidal Quantum Dot Microlasers

Polymeric resonators are well suited for the integration of quantum dots. For the realization of low threshold QD lasers, the gain medium has to be incorporated into the cavity without deteriorating the high Q-factor of the resonators.

The attempt to dope the polymer matrix with the QDs is quite difficult due to the phase separation of the emitters from the host matrix. So it is indispensable to add special ligands to the surface of the dots to maximize their solubility. In this section different routes for the achievement of QD-lasers (with and without surface chemistry of the dots) are presented. For the integration of quantum dots into high-Q polymeric resonators three different techniques are utilized: quantum dot/polymer sandwiched structures, core/shell/PMMA hybrid particle doped cavities and highly localized quantum dot deposition using dip-pen nanolithography techniques on the rim of the resonator. The fabrication and optical characterization of QD integrated polymeric microlasers are central point of the work and presented as follows in the next subsections.

3.3.1 Quantum dot/polymer sandwich microlasers

The coupling of strongly confining bare core QDs (e.g. bare core CdTe QDs) to the eigenmodes of the WGM cavities is challenging. Even if non-radiative Auger process can be overcome by high concentration of the emitters, bare core QDs show a quick bleaching of the emission due to photo-oxidation for example as in water droplet WGM resonators [21] and surface traps due to their poor surface passivation (no core). As a result the QDs do not show lasing for both continuous wave (cw) and pulsed excitations as the damage threshold of this type of QDs is much lower than the one required for lasing [21–23].

By the use of QD/polymer sandwich WGM resonator structures[2], a high density of emitters can be incorporated into the cavities. The integration mechanism does not require surface functionalization of the emitters and the PMMA polymer prevent the QDs from photo-oxidation. The CdTe QDs used in the experiments (Plasma Chem, Berlin) easily form a colloidal solution in water and are terminated with a $-COOH$ group. The nanoparticles have a size of 3.3 nm which is smaller than the excitonic Bohr radius of CdTe ($\backsim$ 7.3nm) [92]. Hence, the emitters are in the strongly confining regime. The emission peak wavelength of the QDs is in between 580-590 nm.

Fabrication

For the realization of a microlaser the CdTe QDs are integrated into a high-Q feed-back cavity. The fabrication process of polymeric resonators is discussed in chapter 2. QD/polymer sandwich structures follow similar fabrication techniques except some modification steps are required to integrate the emitters. As it is shown in Fig. 3.6, in the first step the PMMA (MicroChem PMMA 950k A7, dissolved in anisole) is spin coated on a silicon wafer (with a PMMA layer thickness of nearly $1\,\mu m$). The sample is heated to 110 °C to reduce the solvent content. Then we spin coat three layers of $9\,\mu M$ water soluble CdTe QDs. Heating the sample at 110 °C for 15-20 s reduces the water content. Once again spin coating PMMA (in anisole) on the QD layers result in a high concentration of CdTe QDs sandwiched between two PMMA layers. Then disks on sandwiched structures are patterned by e-beam lithography (with a dose current of 1 nA). After e-beam exposure and chemical development of the PMMA, the silicon is isotropically etched with XeF_2. This results in QD-sandwiched PMMA microdisks standing on silicon pedestals. The resonators used for sandwich structures have a diameter of $26\,\mu m$ and $47\,\mu m$ in size.
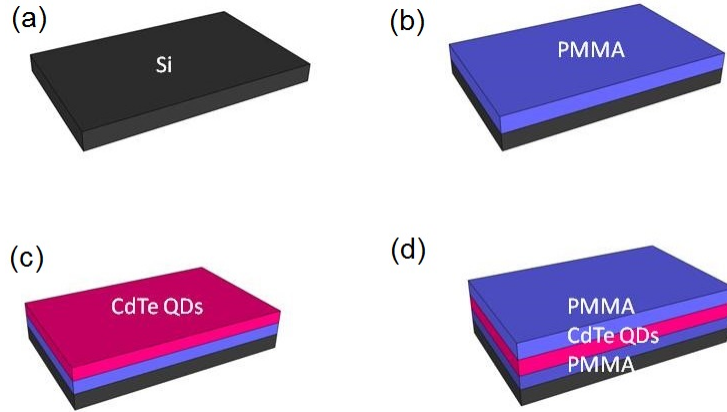
Figure 3.6: QD/polymer sandwich structure. (a) A silicon wafer. (b) PMMA layer of about 1 μm thickness is spin coated on a silicon wafer. (c) Layer by layer deposition of water soluble CdTe QDs are made by spin coating. (d) Spin coating another PMMA layer leads to PMMA-QDs-PMMA sandwiched structure.

Optical characterization

Polymeric WGM resonators confine optical field of the cavity near the rim of the resonators. The sandwiched cavities have Q-factors of about 5.4×10^4 at wavelength around 635.1 nm as shown in Fig. 4.7 (b). The Q-factor can be increased by one order of magnitude if a thermal reflow process is used. The Q-factor of cavities containing QDs are lower than passive disks due to the scattering and absorption of cavity photons by the CdTe QDs. The Q-factor is measured from the full-width at half maximum of the Lorentzian-shaped resonances observed from the transmission spectra collected from an evanescently coupled tapered fiber. The free spectral range, which is evaluated from the periodic repetition of the modal pattern is 1.79 nm, as shown in Fig. 4.7 (a). This is in agreement with the theoretically expected value of 1.83 nm for a $47\,\mu m$ diameter polymeric disk. Besides the fundamental modes, several higher-order modes are also observed.

Free-space excitation

The fluorescence measurements are done in a free-space micro-photoluminescence (μ-PL) setup. The schematic diagram is shown in Fig. 3.8. The pump laser beam is focused on the sample at an angle of 45° with respect to the normal of the sample

---

[2]The results presented in this section have been published in [15].
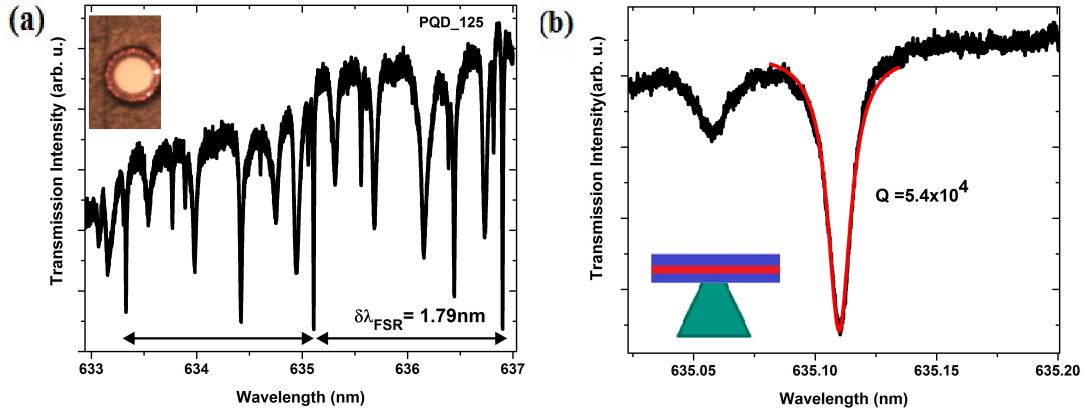
Figure 3.7: Mode spectrum and Q-factor of a microdisk resonator with a diameter of $47 \, \mu m$ in the 630 nm wavelength range. (a) Transmission spectrum through an evanescently coupled tapered fiber shows WGM resonances. Inset: During coupling the light is observed while circulating the resonator. (b) The Lorentzian fit to the modes of QD-sandwiched cavities show Q-factor reaching upto 5.4×10^4 at wavelength around 635.1 nm.

surface. The microcavities were pumped either with continuous wave (cw) emission at 442 nm from a HeCd laser or pulses from a frequency-doubled neodymium-doped yttrium orthovandate (Nd:YVO$_4$) laser with a pulse width of 10 ns and a wavelength of 532 nm. The emission from the sample is collected via a microscope objective of NA=0.4 ($\times$50) and the exact position of the sample and the excitation spot (diameter $\sim 60 \mu m$) is monitored by a camera. The spectral output is analysed using a spectrometer (spectral resolution of 30 pm) equipped with CCD (charge coupled device) camera. The pump intensity for pulsed excitation is controlled by a Pockels cell along with a polarization filter. The cw excitation intensity is adjusted by neutral density filters.

Excitation of the QDs/PMMA sandwich cavities with a cw HeCd laser shows WGM features on the bulk emission of the QDs. Fig. 3.9 (a) shows the PL intensity from a $26 \, \mu m$ diameter cavity pumped with 8.5 mW cw power. The periodic narrow WGM features are clearly observed on the photoluminescence background of the QDs. The coupled optical modes are more pronounced on the lower energy side of the spectrum due to the lower absorption of the QDs. Due to the excitation of the whole sample area huge build up of the spontaneous emission of the bulk QDs is observed. Again, the modal spectrum is quite complex with a free spectral range of $\delta\lambda_{FSR}$ =2.62 nm at a wavelength of 589.5 nm as indicated by the arrows in Fig. 3.9 (a).
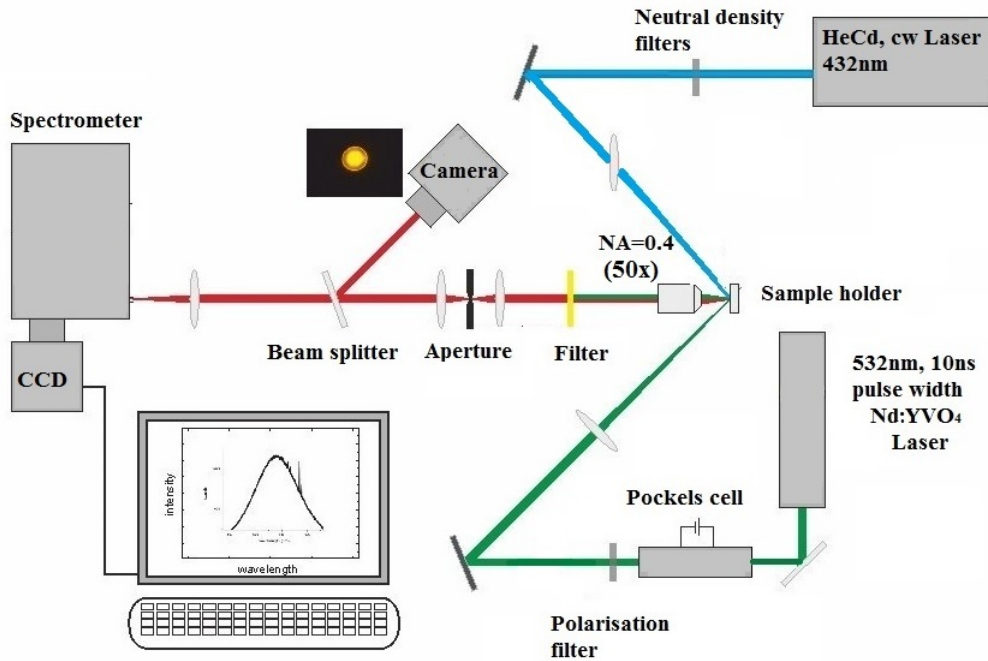
Figure 3.8: Micro-photoluminescence setup for free-space excitation measurement using either a cw or a pulsed laser. The pump laser beam is focused onto the sample and the emission from the sample is collected via a microscope objective, monitored on a camera and analyzed by a spectrometer.

After investigation of the WGM resonances, the pump power is increased to observe a possible cw lasing from the sample. The PL shows a certain increase in the fluorescence and emission linewidth of the QDs until 10 mW. Then a further increase in excitation power leads to photo-bleaching of the QDs. This is manifested by a decrease in PL emission and a blue shift in the peak emission wavelength for an increase in pump energy [93, 94] as depicted in Fig. 3.9 (b). The bleaching is irreversible and results in permanent loss of the PL intensity. These kinds of irreversible losses of PL intensity of colloidal QDs are also observed for other different kinds of QDs [95]. The permanent loss of the PL intensity can originate from thermally induced permanent structural changes, giving rise to trap states [95]. Also charging (ionization) of the QDs from carrier tunnelling and Auger ionization can contribute to this effect [96, 97].

The resonant cavity modes also show a blue shift for increasing excitation power. The shifts observed between two consecutive fundamental modes are not equal for different excitation power, hence the free spectral range also changes. Fig. 3.10 shows the shift in the resonance modes and the accompanied change in the free spectral range for two different excitation powers, 20 mW and 30 mW (upper and lower PL
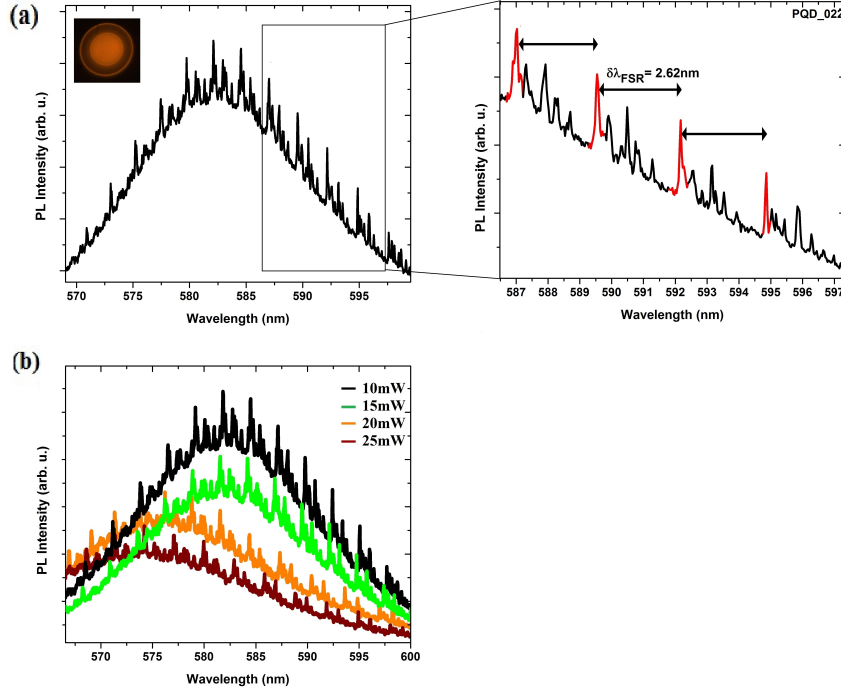
Figure 3.9: (a) PL spectrum of CdTe QDs integrated into a polymeric sandwich micro-cavity with a diameter of $26\,\mu m$. The mode structure is complex as shown on the left side of (a), the red peaks show the consecutive azimuthal modes and the arrows show the free spectral range of the resonant mode ($\delta\lambda_{FSR} = 2.62nm$ near 589.5 nm). The inset on the left of (a) shows the fluorescence image of the QD/PMMA sandwich microdisk. (b) Increasing the pump power leads to a certain increase in the fluorescence and emission linewidth of the QDs until 10 mW. A further increase in excitation power leads to a decrease in PL emission and a blue shift in the peak emission wavelength.

spectrum respectively), above the photo-bleaching threshold value. The distance between the two modes observed at 587.34 nm and 590.4 nm is 3.06 nm for a pump power of 20 mW and increasing the excitation power to 30 mW leads to a blue shift of the modes to 585.85 nm and 588.81 nm respectively, corresponding to a decrease of the spectral distance to 2.96 nm. The resonance wavelength of a given mode depends on the diameter of the cavity, the effective index of refraction and the surrounding medium. PMMA has a large negative thermo-optic coefficient dn/dT = -1.05$\times$ $10^{-4}/K$ [98], so an increase in temperature of the cavity due to optical pumping is expected to dominate the blue shift of the cavity modes.

Pulsed pump sources can avoid bleaching as compared to cw sources, as the time between pulses enables the relaxation of the excited states of the QDs and also
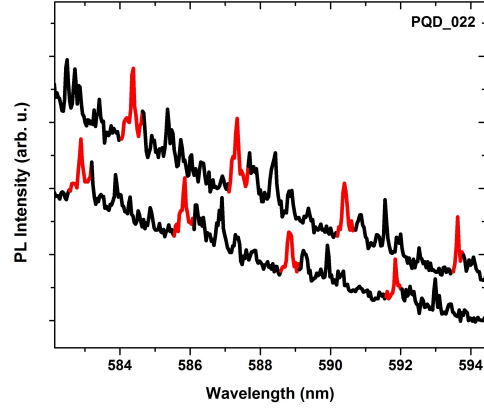
Figure 3.10: Blue shifting of the resonance modes for high excitation power. The upper (lower) spectrum is recorded at 20 mW (30 mW) cw excitation power. The red color shows the fundamental WGM modes.

pulsed excitation is helpful to avoid Auger process that competes with stimulated emission [1,24]. Therefore, the threshold condition for the lasing phenomena can be obtained without charging or even destroying the QDs.

Microcavities pumped with 10 ns laser pulses at 532 nm (with a repetition rate of 70 Hz) show a well defined onset of lasing (Fig. 3.11 (a)). A linear fit to the integrated intensity of a single lasing modes shows a threshold pump energy of $0.33\,\mu$J/pulse for a $47\,\mu m$ diameter microdisk (Fig. 3.11 (b)). This threshold value is comparable to the one reported for CdSe/ZnS (core/shell) QDs in microdrop cavities $(0.4\,\mu$J/pulse) [21] . It was previously reported that by reducing the concentration of the emitters on the surface of the cavity a reduction in the threshold energy is observed (up to 9.9 fJ/pulse for CdSe/ZnS QDs coated on the surface of a toroidal microcavity [1]). As the result of the lower quantum yield of the bare core CdTe QDs and the enhanced Auger effect associated with its size, a further reduction in the concentration does not yield lasing from CdTe QD/polymer sandwich cavity structures. But a reduction in the lasing threshold can be possibly obtained using tapered fiber excitation due to the efficient pumping of the active gain region of the microdisk cavity as compared to free-space excitation.

As it is shown in Fig. 3.12 (a), the lasing modes are clearly pronounced even for higher pump energy, and also the lasing peaks show no blue shift for increasing pump energies. The photo-bleaching effect is observed for pump energies higher
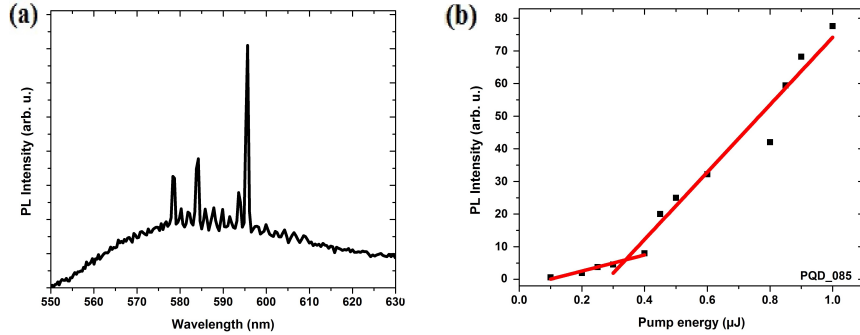
Figure 3.11: (a) Lasing spectrum of CdTe QDs/PMMA sandwich microresonator of a diameter of $47\,\mu m$ at pump energy of $0.5\,\mu J$/pulse, above the lasing threshold. (b) A linear fit to the integrated intensity of one lasing-mode indicates lasing with a small threshold energy of about $0.33\,\mu J$/pulse.
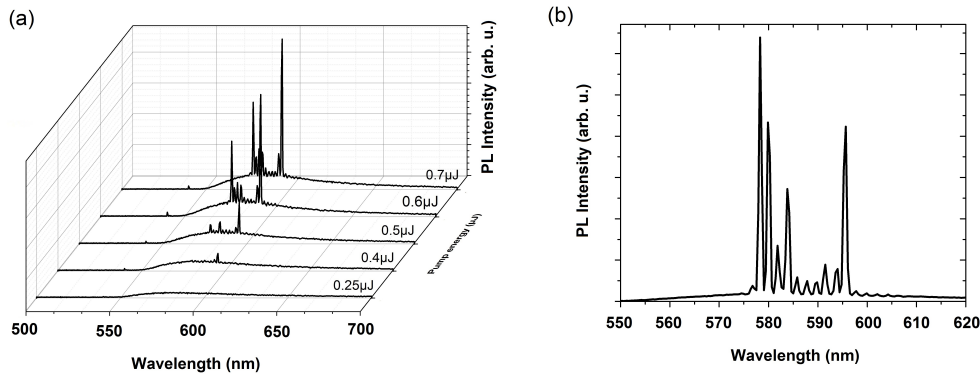
Figure 3.12: (a) The lasing peaks show a stable emission without bleaching and blue shifting of the modes. The smaller peak observed near 532 nm is scattered light from the pump pulse. (b) Lasing spectrum recorded at pump energy of $0.9\,\mu J$/pulse.

than $2\,\mu J$, which is far more than the threshold energy necessary for lasing.

3.3.2 Core/shell/PMMA hybrid particle doped microlasers

Core/shell/PMMA hybrid particles

In order to enhance the quantum efficiency of colloidal QDs (e.g.CdSe nanocrystals), capping their surface using an inorganic material with a wider band gap (e.g ZnS, CdS) semiconductor is indispensable [100]. Even if the capping plays a significant role in the efficiency of the fluorescent emission, the QDs are still sensitive

47
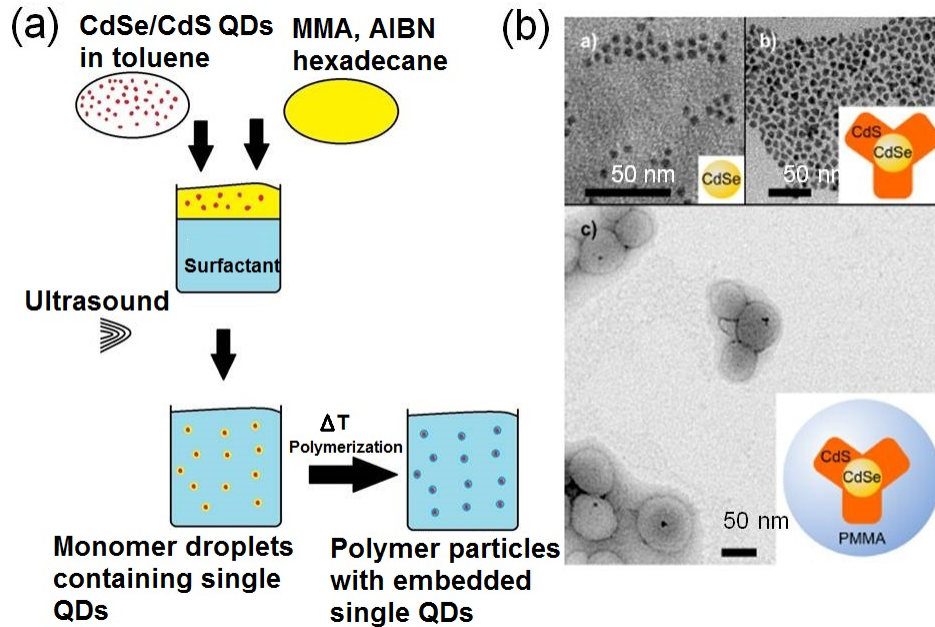
Figure 3.13: (a) Mini-emulsion polymerization process (modified from [99]). (b) Transmission electron microscopy (TEM) image of (a) CdSe core QDs, (b) CdSe/CdS core/shell QDs and (c) CdSe/CdS/PMMA hybrid particles [99].

towards their environment (show photochemical bleaching) and to mechanical damage upon manipulation [101–103]. In addition to the agglomeration of the quantum dots, doping the QDs solution into polymeric matrix is quite difficult due to phase separation the emitters from the host matrix. Encapsulation of core/shell QDs by polymeric nanoparticles leads to a high quantum efficiency, photostability and compatibility with the matrix. Particularly to further improve the optical properties of the QDs (in the PMMA-based polymeric cavities) inorganic/organic polymer-hybrid CdSe/CdS/PMMA QDs are used. These quantum emitters are colloidal CdSe/CdS QDs embedded into methyl methacrylat (MMA) polymer particles via mini-emulsion polymerization [99,104]. In a simple picture the fabrication procedure of this hybrid particles are depicted in Fig. 3.13. More on the chemistry and also the appropriate procedure for the preparation of the emitters are obtained in ref. [99,104]. In the first step 0.1 ml of hexadecane, 10 mg of azobisisobuthyronittrile (AIBN), and 0.2 ml of CdSe/CdS QDs dispersed in toluene were dissolved in 1 ml of methyl methacrylate to form an oil phase. For the mini-emulsification 20 mg of sodium dodecyl sulfate (SDS) was dissolved in degassed water and the oil phase is injected and ultrasonicated (Bandelin GM3200 ultrasonotrode with KE76 tip, operated at 120 W) for 2 minutes. Ultrasonication leads to the creation of mini-emulsion. In this stage surface ligands lead to a centered incorporation of QDs into monomer droplets. Heating

Figure 3.14: (a) Emission spectra of a CdSe/CdS/PMMA hybrid particle doped microcavity laser. (b) A linear fit to the integrated intensity of the lasing mode of hybrid particle doped microresonator shows a threshold energy of 0.36 μJ/pulse.
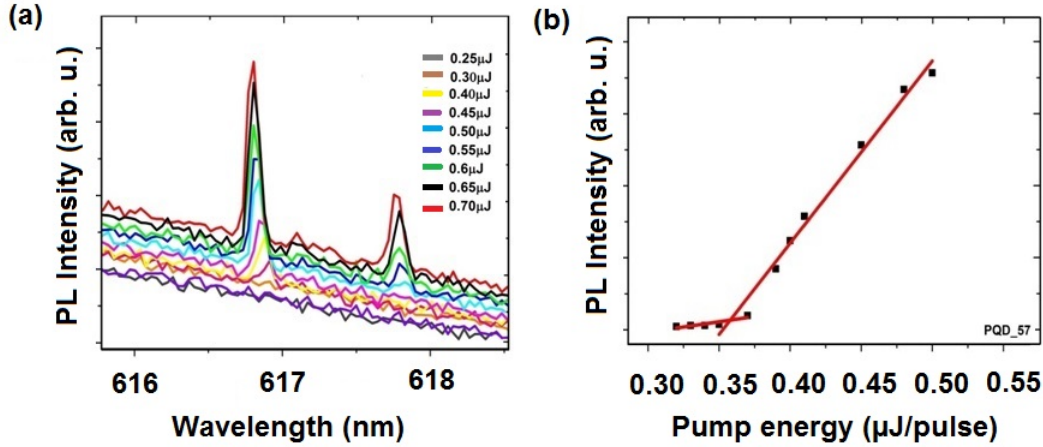
and stirring at 76 °C for 5 hrs under argon lead to polymerization of the monomer droplets. Polymerization of MMA in the presence of quantum dots mini-emulsified in toluene droplets leads to dispersions of PMMA particles with embedded quantum dots. Hence the CdSe/CdS/PMMA particles are produced. The fabrication techniques prevents special red shift caused by Forster energy transfer and also undesired aggregation of quantum dots during the polymerization process [99, 104].

Hybrid particle doped microlasers

The polymer used for the fabrication of the resonators is PMMA, the same material is used in the mini-emulsion polymerization process discussed above for encapsulating core/shell CdSe/CdS QDs. Besides the polymer preventing the emitters from photo-oxidation and increasing its photostability, the compatibility between the polymer matrix and the encapsulated emitter opens a room for doping the QDs into the host matrix before processing the cavities. To do so 15 μmol of these hybrid QDs particles are doped into 1 gram of solid PMMA (in anisole)(15 μmol/1 g solid PMMA). Then about 1 μm thick QD-doped PMMA layer is spin coated on a silicon wafer and the resonator structures are patterned using e-beam lithography as discussed in chapter 2. After developing and etching the sample, CdSe/CdS/PMMA doped microdisk and microgoblet (after heat reflow process) laser resonators are realized on a silicon chip. For the optical characterization the 25 μm radius QDs-doped microresonators are pumped with 10 ns pulses from a frequency-doubled Nd:YVO_4
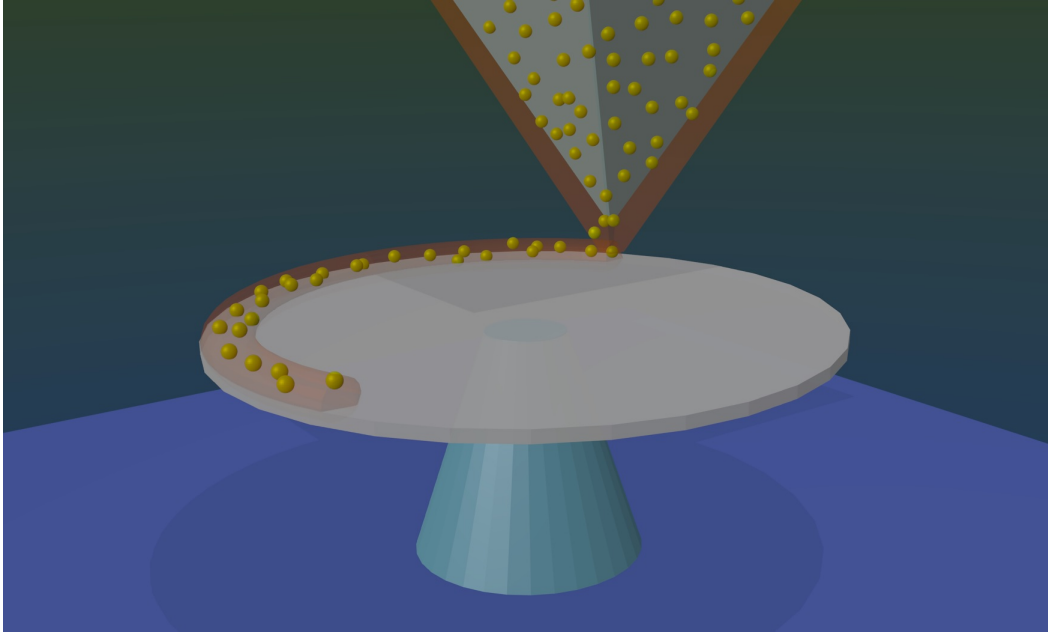
Figure 3.15: The ink which consits of CdSe/ZnS QDs is transfered from the tip (probe) of the AFM to the rim of microdisk resonator via water meniscus formed between the two surfaces.

laser at a pump wavelength of 532 nm (with a repetition rate of 90 Hz) in a free-space excitation as shown in Fig. 3.8. As it is depicted in Fig. 3.14 pumping for different pulse energy leads to low-threshold quantum dot lasing (with the threshold energy of 0.36 μJ/pulse). The output intensity for certain pump energies is determined by integrating the intensity of a single lasing mode. The onset of lasing is inferred from the super-linear increase of the intensity resulting from the dominance of stimulated emission over spontaneous emission as shown in Fig. 3.14 (b).

3.3.3 Highly localized quantum dot deposition using dip-pen nanolithography

Even if WGMs are confined on the rim of the resonators, polymer/QD sandwiched structures and core/shell/PMMA hybrid particle doped resonators have the gain medium throughout the whole cavity. This leads to high absorption of the pump photons (result in huge spontaneous emission which do not contribute for lasing and increases the threshold energy). The most straight forward way to efficiently couple the QDs into polymeric high Q-cavities is highly localized deposition of the emitters
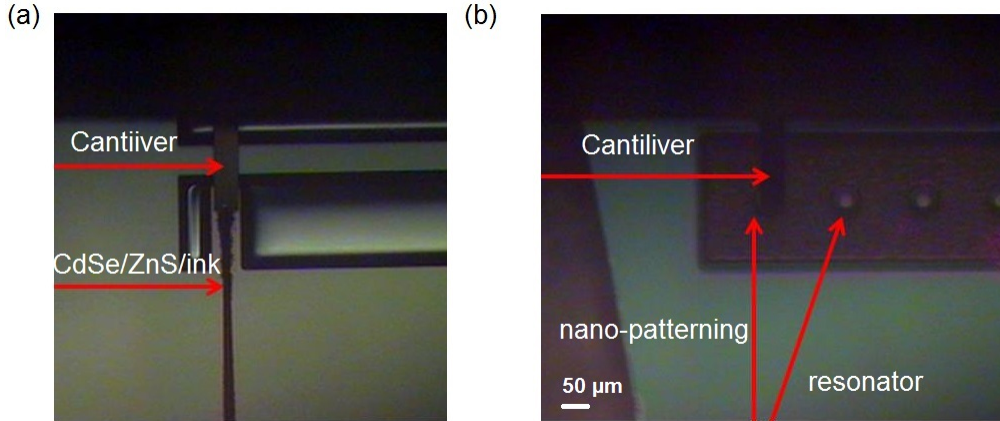
Figure 3.16: (a) The DPN probe is dipped into the reservoir and the QD/ink is transferred to the surface of the tip at high relative humidity condition (70%). (b) QDs nanopatterning on the rim of the resonator. The deposition of the ink is controlled by the speed of the probe and the changes of the relative humidity during lithography.

solely on the rim of the circular symmetrical boundary of the resonator. This is not easy due to the difficulty of patterning of the emitters in few nanometer scales.

One way for constructive functionalization with high spatial resolution and accuracy is dip-pen nanolithography (DPN) [105] . This technique utilizes the tip of an atomic force microscope (AFM) coated with desired chemical inks to pattern surfaces (from nano-micro scale). To facilitate the transfer of QDs in DPN, it is useful to employ some kind of carrier ink. The carrier or matrix should be neutral to the desired application and compatible with the materials to be carried. Often used carriers in these matrix-assisted DPN (MA-DPN) and related techniques as matrix-assisted polymer pen lithography (MA-PPL) are polyethylene glycol (PEG) [106, 107] and glycerol [108] in case of water compatible materials. Also phospholipids or cholesterol can act as carrier: DPN with lipids (L-DPN) is usually performed for the generation of artificial biomimetic lipid membranes [109] in the context of biological experiments [110, 111] and also for sensor applications [112–114].

In the following QDs-lasers via highly localized deposition of CdSe/ZnS QDs on the very rim of PMMA microdisk resonators using MA-DPN is realized. The patterning is in few nanometer scale and enables lasing only in the lower order cavity modes (which have higher modal gain as compared to higher order cavity modes).

The "ink", which mainly consists of QD nanoparticles in cholesterol matrix is prepared in a special technique and it helps the transfer of the QD particles from the tip
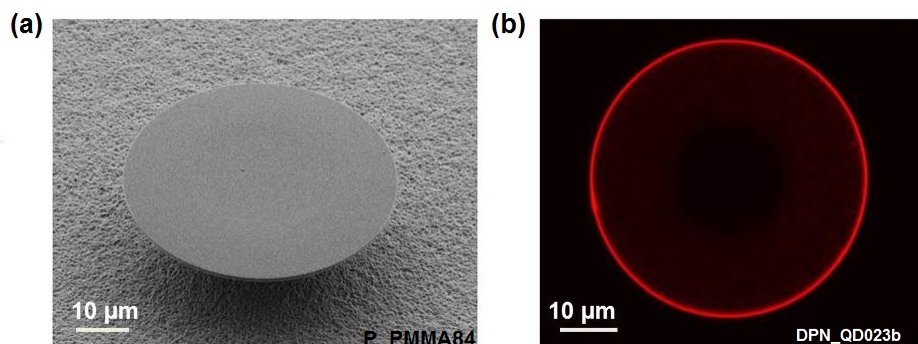
Figure 3.17: (a) Scanning electron micrograph image of PMMA microdisk resonator. (b) Dark-field (DF) microscopy image of highly localized deposition of CdSe/ZnS core/shell quantum dots on the rim of a 49 μm diameter microdisk resonator using DPN technique. For the DF-image the sample is excited by Mercury lamp (415-455 nm) and the pump light is filtered by DC-mirror of transmission on the QD emission wavelength (>550 nm).

to the sample surface through a water meniscus that automatically forms between tip and surface at humid environment as depicted in Fig. 3.15. The preparation of the ink, the patterning condition and optical characterization of highly localized deposition of QDs on the rim of the resonator is discussed below[3].

Preparation of QDs/ink

The QDs used in the experiments are CdSe/ZnS structures (PlasmaChem, Berlin). The QDs have an average size of 2.45 nm radius and their size is much smaller than the excitonic Bohr radius of CdSe/ZnS $\sim$ 6 nm. Hence the QDs are in the strongly confined regime. For the preparation of the ink, QDs are dissolved in toluene with a concentration of 5 mg/ml in ultrasonic bath. Similarly 5 mg/ml of cholesterol (Avanti (ovine wool>98%)) in chloroform is also prepared. The role attributed to the cholesterol is to serve as a QD carrier during the nanopatterning steps. The QD-ink solution is prepared by admixing $4 \mu l$ cholesterol in chloroform solution into 30 μl of CdSe/ZnS in toluene. After mixing of these components together, the QD-ink solution was sonicated in ultrasonic bath for 30 minutes. Then 1-2 μl of QD/ink is filled into a reservoir of an inkwell (M-6MW, NanoInk, INC., Skokie, IL, USA). To evaporate the solvents the inkwell is placed in evaporation desiccator for 30 min.

---

[3]The results presented in this section will be submitted for publication, the manuscript is under preparation (2014).
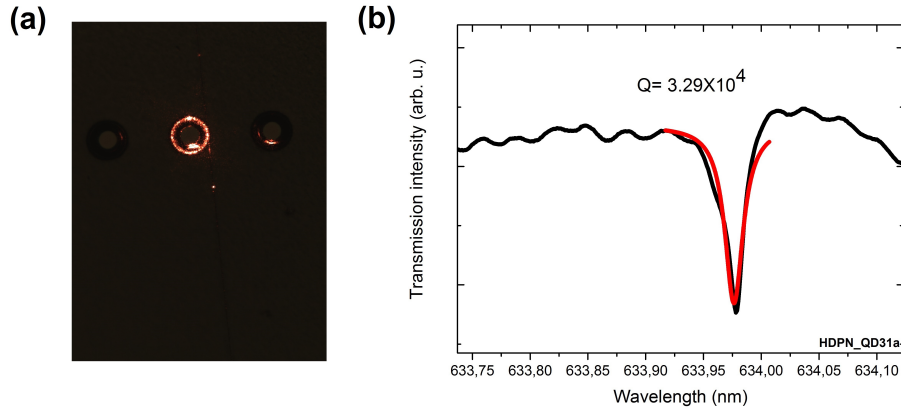
Figure 3.18: (a) Light is evanescently coupled into the resonators via tapered fiber. (b) The transmission spectrum from a tapered fiber coupled to nanopatterned resonator shows WGM resonances and the Lorentzian-fit to the modes reveal high-Q factors reaching 3.14×10^4.

Nanopatterning

A commercial DPN instrument (DPN 5000, NanoInk, Inc.) equipped with a camera with a single tip pen (type A, NanoInk, Inc.) is used for nanopatterning. To prevent mechanical damage while patterning, flexible probes with very low force constant $(0.04 \ N/m^2)$ are used.

The pen was coated with QD-ink by dipping into the microfluidic channel of the inkwell for 30 min at 70% relative humidity and 23 °C as shown in Fig. 3.16(a). The QD-ink solution is transferred from the reservoir to the tip (probe) through a water meniscus that forms between the two surfaces.

After dipping the pen and the probe can be immediately used for nanopatterning. The QDs are solely deposited on the rim of the resonator by bringing the probe on the top-rim of the microdisk resonator. The cavity has a radius of about $24.5 \, \mu m$ and the lithography step is designed so that the probe coats only the rim of the resonator (probe patterning radius 24-24.5 μm) as depicted in Fig. 3.16(b).

The concentration of the QDs deposited on the cavity is determined by the speed of the tip (in the experiment the speed of the probe is varied between 1-5 μm/s), the deposition rate of the QDs in the ink and also the size of water meniscus formed between the tip of the probe and the cavity surface (at 70 % relative humidity).
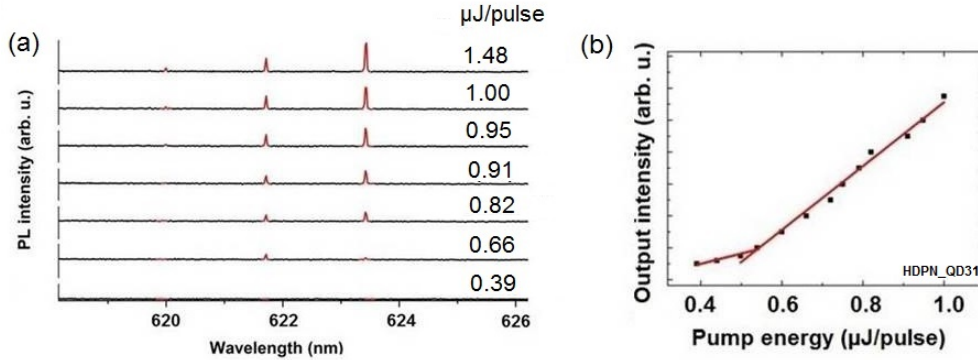
Figure 3.19: (a) Lasing spectrum of a dip-pen nanolithographically patterned microlaser for different pump energies. (b) A linear fit to the integrated lasing peaks revels low threshold QD-lasing with a threshold energy of 0.56 μJ/pulse.

Fig. 3.17 (a) and (b) show scanning electron micrograph image of microdisk resonator and fluorescence microscopy image of highly localized deposition of CdSe/ZnS quantum dots on the rim of 49 μm diameter resonator (the speed of the coating probe is 5 $\mu m/s$). It is found that the lateral side extension of QDs/ink after deposition ranges about $0.6 \pm 0.1 \, \mu m$ from the very rim of the resonator.

Optical characterization

For the optical characterization of QDs-coated resonators, light is evanescently coupled into the resonators via tapered fiber as discussed in chapter 2. Due to the sticky nature of the QD/ink on the rim of the resonator, the fiber is attracted to the resonator during coupling. To prevent the fiber from breaking and also reduce the loss mechanism due to the coupling process, the translational stage is made to have a resolution of about 20 nm. The resonator-tapered fiber distance is adjusted until the WGMs are appeared as sharp dips in the transmission spectrum as shown in Fig. 3.18 (b). Also on the camera the coupling is observed when the light is circulating around the rim of the resonator as depicted in Fig. 3.18 (a). The modal spectrum observed from the transmission coupled fiber shows complex WGMs, with a Q-factor reaching 3.14×10^4 near 634 nm (see Fig. 3.18 (b)). Even if the QDs are absorbers and scatters, the high localized deposition technique still maintains high-Q factor of the microdisk resonator. Hence the feedback from the cavity is good enough to support lasing for the appropriate optical gain conditions.
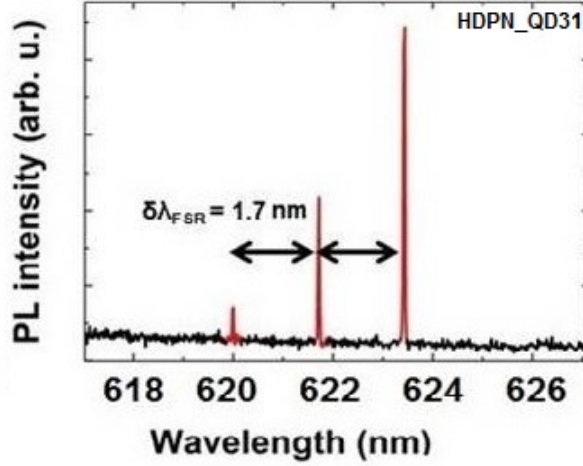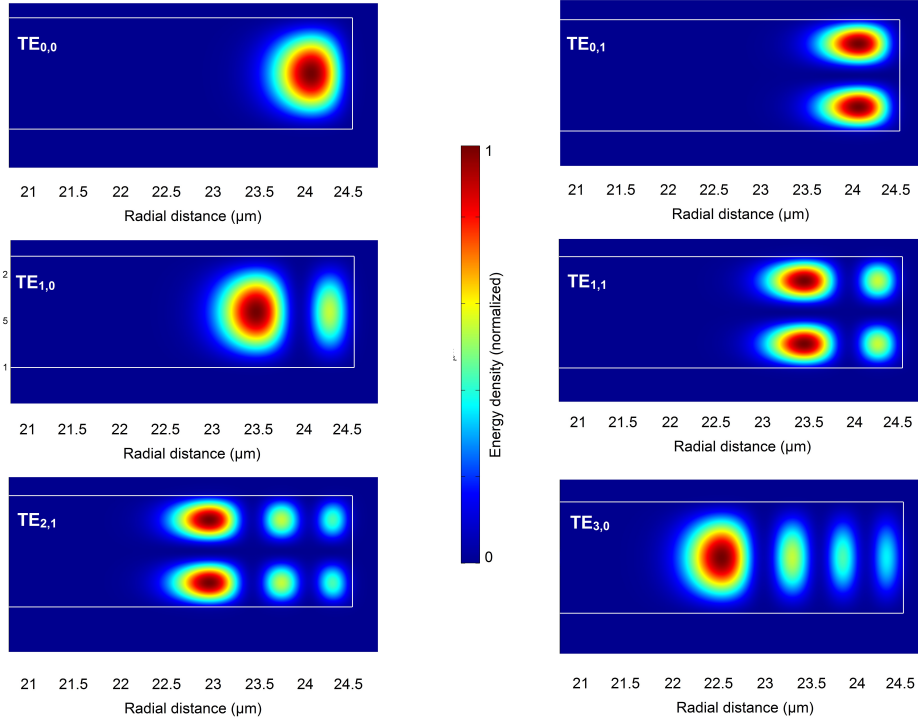
Figure 3.20: Lasing in the fundamental mode of the cavity. The spacing between the lasing modes is about 1.7 nm which is in the same magnitude as the free spectral range ($\delta\lambda_{FSR}$) of the microresonator (theoretically it is about $\delta\lambda_{FSR}$= 1.67 nm).

Free-space excitation

For optical excitation of $49\,\mu m$ radius dip-pen nanolithographically patterned microresonators, free-space excitation in a micro-photoluminescent setup is used. Again 10 ns pulses from a frequency doubled Nd:YVO$_4$ laser at a pump wavelength of 532 nm (with a repetition rate of 90Hz) is used as a pump source. As it is depicted in Fig. 3.19 (a) pumping for different pulse energy leads to low threshold quantum dot lasing. The linear fit to the integrated lasing peaks revels low threshold QD-lasing with a threshold energy of 0.56 μJ/pulse, as shown in Fig. 3.19(b).

As it is observed from the lasing spectra there is a mode spacing of about 1.7 nm between the lasing peaks (see Fig. 3.20). This is in the same magnitude as the free spectral range ($\delta\lambda_{FSR}$) of the PMMA based microresonator (theoretically it is about $\delta\lambda_{FSR}$= 1.67 nm near 625 nm wavelength range for a diameter of 49 μm PMMA microdisk resonator). This shows that the lasing phenomena is most likely occurs in the low order fundamental cavity modes as they provide highest modal gain as compared to higher order cavity modes. This argument is supported by the simulation of the mode profile of a microdisk resonator.

For the realization and understanding of the mode structures and the spatial distribution of the WGMs in PMMA microdisk resonators, finite element (FEM) simulations were performed as discussed in chapter 2.

Figure 3.21: Electric energy density distribution in microdisk resonator of 24.5 μm radius and 1.2 μm thickness. The fundamental modes of both polarization (TE and TM) are confined on the rim of the resonator and the higher order modes are far away from the rim depending of the quantum numbers. The electric energy density distribution and resonance wavelength of the WGMs were calculated with JCMResonance. The azimuthal mode number of the presented WGMs is m = 384.

Fig. 3.21 shows the intensity distribution of energy density of the fundamental and higher order modes of microdisk resonator and the radial distance of the localization of the modes. The low order transverse electric field modes TE$_{00}$ and TE$_{01}$ are located on the rim of the resonator and its energy density extends up to $0.7\mu m$ from the rim of the resonator. This is exactly in the same position where the QDs are deposited. As the mode numbers increases, the maximum of intensity moves towards the center of the resonator where there is no active media. This argument proves the lasing obtained from high localized deposition is mainly from low order fundamental modes of the cavity. TE and TM modes of similar radial and angular quantum numbers show slight resonance wavelength difference but the energy density distribution is similar.

3.4   Summary and Conclusions

In this chapter, the use of nanocrystal colloidal QDs as a gain medium was discussed. The loss and the gain mechanisms for developing optical gain and lasing was presented.

In order to integrate QDs in polymeric resonators three important techniques were shown. In the sandwiched resonator structure CdTe QDs embedded between PMMA layers enabled the coupling of the QDs to the eigenmodes of the WGM resonator. In order to dope QDs into the polymer host matrix, CdSe/CdS/PMMA hybrid particles (fabricated via mini-emulsion process) were used. For the highly localized deposition of the emitters only on the rim of the resonators, dip-pen nanolithography technique was utilized. These highly localized deposition enabled lasing only on the lower order fundamental modes of the cavity. All the three routes for the integration of colloidal QDs into polymeric resonators showed low threshold microlasing, with a threshold energy in few μJ/pulse.

Chapter 4

Organic Dye Doped Low-Threshold Microlasers

As it is discussed in the previous chapter simple integration of QDs as a gain medium in microcavities is challenging due to the phase separation of the emitters from the polymer host matrix. So the QDs need special pre-treatment to be incorporated into the microcavities. In the following chapter an organic laser dye with near unity fluorescence quantum yield, low self-aggregate and perfect compatibility with the host matrix is introduced. The chapter begins with an overview of the photophysics of organic dyes (π-conjugated organic molecules) as well as a theoretical framework for the description of dye lasers in most practical situations. The absorption and emission mechanisms and the development of optical gain relevant for lasing performance are discussed. For the realization of polymeric dye lasers, Pyrromethene 597-doped microcavities are used. The fabrication process and its optical characterization are presented as well.

4.1 Basics of π-Conjugated Molecular Systems

Organic compounds usually consist of carbon and hydrogen along with a few possible hetero-atoms (e.g. oxygen, nitrogen or sulfur). Carbon atoms have six electrons with a configuration of $1s^2 2s^2 2p^2$. Hence the s orbitals are fully occupied but two out of the three p_x, p_y and p_z orbitals are occupied by one electron each. When a carbon atom binds with another atom, hybridization between s and p orbitals occurs. When the C atom binds via four single bonds to other atoms, sp^3-hybridization occurs and the outer four electrons are arranged at the corners of a tetrahedron to form σ-bonds, which exhibit a cylindrical symmetry. These saturated compounds

lead to good electrical insulation. Examples are alkanes or saturated polymers such as polyethylene (-CH2-CH2-)n, polystyrene (-CH2-CH(Ph)-)n or polypropylene (-CH2-CH(CH3)-)n [115]. Unlike saturated molecules, organic compounds containing double or triple bonds have more complex and interesting properties. These compounds, like ethylene (CH2=CH2) for example, have double bond and its carbon atoms exhibit sp^2-hybridization as shown Fig. 4.1. The three sp^2-hybrid orbitals form a trigonal planar geometry, pointing to the three vertex of an equilateral triangle (with an angles of 120 °C between them). The unhybridized $2p_z$ orbitals are perpendicular to this plane and overlap side-by-side to form a weaker π-bond [115].

If the molecule has an alternation of double and single bonds over a planar segment, the system is said to be π-conjugated. Such systems can exist in many forms as small molecules, conjugated polymers or molecular crystals[1]. The simplest examples of π-conjugated molecules, for understanding the physics, are benzene and butadiene (see Fig. 4.2) even though they are not useful for lasing. The overlap between the π-orbitals in the structures allows the de-localization of the electrons over the whole conjugated segment. A naive picture of de-localization of electron is considering the π-electron moving along the conjugated chain as a flip-flop between single and double bonds. The alternation of double and single bonds is a requirement for π-conjugation, but not sufficient condition as the bonds should also lie in the same plane to enable electron de-localization. For instance, benzene, with its 6 carbon atoms linked at the corners of a regular planar hexagon (see Fig. 4.2), is the archetype of aromatic conjugated systems. In contrast, cyclooctatetraene, which is a regular octagon with alternating simple and double bonds, adopts a nonplanar conformation and is therefore not aromatic (and only weakly conjugated) [115].

When more and more p_z orbitals are shared to form a conjugated system, the energy between molecular orbitals decreases, exactly like the decrease in the energy level gaps while the size of the the box dimensions increase in a 'particle in a box' model of quantum mechanics. The derivation for the energy levels, optical gap and its consequence for the absorption property of the dye is discussed below.

---

[1]Most dyes have a portion of the molecule which is conjugated and is called the active unit (or chromophore unit). The rest of the molecule can be a saturated alkyl chain (added for solubilization) or bulky side groups (added to prevent stacking of the π-orbitals between them in adjacent molecules, like in dendrimers [116]) or in small molecules with bulky side substituents [117].
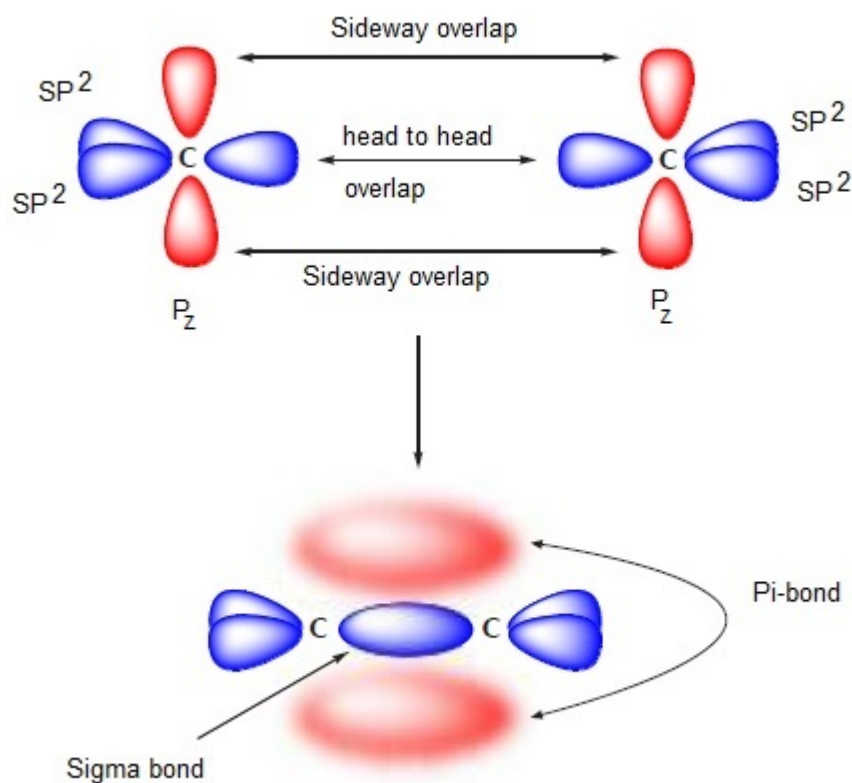
Figure 4.1: Illustration of σ- and π- orbitals in ethylene (modified from [118]).

4.1.1   Energy eigen states

In the free electron model the de-localized π-electrons are considered as freely moving within their planar distributions above and below the molecular plane. Their movement is only restricted due to the repulsive potential of the methyl groups at the end of the chain of the dye. The electrostatic potential of a single π-electron moving in the molecular field of the molecule is considered to be constant. Then the electronic states of a dye molecule can be approximated by the analogy of freely moving electrons in a potential well, shown in Fig. 4.3 for a cyanine dye. Considering the length L of the conjugated chain, the energy of the nth eigenstate of electrons can be defined as:

$$E_n = \frac{h^2 n^2}{8mL^2} \qquad (4.1)$$
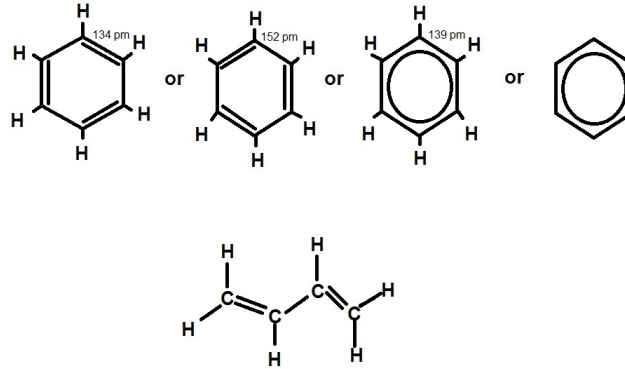
Figure 4.2: Two simple and archetypical examples of π-conjugated systems: benzene (top) and 1,3-butadiene (bottom) [115].

where m is the mass of the electron and n is the quantum number describing the antinodes of the eigenfunction along the chain. When light is incident upon a conjugated molecule, an optical transition can occur. The lowest energy required for such optical transitions defines the optical gap. The optical gap is slightly lower than the gap between the highest occupied molecular orbital (HOMO) and lowest unoccupied molecular orbital (LUMO), this is due to the attractive interaction between a hole (the abscence of electrons in HOMO) and an electron (electron in LUMO) which coexist in a single molecule to form the excited state. This is the same as the exciton binding energy. By neglecting this binding energy (as it is comparatively small), the optical gap can be derived as follows: Due to Pauli exclusion principle each of the energy states can be occupied by two electrons of opposite spin hence the molecule is in the singlet state S_0. For a dye in the ground state with $2N$ electrons, the lowest N states are filled. The smallest energy needed to excite the molecule is the energy difference between the highest occupied state E_N and the lowest unoccupied energy state E_{N+1}. Using equation 4.1, this energy can be calculated as:

$$E_{gap} = E_{n=N+1} - E_{n=N} = \frac{h^2}{8mL^2}(2N+1) \qquad (4.2)$$

This minimal energy defines the longest wavelength that can be absorbed by the molecule through the relation:

$$\lambda_{max} = \frac{hc}{E_{gap}} = \frac{8mcL^2}{h(2N+1)} \qquad (4.3)$$

This expression indicates that the position of the absorption band is determined by the chain length L and the number of π-electrons. Usually lots of p_z orbitals are shared to form the conjugated system and the absorption band (which depend on
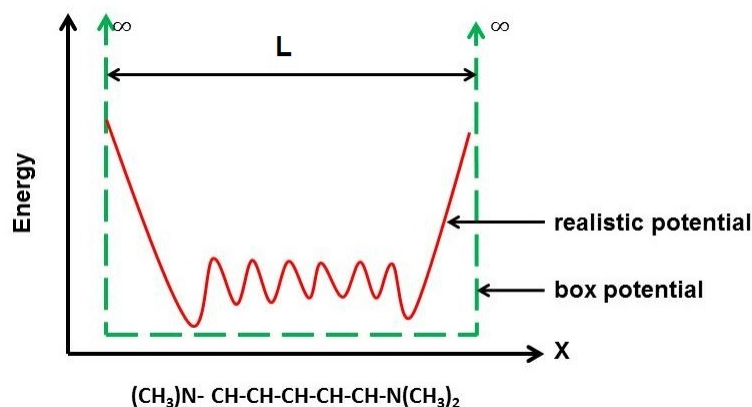
Figure 4.3: The realistic and box potential energy of a π-electron moving along the carbon chain of cyanine. In the particle in a box model the energy states of π-electrons are considered as freely moving electrons in a potential well of length L (green dashed line), which is the length of the carbon chain. The realistic potential is depicted by the red line [119].

L) typically occurs at wavelengths above 200 nm, making such compounds suitable for optical excitation in the UV- visible part of the spectrum [115].

4.1.2   Photophysical properties of π-conjugated systems

Optical transitions associated with molecules with only single bonds are of the type $\sigma - \sigma^*$ and lead to absorption bands at wavelengths below 160 nm. The associated photon energy ($\backsim$ 7 eV) is higher than the dissociation energy of the chemical bonds (photochemical decomposition is likely to occur), hence such compounds are not suitable as a gain medium for lasing [115]. Suitable optical transitions for lasing performance are based on $\pi - \pi^*$ transitions.

Electrons have spin angular momentum, described by a spin quantum number s = $\pm 1/2$. The sum of all spins of all electrons involved in a system is defined by the spin S of the system, and spin multiplicity is defined as 2 S + 1. When S = 0 the state is said to be a singlet state whereas when S = 1, the multiplicity is 3 and the state is said to be a triplet state. Excited states in organic materials are created by the absorption of a photon, that is promoting one of the two electrons of the ground state to one empty higher-lying orbital. As inner, filled, energy states are not involved in optical processes, the ground state of the system is usually described by a single filled orbital (the HOMO) containing two electrons, whose spins are necessarily antiparallel due to Pauli exclusion principle. Hence the ground state of an
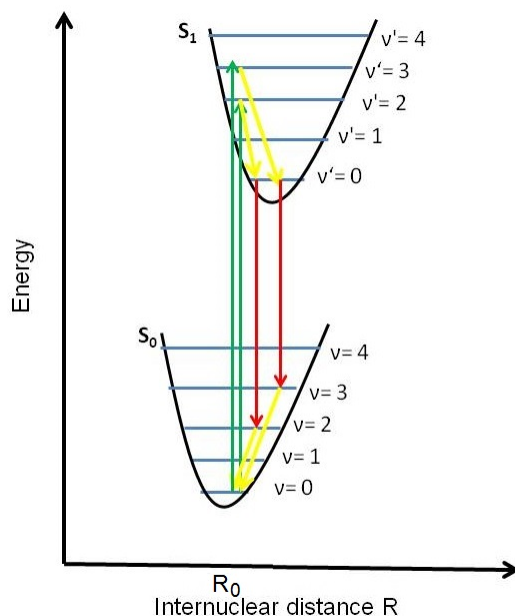
Figure 4.4: Potential energies of the S_0 and S_1 state of a molecule as function of the internuclear distance. The vibrational energy levels are denoted as ν and ν' [121]. The transitions given by the Franck-Condon principle are indicated as vertical arrows, where the absorption of a photon is marked in green and the emission is marked in red. Nonradiative vibrational state assisted transitions are represented in yellow.

organic system is always a singlet state, denoted by S_0. Excited states are described by two electrons: one residing in the HOMO level and the other one in another antibonding molecular orbital, which can be the LUMO or any another higher-lying antibonding orbital. Since the two electrons are not any more in the same electronic level, Pauli exclusion principle does not hold and there is a possibility of other spin combinations. The singlet and triplet excited states are denoted by S_1, S_2, S_3,...., S_n and T_1, T_2, T_3,...., T_n respectively. Even if there is no limitations due to Pauli exclusion principle, not all optical transitions are possible due to optical selection rules [120]. Spin selection rule dictates that for a pure electric dipole transition, the electric field of the incoming radiation can not switch the spin of an electron. Therefore absorption from the ground singlet state S_0 can only lead to excited singlet states S_1,...., S_n. However the creation of triplet state is not totally forbidden and can be enhanced through spin-orbit coupling. The formation of triplet states and the accompanied transitions will be discussed later.

The electrons in a molecule move much faster than the nuclei (because of their

lower mass) so that an electronic transition occurs without changes of the nuclei positions [122]. This well known phenomena is called the Franck-Condon principle[2]. The transitions between S_0 and S_1 are represented by vertical lines in diagrams in which the potential energy of the electronic molecular state (approximated as Morse potential) is plotted as function of the nuclei distance (Fig. 4.4). The horizontal equidistant lines (nearly the same due to the approximated quadratic potential in this region) represent the vibrational states. A transition is more likely occur for overlapping wavefunctions of the vibrational states of the initial and final state and can be evaluated using quantum mechanics by considering the overlap integral of these wavefunctions. After excitation into higher energy levels (S_1 or higher) in femtosecond time scale, the molecule relax into $S_{1,\nu'=0}$ level within picoseconds. From lowest energy level $S_{1,\nu'=0}$ again relaxes into $S_{0,\nu\neq0}$ within nanoseconds accompanied by spontaneous emission of a photon and following non-radiative relaxation into the $S_{0,\nu=0}$ state.

Fast non-radiative relaxation process of singlet states as compared to slower radiative transitions can lead to an efficient build up of inverted population, resulting from accumulation of dye molecules in $S_{1,\nu'=0}$ level. It is important to note that the energy difference between vibrational levels is around $125\,\mathrm{meV}$, which is considerably higher than $k_B T \approx 25\,\mathrm{meV}$ at room temperature. Therefore the higher vibronic levels of the singlet ground state are not occupied at room temperature.

Due to the large number of atoms in a dye molecule, there is a large number of vibrational states involved during absorption. This leads to broad absorption spectra. Fig. 4.5 shows singlet-state absorption and emission cross-section of Rhodamine 6G and Pyrromethene 597 dye.

In addition to the optical transitions involving the singlet state with $S = 0$, spin-orbit coupling can lead to non-radiative transitions between singlet and triplet states through a process called intersystem crossing (ISC) (see Fig. 4.6). ISC has a large time constant around $100\,ns$ which is much larger than the radiative spontaneous emission lifetime (few nanoseconds). This very small radiative life time of organic dyes is due to the very large dipole matrix element ($\backsim eL$) originating from the large spatial de-localization of π-electrons. The π- electron distribution also plays a major role for ISC formation. It was discovered that for π-electrons of the chromophore

---

[2]The Franck-Condon principle is a classical approximation of an electronic transition. It states that the likelihood of the occurrence of electronic transition without changes in the positions of the nuclei in the molecular entity and its environment. The resulting state is called a Franck-Condon state. The quantum mechanical formulation of this principle is that the intensity of a vibronic transition is proportional to the square of the overlap integral between the vibrational wave functions of the two states that are involved in the transition.
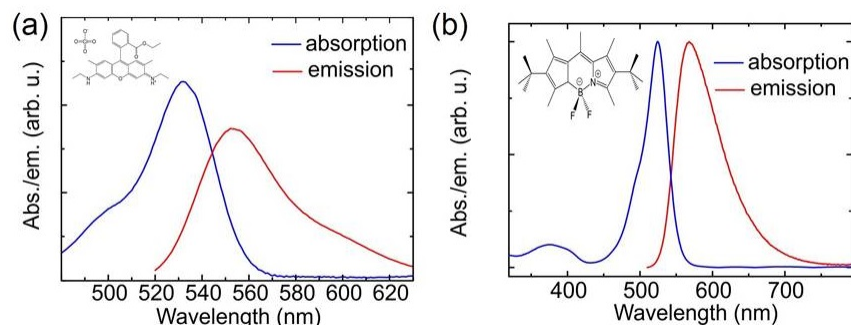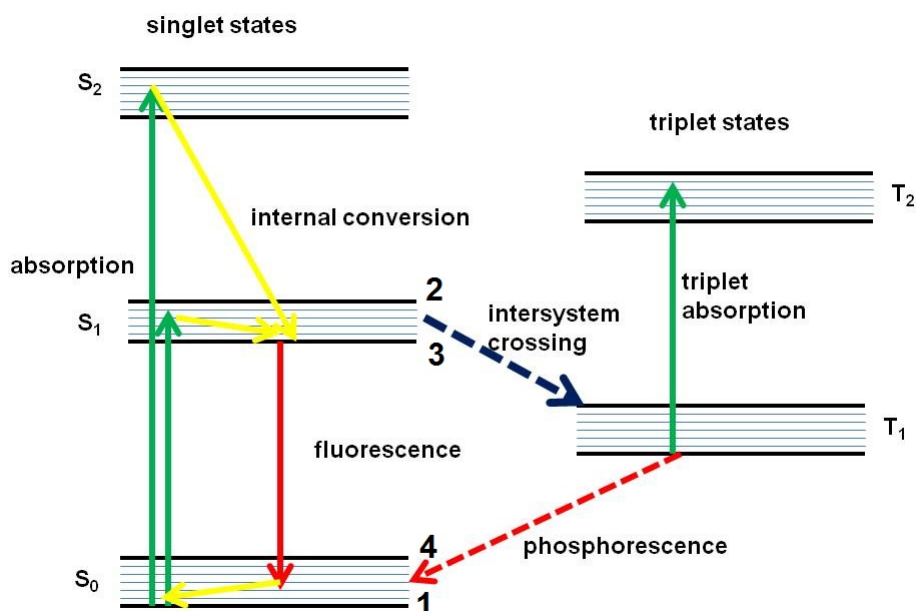
Figure 4.5: Absorption and emission spectra of Rhodamine 6G (a) and Pyrromethene 597 (b) dye [19].

makeing a loop, the triplet yield is higher than for the case in which the loop is blocked [119]. This can be explained by an increases in the spin-orbit coupling due to an increase in orbital magnetic moment caused by orbiting electrons [119]. The forbidden spin-flip transition to the ground state leads to a long life time of the triplet states reaching up to $100\,\mu s$ [121]. The radiative transition from T_1 to S_0 is known as phosphorescence.

4.2   Relevant Conditions for Lasing

4.2.1   A 4-level system

Vibrationally broadened energy states and the accompanied Stokes shift makes organic dye at first approximation as a 4-level system as shown in Fig. 4.6. The fast intraband decay in sub-pico seconds explains why the fluorescence spectrum does not depend on which sublevel (within the S_1 manifold) the molecule has been excited. Excitation in a higher level S_n ($n > 1$) also leads to the same emission spectrum, as internal conversion from S_n to S_1 also occurs on a picosecond scale through non-radiative processes. Pumping to S_n state ($n > 1$) leads to thermal dissipation through non-radiative channels, and is consequently determinantal to the laser efficiency. The lowest vibrational level of S_1 has a relatively long lifetime, typically in the order of a few nanoseconds. The lasing transition then occurs between this level and one of the R_0-vibrational levels of the S_0 manifold and another sub-picoseconds fast non-radiative decay brings the molecule back to the ground state, i.e. the lower-lying level of S_0.

Figure 4.6: Energy diagram and optical transitions involved in dye molecules. Solid arrows represent spin-allowed transitions and broken arrow indicates spin-forbidden transitions. Optical absorption and emission are represented by green and red arrow respectively. Internal conversion marked by yellow. The intersystem crossing (singlet to triplet transition) is represented in blue/black.

For laser applications, a large Stokes shift is indispensable as it reduces the amount of ground state re-absorption of laser light. But a huge Stokes shift is not ideal as it enhances the thermal loading and sends the molecule in a highly-excited vibrational state which leads to photo-dissociation [115]. The extent of the Stokes shift for a given π-conjugated compound is highly dependent on the environment (host matrix) and particularly on its polarizability: the higher the polarizability of the surrounding, the higher the redshift [123]. This is a well known effect in molecular fluorescence. When a dye molecule with high polarizability is dispersed into a nonpolar host matrix, the emission curve will shift towards longer wavelengths upon increasing the dye concentration. An example of such a behaviour is seen in triarylamines in Alq_3 [124].

4.2.2   Threshold condition for dye lasers

In this subsection the photophysical parameters and their time constants relevant for organic dye lasing is presented.

Fluorescence

Molecules can decay radiatively through fluorescence. The radiative decay is defined by $\kappa_r = \tau_{rad}^{-1}$, where τ_{rad} is the radiative life time. This is related to the absorption of the $S_0 \rightarrow S_1$ band through the Einstein relations. Unlike in an atomic system a modified picture is required to take into account the broad absorption and emission characteristics. The relation connecting the radiative life time to the absorption cross-section spectrum is derived in the work of Strickler and Berg [125] and is given by [126]:

$$\kappa_r = \frac{1}{\tau_{rad}} = \frac{8\pi c n_F^3}{n_A} \frac{\int_{S_0 \rightarrow S_1(em)} f(\lambda) d\lambda}{\int_{S_0 \rightarrow S_1(em)} f(\lambda) \lambda^3 d\lambda} \int_{S_0 \rightarrow S_1(abs)} \frac{\sigma_{abs}(\lambda)}{\lambda} d\lambda \qquad (4.4)$$

where n_A and n_F refers to the average refractive index of the material in the absorption and emission spectral regions, usually $n_A > n_F$. Using the fluorescence spectrum $f(\lambda)$ as a weight function one can write the above expression as:

$$\kappa_r = \frac{8\pi c n_F^3}{n_A \langle \lambda^3 \rangle_F} \int_{S_0 \rightarrow S_1(abs)} \frac{\sigma_{abs}(\lambda)}{\lambda} d\lambda \qquad (4.5)$$

Internal conversion

The non-radiative decay rate of the molecule to the ground state by internal conversion (IC) is defined by $\kappa_{nr} = \tau_{nr}^{-1}$. The IC is usually related to the structural rigidity of the molecule. Non-radiative decays require coupling of vibrational states between the excited and the ground state. Rigid and planar molecular structure follow luminescence than IC, as seen in the highly fluorescein molecules [127]. IC is favoured when a resonance is obtained between a highly vibrational state of S_0 and the lowest lying vibronic state of S_1. For this reason stretching vibrations associated to atoms (e.g. highly energetic vibrations due to the low mass of H-atom) are likely to contribute to non-radiative decay (e.g. the Rhodamine 110 [127]). Hence long-wavelength emitters with a small energy gap (HOMO-LUMO) are likely to suffer the IC. However for organic dyes emitting in the green, blue or UV-most of the quantum yield quenched due to intersystem crossing (ISC) rather than IC [115].

Intersystem crossing

The intersystem crossing (ISC) rate is represented by κ_{ISC}. As it is explained in the previous section this phenomena is basically related to the spin-orbit coupling in the

molecule. A molecule transferred to the triplet state T_1 may relax to the ground state with a rate defined by $\kappa_T = \tau_T^{-1}$, which is mostly non-radiative from $T_1 \rightarrow S_0$ due to the spin-forbidden transition (see Fig. 4.6). There is also a possibility of radiative decay (phosphorescence). Phosphorescence can be observed at low temperature when vibrational excitations are frozen and also for molecules having strong spin-orbit coupling [115].

An emitter in the T_1 state can also make a transition to a higher-lying triplet state T_n by a spin-allowed transition through the process called triplet absorption (TA)(see Fig. 4.6). The typical cross-section of triplet absorption is $\sigma_{TT} \backsim 10^{-16} cm^2$, which is in similar order of magnitude with the stimulated emission cross-section [121]. Hence there is a significant spectral overlap between them. There is also a decay of the emitter in the T_1 state to the ground state in biomolecular process through the encounter with a singlet state (called singlet-triplet annihilation (STA)) or triplet state (called triplet-triplet annihilation (TTA)) [115].

Triplet state formation also leads to irreversible quenching of dyes due to its reaction with oxygen in the environment (photo-oxidation). This effect is more pronounced at higher temperatures due to an increase in the mobility of the dye. During optical pumping the excess energy is dissipated as heat to the surrounding of the dye, hence the active medium is heated. Liquid dye lasers overcome this problem by continuously exchanging the solution in the pump beam [128]. In dye-doped polymers, heat dissipation has to be as efficient as possible to obtain high operational lifetime, hence the dye molecules have to be stably embedded in the polymeric host matrices [18,129], e.g., by covalent linking of dye molecules to the polymer chain [130].

Therefore to develop significant gain and population inversion for lasing the triplet state formation should be reduced significantly. This is possible using pulsed laser sources with pulse widths smaller than the intersystem crossing rate. When the pump light energy density reaches the lasing threshold before the intersystem crossing rate $k_{ISC}^{-1} = 100\,ns$ of dyes, stimulated emission occurs faster than the triplet state formation [119]. Hence pump pulses of few tens can be used to overcome ISC.

Quantum yield

One of the most important parameters of organic emitters is the quantum yield of fluorescence ϕ_F $(0 < \phi_F < 1)$. It is the ratio of emitted fluorescence photons divided by the number of absorbed pump photons. The real definition of this parameter needs the incorporation of quenching mechanisms and is given by:

$$\phi_F = \frac{\kappa_r}{\kappa_r + \kappa_{nr} + \kappa_{ISC}} = \frac{\tau_{nr}}{\tau_{rad} + \tau_{nr} + \kappa_{ISC}\tau_{rad}\tau_{nr}} = \frac{\tau_F}{\tau_{rad}} \tag{4.6}$$

where $\tau_F = \phi_F \tau_{rad}$ is the fluorescent life time. It is the measure of the effective life time of the singlet state, taking into account all possible decay source, except stimulated emission (it is always defined in non lasing case). The fluorescence life time is always shorter than the radiative life time.

Large oscillator strength dyes, where the fluorescence life time is nearly same as radiative life time, has high quantum yield. Diluted dye solutions are one good example that show high quantum yield [131]. Densely packed solid dyes or solutions with dye concentrations above 10^{-3} mol/l, show a high aggregation of dye molecules leading to fluorescent quenching [132, 133]. It was reported that the quantum yield ϕ_F can drops below 20 % for dye concentrations above 10^{-2} mol/l [133]. Hence, a separation of the dye molecules by a polymeric host matrix is indispensable to prevent aggregation (e.g formation of dimmers) in order to obtain a high quantum yield.

Stimulated emission

The molecules can also decay radiatively through stimulated emission. The rate of stimulated emission is defined by $\kappa_{SE} = \sigma_{em}I$, where σ_{em} is the stimulated emission cross-section (given in units of cm^2), and I is the intracavity laser intensity gain in photonic units (photon-flux per unit area).

The saturation intensity I_{sat}

The different decay rates depleting the S_1 state compete with each other and among the intra-molecular phenomena, the stimulated emission rate is the only one depending on the intensity. A useful quantity for lasers is the saturation intensity defined in terms of photonic units as:

$$I_{sat} = \frac{1}{\sigma_{em}\tau_F} \tag{4.7}$$

It can also be expressed in terms of energy units as:

$$I_{sat} = \frac{hc}{\lambda_{laser}\sigma_{em}\tau_F} \tag{4.8}$$

Organic materials have a saturation intensity in the order of few MW/cm^2. I_{sat} is the intracavity laser intensity for which the stimulated emission rate $\sigma_{em}I$ is equal to the spontaneous decay rate $1/\tau_F$. The later one includes all the non-radiative decays (IC and ISC). The condition $I > I_{sat}$ defines the lasing operating regime where stimulated emission dominate. In this case every photon from stimulated emission brings one excited molecule back to the ground state. Hence the population inversion becomes saturated and is very small [115].

It is worth to mention that the saturation intensity is an intracavity laser intensity and is not related to the pump laser intensity threshold; and it is not also directly related to the maximum intensity that can be produced by a laser. The saturated regime $I > I_{sat}$ is useful in laser systems where non-radiative pathways exist (and limit the efficiency and the photostability), as they can be quenched by stimulated emission. High laser intensities can be obtained using high-Q cavities for a given pump intensity [115].

Stimulated emission cross-section

Stimulated emission cross-section can be theoretically derived from optical gain characterizations, however, it is not simple to measure independently the singlet state population, particularly when steady state is not reached. This is particularly common in organic lasers operating with short pulses. Using Strickler-Berg relation [125] one can define the stimulated emission cross-section as:

$$\sigma_{em}(\lambda) = \frac{\lambda^4}{8\pi c n_F^2 \tau_{rad}} \frac{f(\lambda)}{\int f(\lambda)d\lambda} \tag{4.9}$$

where n_F is the refractive index in the emission spectral region, and $f(\lambda)$ is the fluorescence spectrum and τ_{rad} is the radiative life time. Since the latter also connected to the absorption cross-section σ_{abs}, one can find:

$$\int \frac{\sigma_{em}(\lambda)}{\lambda}d\lambda = \frac{n_F}{n_A} \int_{S_0 \to S_1(abs)} \frac{\sigma_{abs}}{\lambda}d\lambda \tag{4.10}$$

This leads to

$$\sigma_{em}(\lambda) = \frac{n_F}{n_A} \frac{\lambda^4 f(\lambda)}{\int \lambda^3 f(\lambda)d\lambda} \int_{S_0 \to S_1(abs)} \frac{\sigma_{abs}}{\lambda}d\lambda \tag{4.11}$$

The values of σ_{em} for dyes are in the order of $10^{-16}\ cm^2$ and therefore is several orders of magnitude larger than in other gain medium like rare-earth-doped crystals [121]

and inorganic semiconductors, like gallium arsenide [134].

In addition to the cross-section for stimulated emission (as shown in equation 4.11) the losses due to the cavity and also the self-absorption of the dye have to be considered for deriving the oscillation conditions of 4-level system. The total number of dye molecules per unit volume is defined by $n_t = n_0 + n_1$, where n_1 is the number density (per unit volume) of molecules in the first excited singlet state and n_0 is the number density of molecules in the ground singlet state. For the achievement of lasing in a cavity of Q quality-factor and n index of refraction, incorporating dyes as a gain media, the round-trip gain must overcome the total round-trip losses at the lasing wavelength λ [135] and is given by:

$$n_1\sigma_{em}(\lambda) \geq \alpha_{leakage}(\lambda) + \alpha_{abs}(\lambda) + n_0\sigma_{abs}(\lambda) \tag{4.12}$$

where $\alpha_{leakage}$ and α_{abs} are the leakage loss out of the cavity and absorption loss of the absorber (in inverse wavelengths) respectively[3]. For λ at resonance, $\alpha_{leakage}$ can be written as $\alpha_{leakage} = 2\pi n/\lambda Q$. Hence one can write equation 4.12 as:

$$n_1\sigma_{em}(\lambda) \geq \frac{2\pi n}{\lambda Q} + n_0\sigma_{abs}(\lambda) \tag{4.13}$$

The minimum fraction of molecules $\xi = n_1/n_t$ that must be excited to produce lasing is given by [136]:

$$\xi(\lambda) \geq \frac{2\pi n/(\lambda Q n_t) + \sigma_{abs}(\lambda)}{\sigma_{em}(\lambda) + \sigma_{abs}(\lambda)} \tag{4.14}$$

From equation 4.14 it is clear that the lasing threshold of dye lasers depends on the Q-factor and the density of dyes in the cavity. The lasing develops at wavelengths where $\xi(\lambda)$ is minimum. This can be calculated by inserting the cross-sections of absorption and stimulated emission into equation 4.14. From equation 4.14 it is also seen that a higher dye concentration leads to a lower lasing threshold but from practical observations an increase in the dye concentration beyond the limit leads to aggregation of the molecules and quenching of the fluorescence.

In the following section by doping optimum concentration of near unity quantum yield organic dyes into polymeric resonators, low threshold microlasers are realized. The fabrication process, the optical characterization and the lasing emission property of the dye lasers are discussed.

---

[3]If the fluorescence wavelength λ is not at resonance with the cavity, $\alpha_{leakage}$ is large and the
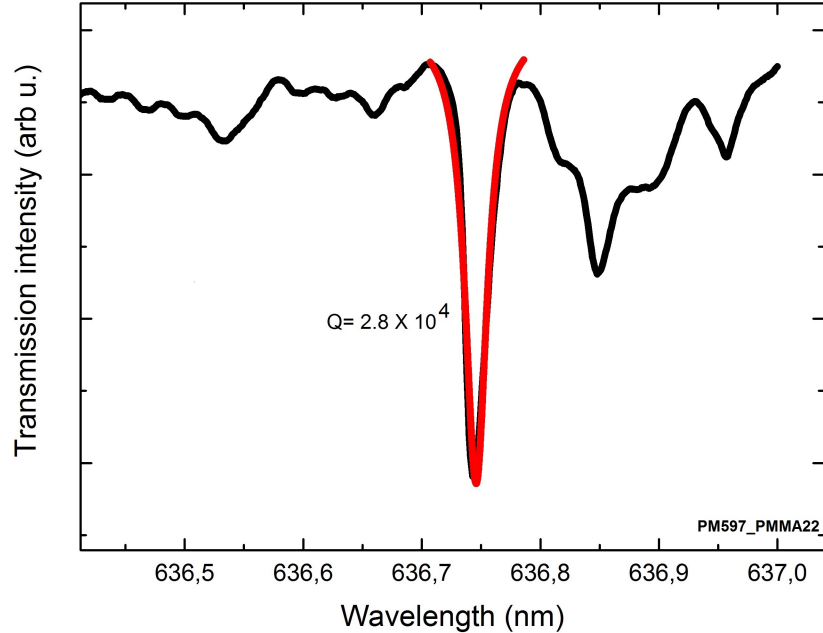
Figure 4.7: Transmission spectrum through an evanescently coupled tapered fiber shows complex WGM resonances of a PM597-doped microcavitiy. The Lorentzian fit of the mode at about 636.7 nm reveals a Q-factor of 2.8×10^4.

4.3 Pyrromethene 597 Dye-Doped Microlasers

For the realization of dye doped microlasers, the laser dye Pyrromethene 597 (PM597) are used. PM597 is a photostable dye which emits in the visible range from the green to the red part of the spectrum [137] with a high molar absorption coefficient (around $10^5 \, \mathrm{M}^{-1} \, \mathrm{cm}^{-1}$) and a near unity quantum yield [138]. The chemical structure, the absorption and the emission property of PM597 are depicted in Fig. 4.5(b). In addition to high photostability, PM597 has a further advantage due to a reduced triplet-triplet absorption within the emission band of the S_1 state [139] and also has low self-aggregation in organic solvents (this avoids fluorescence quenching of the monomer emission). In addition to this, PM597 is an ideal gain medium in PMMA-based resonators due to its perfect compatibility with the polymer host matrix. Hence, additional solvent before admixture to PMMA was not required and the dye was directly dissolved in the photo-resist before processing of the cavities. After integrating (doping) PM597 into the photoresist, the doped PMMA is spin coated on a silicon wafer and lithographic fabrication of microresonators is performed as

---

lasing conditions are not satisfied.
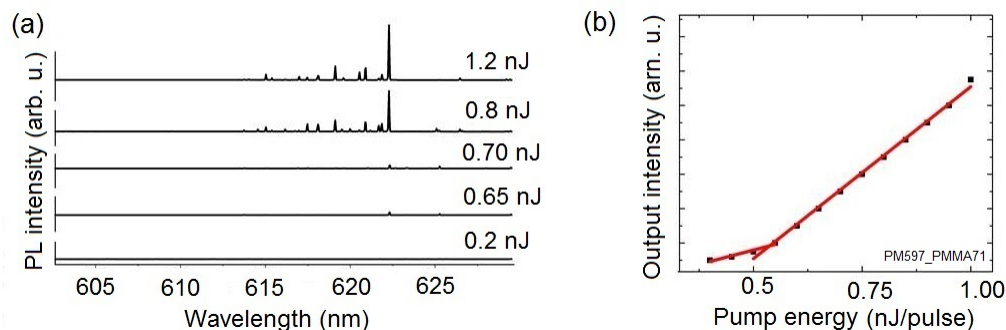
Figure 4.8: Emission spectra and lasing threshold of a PM597-doped microlaser. (a) Lasing spectra of dye-doped microcavity for different pump energies. (b) Input-output curve of a PM597 dye-doped microcavity (with a concentration $10\,\mu$mol/g solid PMMA) shows lasing threshold about $0.54\,$nJ/pulse.

discussed in chapter 2. The PM597 concentration varies between 10-25 μmol/g of solid PMMA.

Optical characterization

For the optical characterization of PM597-dye doped microresonators, light is evanescently coupled into resonators with radius of 22 μm via tapered fiber as discussed in chapter 2. The transmission modal spectrum shows complex WGMs, with a Q-factor reaching 2.8×10^4 near 636 nm as shown in Fig. 4.7. The Q-factor is reduced as compared to passive resonators due to the absorption of photons by the emitter and also the increase in the scattering effect as the result of the presence of more scatterers (dye molecules).

Free-space excitation

For fluorescence measurement of dye doped polymeric cavities, free-space excitation is used in a micro-photoluminescent setup (as depicted in Fig. 3.8). Since the dye has a higher absorption at about 530 nm, 10 ns pulses from a frequency-doubled Nd:YVO$_4$ laser at a pump wavelength of 532 nm (with a repetition rate of 93Hz) are used. The pulse width is chosen to be in few ns scales in order to prevent triplet state formation of the dye molecules (pulses with length shorter than 100 ns are required).

For the excitation-energy dependent measurement, the pockel cell along with a linear
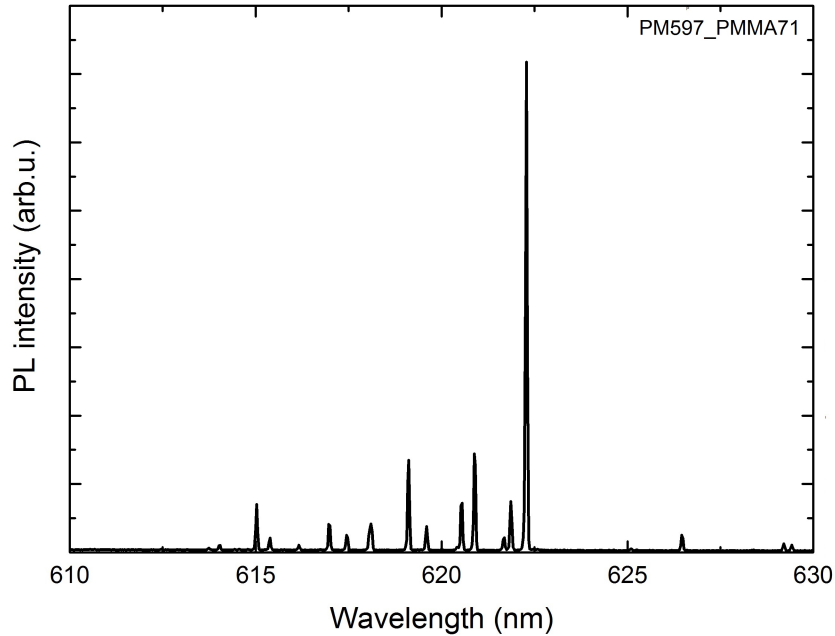
Figure 4.9: Lasing emission spectra of a PM597-doped microlaser at a pump energy of 0.8 nJ/pulse, which is much higher than the energy required for lasing.

polarizer is used. Fig. 4.8 shows the emission property of PM597-doped microgoblet with a radius of 22 μm (with a dye concentration of 10 μmol/g of solid PMMA). The output of the dye-doped microcavity as a function of the pump energy was recorded and a characteristic input-output curve shows low lasing threshold E_{th}= 0.54 nJ/pulse (Fig. 4.8 (b)). For pump energies above the lasing threshold, several narrow lasing peaks appear in the spectrum. Fig. 4.9 shows the lasing spectrum at the pump energy of 0.8 nJ/pulse, which is much more than the energy required for lasing. The spectral distance between the peaks is smaller than the expected free spectral range, hence in addition to the fundamental modes, several higher order cavity modes are also contributing to lasing.

As it is well described in ref. [19], the difference in the concentration of dye molecules in polymeric goblet resonators leads to a difference in the threshold energy. An increase in threshold energy with increase in dye concentration (from 3-16 μmol/g of solid PMMA) is obtained [19]. This is due to the decrease in the Q-factor of the cavity as the result of an increase in absorption and scattering of cavity photons by the dye molecules as discussed in the previous section. The higher concentration of the dye molecules also lead to aggregation and decrease the internal quantum efficiency [133]. Too low concentration (for example 1 μmol/g of solid PMMA) also

leads to high lasing threshold due to reduced absorption of pump energy in the 1-1.5 μm thick cavity via free-space excitation technique, leading to reduced gain as the result of smaller number of dyes [19].

In addition to its good lasing performance, PM597 doped microgoblet lasers have long operational life time of more than 2×10^6 pulses (more than 5 operational hrs.) [19]. This makes the device suitable for applications where several time operation is needed (e.g biosensing applications).

4.4   Summary and Conclusions

In this chapter, the electrical and optical properties of π-conjugated organic molecules as a gain medium were discussed. Due to the compatibility of PM597 with PMMA, the laser dye was directly doped into polymer host matrix before processing of the cavities. After lithographic fabrication, optical characterization and fluorescent measurement were conducted. It was observed that laser dye-doped resonators acquire Q-factors reaching up to 2.8×10^4. The decrease in the Q-factor is attributed to the absorption of cavity photons by the laser dye and the scattering associated with the presence of the dye molecules. Excitation intensity dependent measurements show low threshold lasing ($\backsim 0.54$ nJ/pulse). The WGM laser emission from PM597 dye-doped cavity was very stable and have operational life time. These lasers are applicable for label-free molecule detection [19], for the formation of photonic molecules [17] and tunable microlasers [140]. The latter is discussed in the next chapter.

Chapter 5

Photo-Induced Tuning of Polymeric Microresonators

Polymeric whispering gallery mode (WGM) resonators made from PMMA have outstanding optical properties like high Q-factors as discussed in chapter 2 and are also suitable for the integration of quantum emitters like quantum dots and laser dyes as it is presented in chapter 3 and 4 respectively. However, room temperature photonic-mode control and tunability of the resonance (laser modes) is indispensable for robust device applications. To do so a photo-responsive smart material is required. Responsive polymeric materials have the capability of executing specific functions in response to changes in stimuli (like temperature, electric field, light, etc) and have potential applications in many areas.

Liquid crystal elastomers (LCE) are one of the smart materials that offer a platform for realizing responsive photonic systems. LCEs are solid-state materials that combine orientational order of liquid crystals (LCs) with the elastic properties of long, cross-linked polymer chains. It is among one of the smart artificial materials that converts external stimuli into mechanical actuation to perform reversible shape deformation. Different types of dopant molecules and alignment of molecules can be chosen to make the polymer sensitive to temperature, light, pH, humidity and alike. The liquid crystalline units of the network amplify the dopant action, leading to fast and large responses. These responses can be optical or mechanical changes and can be tuned to be reversible (or non-reversible) depending on the application required.

In this chapter optically controlled, stable and perfectly reversible tunable microresonators (lasers) are realized. The tuning is made over a large spectral range (high finesse). The chapter begins with a discussion of the basics of liquid crystals and liq-

uid crystal elastomers and also discusses the fabrication of azo-dye integrated LCE micro-actuators (polymerized via two photon absorption induced 3D direct laser writing). Then for photo-induced tuning of the resonators, the integration technique of LCE/goblet laser resonators, its optical characterization, and the tuning mechanism for different pump energy densities is presented.

5.1   Basics of Liquid Crystalline Elastomers

5.1.1   Liquid crystals

Liquid crystals (LCs) are materials that have properties between conventional liquids and solid crystals. Hence they can flow and show at the same time typical properties of liquids while their molecules are oriented like crystalline states of matter. Liquid crystal materials in general have several common properties like; a rod-like molecular structure (anisotropic structure with one axis appreciably longer than the other axis) and strong dipoles and/or easily polarizable substituents. In contrast to liquids, which have no intrinsic order, the liquid crystals have their molecules (commonly called mesogens) to point along a common axis, called the director. In the solid state molecules are highly ordered and have little translational freedom. The common characteristic orientational order of the liquid crystal state is intermediate between the solid and liquid phases and this is why the term mesogenic state is used synonymously with liquid crystal state. It is known that polymers exhibit anisotropic properties if a macroscopic order is generated. This leads to different physical properties in the direction of the alignment and the two perpendicular axes [141]. Similarly densely cross-linked polymer networks of the LC acrylate-based systems show a large difference in their properties along and perpendicular to the monomeric unit. In this chapter optical properties and structural deformations will be discussed with the molecular alignment direction (director) as a reference.

In the general sense the LC state can be obtained either lyotropically, by varying a composition of a multi-component system, or thermopically, by varying temperature. A lyotropic LC phase is achieved by dissolving amphiphilic molecules in a solvent where their phase transitions can be observed through the addition or removal of the solvent. Thermotropic LC structures are observed in a particular temperature range. At a high temperature, the LC material shows isotropic behaviour of a liquid while at low temperatures it shows typical crystal structures of a solid. Moving from low to high temperature, the LC material exhibits various different structures [142].

Depending on the orientation of the alignment, LCs can be found in one of the
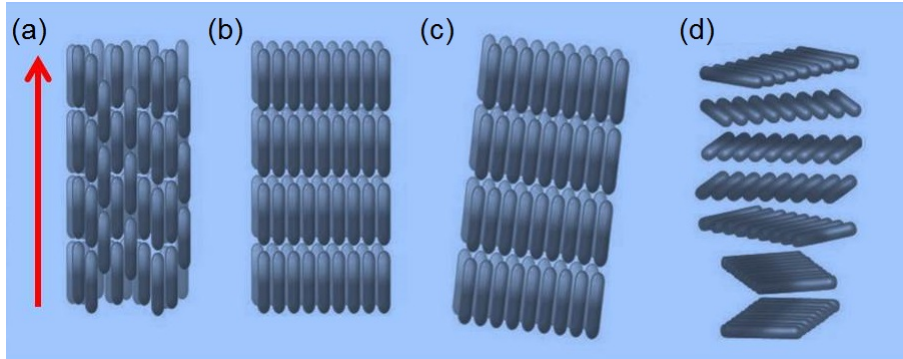
Figure 5.1: Schematic representation of different liquid crystal (LC) phases. (a) nematic phase, (b) smectic A phase, (c) smectic C phase, (d) cholesteric phase.

three phases: nematic, smectic, and cholesteric as shown schematically in Fig. 5.1. In the nematic phase structure LC molecules are arranged along the direction of the director but have the freedom of moving (rotating) in either direction along their long axis (see Fig. 5.1 (a)). Hence this particular phase has long orientational order but a short positional order of the LC structure. Due to this orientational order, nematic LCs show anisotropy in various physical properties for instance optical birefringence, viscosity, electrical, magnetic response and so on [142].

Unlike for the nematic phase, LCs in smectic phase can be found at lower temperatures and they possess both orientational and positional order. Since they are biaxially aligned, they form a layer and the alignment is both along their long and short axis. Depending upon their molecular arrangement within a layer, there are different semectic phases labelled as A, B, C, E, F, and so on. Smectic A and smectic C phases are most common types and differ only by the position of the molecular axis with respect to the layers normal axis. Smectic A structure has a molecular long axis parallel to the layers normal axis (Fig. 5.1 (b)), where as in smectic C phase it is tilted with an angle θ as shown schematically in Fig. 5.1 (c). The other types are also differing according to the crystal structure of molecules within the layer [143].

The cholesteric phase, sometimes also called chiral phase, has the director twisted about an axis normal to the molecular orientation (following a helical path). The twisting can be right-handed or left-handed depending on the molecular conformation (Fig. 5.1 (d)). Iridescent colors are characteristic of cholesteric phases [144,145].
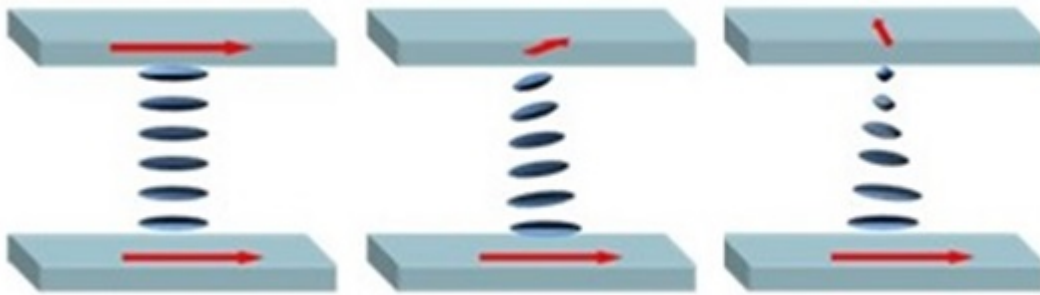
Figure 5.2: Schematic diagram of the alignmenmt of LC molecules using PI coating and surface anchoring. The LC molecules oriented along the rubbing direction.

5.1.2   External influences on liquid crystals

External stimuli (perturbations) can cause significant change in the macroscopic property of the liquid crystal system. Temperature, electric and magnetic field can be used to induce these changes. For practical applications the magnitude of the fields and also the response time of the aligned molecules play a significant role. For the alignment of the molecules in liquid crystal devices specific surface treatment need to be applied. Some of the common techniques are discussed below.

I-Electric and magnetic field effects

The response of liquid crystal molecules to an applied electric field can be used to manipulate the direction of the alignment. The director aligns along an external field due to the electric nature of the molecules. When one end of a molecule has a net positive charge and the other end has a net negative charge, permanent electric dipoles are created. When an external electric field is applied to the liquid crystal, the dipole LC molecules align themselves along the direction of the field. Sometimes a permanent dipole may not be formed, even in that case the external electric field re-arranges the electrons and protons in the molecule leading to an induced electric dipole and consequently to an orientation of the molecules, though it is not as strong as permanent dipoles. The effect of a magnetic field on liquid crystal molecules is similar to the electric fields as magnetic fields are generated by moving charges. Similarly permanent magnetic dipoles are produced due to the electrons moving in the atom. When an external magnetic field is applied, the LC molecules align in the

same or opposite direction to the field [146].

II-Surface Preparations (Surface anchoring)

When there is no electric or magnetic field, the director of a liquid crystal is arbitrarily pointing in any direction. However, even without using any external field the director can be aligned in a specific direction by introducing an outside agent to the system. This is possible using a thin polymer coating (polyimide (PI)) on a glass substrate, which is rubbed in a single direction. It is observed that liquid crystal molecules in contact with such a surface align themselves along the rubbing direction [1]. This technique is useful when the long axis of the molecule is required to be aligned along the plane of the substrate (parallel to the plane of the substrate). The liquid crystals can also be aligned perpendicular to the substrate only by PI coating (no rubbing). Schematic diagram of the alignment of LCs by surface anchoring is depicted in Fig. 5.2.

III-Freedericksz Transition

The orientation produced by surface anchoring and also by external applied electric field can be exploited together in liquid crystal molecular orientation. For example, aligning the liquid crystal molecules parallel to the surface using PI coating and rubbing and apply an electric field perpendicular to the cell: In the beginning the increase in electric field does not change the alignment but at some threshold magnitude of the electric field deformation will occur. This deformation happens as the director changes its orientation from one molecule to the other and is known by the name Freedericksz transition. The same holds true using a magnetic field of a sufficient strength.

---

[1]The origin of the alignment of liquid crystal (LC) molecules on rubbed polymer surfaces has remained a puzzle since its discovery in 1911. In general, the LC alignment has to originate from symmetry breaking at the surface of the polymer substrate. Asymmetries in either the macroscopic topographical or microscopic molecular structure of the polymer surface have been proposed for its origin [147]. Currently there is also a group who think the alignment is occurred due to an epitaxial growth of the liquid crystal layers on the partially aligned polymer chains in the near surface layers of the polymide (still debatable).

Refractive indices of LCs

Due to their anisotropic nature liquid crystals are birefringent materials [2]. When light enters a nematic liquid crystal sample (like other birefringent materials), the light is broken up into the fast (called the ordinary ray) and slow (called the extraordinary ray) components. As the result of the different velocities of the ordinary and extraordinary light, the waves get out of phase. When the rays are recombined as they exit the birefringent LC material, the phase difference leads to a change in the polarization state of the output. The birefringence of a material is mainly characterized by the difference in the indices of refraction for the ordinary and extraordinary rays Δn. Since the index of refraction of a material is defined as the ratio of the speed of light in vacuum to that in the material, the indices for are given by $n_e = c/v_{\parallel}$ and $n_o = c/v_{\perp}$ for the velocities of a wave travelling perpendicular to the director and polarized parallel (extraordinary) and perpendicular to the director (ordinary) respectively, so that the birefringence is $\Delta n = n_e - n_o$. The condition $n_e > n_o$ describes a positive uni-axial material and nematic liquid crystals belong to this category.

Refractive indices of a uni-axial thermotropic liquid crystal are dominantly governed by the molecular constituents, wavelength, and temperature. In the visible spectral region, the ordinary index of refraction n_o is typically in the range from 1.50 to 1.57. n_o is not very sensitive to the molecular constituents of the LC, but is rather dependent on the wavelength (λ) and the temperature. As the wavelength λ increases, n_o decreases but saturates in the near-IR region. But n_o increases slightly as the temperature of the LC sample increases. A more pronounced increase in n_o is observed near the phase transition temperature (from nematic to isotropic phase) [148].

Unlike the ordinary index of refraction, the extraordinary index of refraction n_e is very sensitive and dependent on the molecular constituents of the LC. In the visible range it varies from about 1.5 (for a totally saturated compound) to about 1.9 (for a highly conjugated LC) in the visible region. Like n_o, n_e decreases as the wavelength λ increases. Unlike n_o, n_e decreases as the temperature increases, and drops sharply as the temperature reaches the phase transition point. Beyond the clearing point the LC becomes an isotropic liquid and n_e coincides with n_o (Δn vanishes) [148].

---

[2]Birefringence is an optical property in which a single ray of unpolarized light entering an anisotropic medium is split into two rays, each travelling in different directions. One ray (called the extraordinary ray) is bent (refracted) at an angle as it travels through the medium. The other ray is called the ordinary ray and it is still follows Snell's law of refraction as it passes through the medium. Hence, they acquire double refraction (having two indices of refraction) leading to different velocity of light in this two directions.

5.1.3   Liquid crystalline elastomers (LCEs)

LCEs are solid-state materials that combine orientational order of liquid crystals with the elastic properties of long, cross-linked polymer chains [149–152]. Due to its LC properties LCE mesogens exhibit a molecular order and cross-linked structure, which leads to many characteristic properties. Depending on the alignment of the molecules and its positional order they can be classified as nematic LCEs, smectic LCEs, and cholesteric LCEs [153]. On the network the mesogenic groups attached in different ways (with their microscopic properties of LCs) thus introducing the liquid crystal order.

A mesogen used for LCE consists of three distinct components: The first part is called a reactive group and takes part in the polymerization reaction. The second part is called a spacer unit that separates the core of the mesogen from the reactive group. The last part is called the core component, usually composed of cyclic structures such as benzene, cyclohexane, or heterocyclic rings. Fig. 5.3 (a) shows the three different parts of a LCE mesogen. Depending on the attachment of the reactive group the mesogens can be side chain mesogen or main chain mesogen[3].

The structure of the mesogen core varies depending on the type of LC used. Mostly LCs have an anisotropic shape and are based upon various ring structures such as benzene, cyclohexane and biphenol derivatives mesogens. As the number of rings is increased, the isotropic phase transition temperature tends to increase. Phase transitions strongly depend on the nature of the ring and spacer. In this work the commonly used monomer is depicted in Fig. 5.3 (b).

Synthesis

The idea of LCEs has been extensively investigated by researchers since they are proposed for the first time by de Gennes [154]. J. Kupfer and H. Finkelmann made a major breakthrough when they successfully synthesized nematic monodomain LCEs [155] (see Fig. 5.4). After that time different structures of LCEs with a variety of mesogens have been prepared. One of the important factors in the preparation of LCEs is to perform the polymerization process at temperatures where the system exhibits a LC phase. LCEs can be synthesized by different routes. There are 4 common synthesis techniques which are presented in the following:

---

[3]Side chain mesogens are linked with the polymer chain only in one side, where as main chain mesogens are linked to the chain on both sides so that they have reactive group at both ends of the mesogen (see Fig. 5.7).
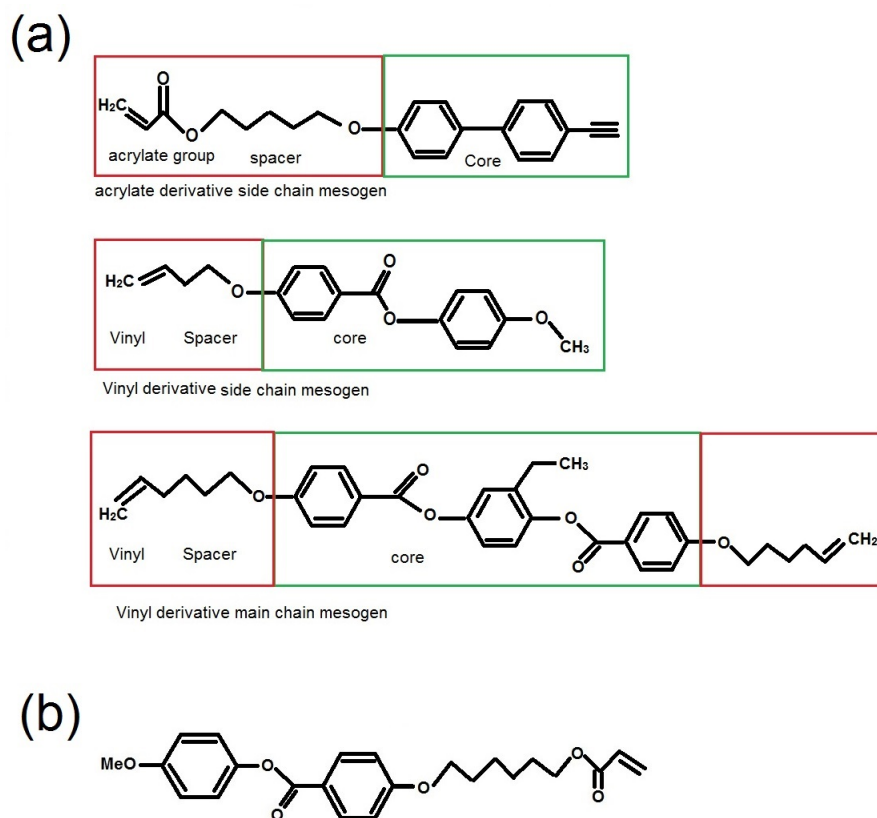
Figure 5.3: (a) The different functional groups of the mesogen. The red marked part shows the reactive group that participates in the polymerization process. The spacer part separates the reactive group from the core (green). Depending on the reactive part the mesogens can have a side chain or main chain configuration for polymerization. (b) Side chain LC mesogen used in this work.

The first method commonly utilizes siloxane chemistry. In this route in one-step a linear non-functional/functional polyhydrosiloxane chain is coupled to the mesogenic groups and is cross-linked. This reaction is mediated by platinum catalyze and results in the attachment of mesogens and cross-linking moieties to polyhydrosiloxane backbone [156]. Due to the kinetics of the reaction vinyl groups react about two orders of magnitude faster than methacryloyl groups. This makes the cross linking process two steps as fast reaction of vinyl groups leads to a weakly cross-linked network. A final complete cross-linking is obtained in the second step by high temperature slow reaction of methacryloyl groups. Utilizing this technique different types of LCEs have been produced like side-on mesogens [157, 158], end-on mesogens [155], main-chain polymers [159], photosensitive side-groups [156]. The
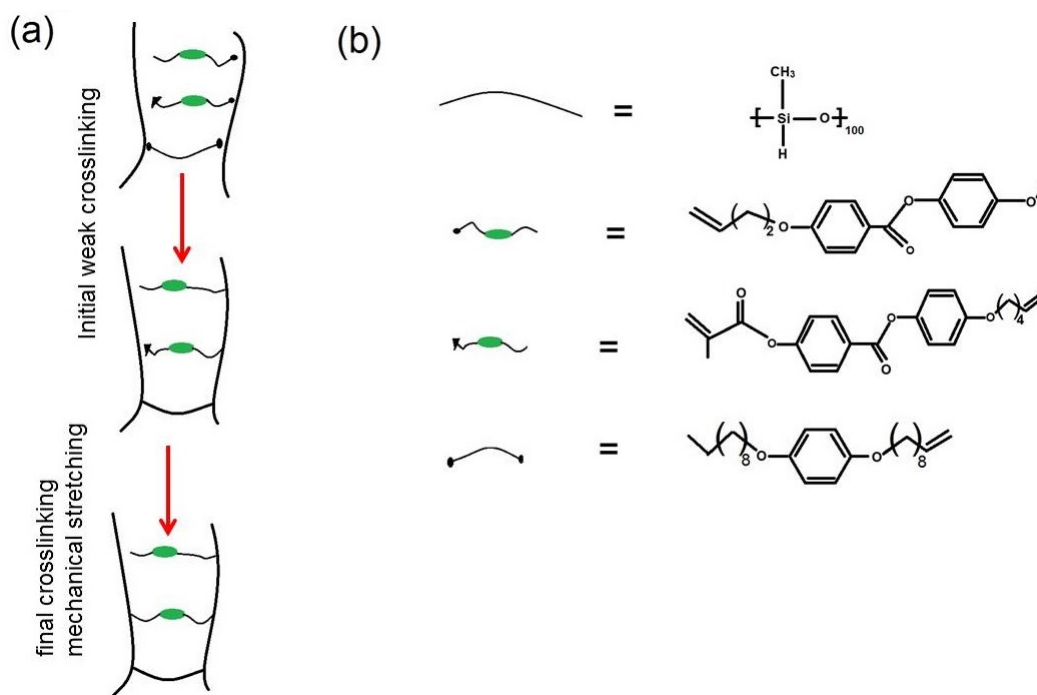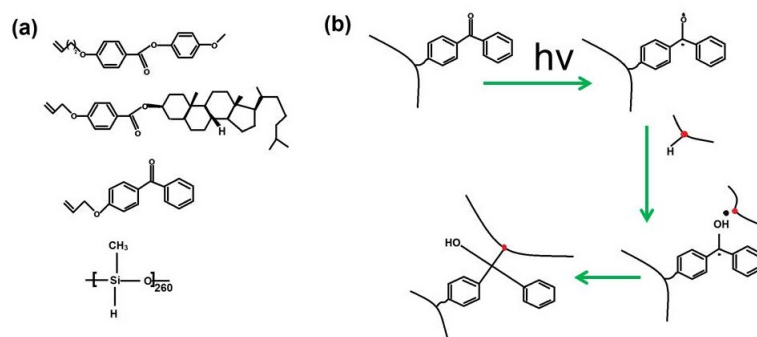
Figure 5.4: (a) Schematic representation the synthesis of monodomain nematic liquid crystalline elastomers (LCEs) proposed by Kupfer and Finkelmann (modified picture from [155]). (b) Chemical structures of polymer chain, LC monomer and cross-linkers used for the synthesis monodomain nematic LCEs [144, 155].

benefit of this technique is that it is easy to exchange mesogenic compounds without making considerable changes in the whole structure. The common problem of the technique can be an incomplete reaction from low molar mass materials (unreacted mesogens or cross-linker). These unreacted mesogens/cross-linkers remain in the elastomer and might migrate and phase separate. The purification of these impurities is only possible by extracting them from the elastomer using a suitable solvent, which is time consuming and is not always complete [144, 153].

The second technique is a two-step process where initially liquid crystalline polymer which contain additional functional groups is synthesized. Then it is mixed with a multifunctional cross-linking agent which reacts selectively with the functional groups, resulting a network formation. This technique has been usually used for the cross-linking of polyacrylate or methacrylates. In most cases the cross-linking is done by integration of click-reaction of azides and acetylenes [160], isocyanates to alcohols [161], reaction of active ester and amines [162] and by hydrosilylation reaction [163]. The impurities during the synthesis of the elastomers can be purified

Figure 5.5: (a) Chemical structures of the molecules used for the synthesis of photo-crosslinked monodomain LCEs by Komp et al. [164]. (b) Schematic representation of photo-induced cross-linking mechanism [144].
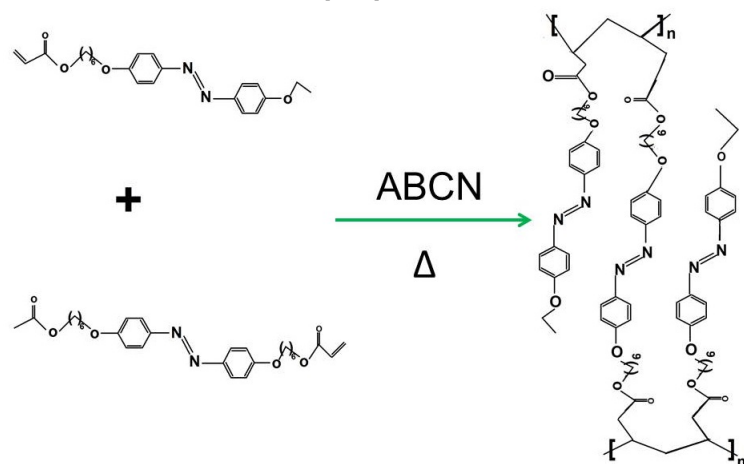

Figure 5.6: Synthetic technique of photosensitive LCEs [165]. The polymerizations leading to LCEs are initiated thermally by mixing monomer and cross-linker and initiator.

easily as compared to the first technique as they can be purified before the final cross-linking process.

In the third technique the LC polymer contains cross-linkers which can be cross-linked via photons [164–166] (see Fig. 5.5) or by thermal or UV exposure [166]. This synthetic route has the difficulty in achieving high degrees of cross-linking as one uses a LC prepolymer that contains cross-linkable groups and steric hindrance, which makes it difficult to achieve high degrees of cross-linking [144]. By this approach a high purity can be achieved (similar as in second technique) as LC polymer can be purified before the cross-linking step.

The fourth technique uses a different approach. In this route LCEs are prepared
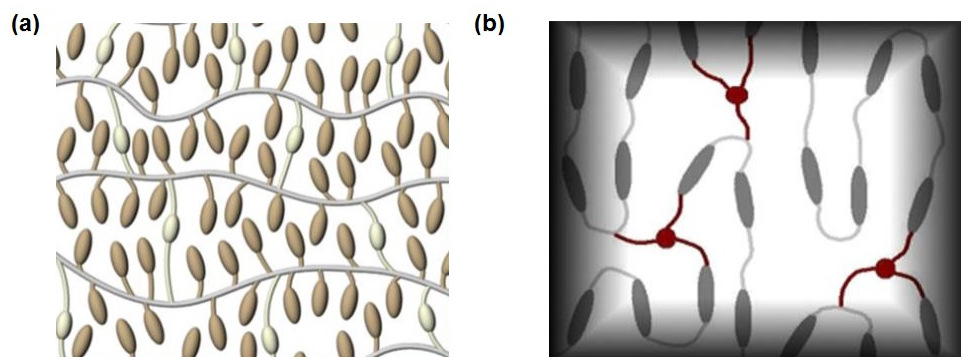
Figure 5.7: (a) LCE with mesogenic groups on the side. (b) LCE with mesogenic groups as a part of the chain [167].
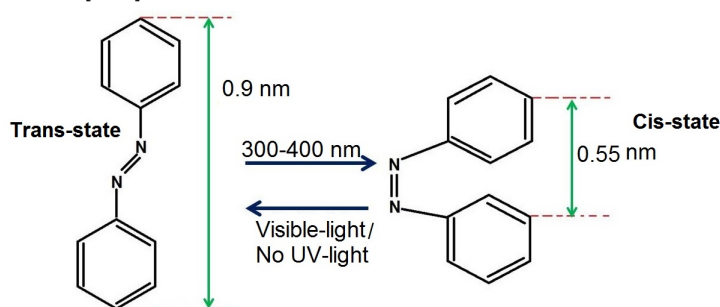
Figure 5.8: Trans-cis isomerization of azobenzene [168]. Azobenzenes under go a transition from trans-state to the cis-state under UV exposure. This is accompanied by a decrease in the size of the molecular structure (the distance between carbon 4-4' carbon decreases from 0.9 nm to 0.55 nm) [168].

by mixing a LC monomer, a multifunctional cross-linker and a radical initiator together in one step (see Fig. 5.6). Depending on the type of initiator used the polymerization reaction (leading to LCE structures) can be initiated thermally or with UV irradiation. Fig. 5.6 shows the route for the synthesis of photosensitive LCEs.

After the final polymerization process of LCE the mesogenic groups can be bind as a part of the chain (main chain) or can be just pendant on the chain (side chain LCEs) as depicted in Fig. 5.7. In this work photo-initiated cross-linking and polymerization of LCE is realized as discussed in the following:

5.1.4   Azobenzene chromophore

Photo-responsive LCEs can be fabricated by the integration of photosensitive molecules like cinnamylidene/azo compounds and cinnamic acid (CA). One of the commonly known photosensitive molecules widely used for such application is azobenzene. This photosensitive molecule has a fast response on exposure to an appropriate wavelength of light [169]. Azobenzene has two aromatic rings with an azo linkage (N=N) joins the two phenyl-rings. So far different kinds of azo chromophores are obtained by changing the aromatic ring of the chromophore with various substituents to change the geometry and electron donating/withdrawing mechanism [144]. Most of the azo-based chromophores have similar photophysical properties as they are π-conjugated systems and have strong electronic absorption in the UV/visible part of the electromagnetic spectrum depending on the ring-substitution pattern.

The azobenzene molecule exhibits LC behaviour, which makes this molecule ideal for the synthesis of photo-responsive LC materials. One of the most interesting properties of azobenzene (and similar molecules with a substituted aromatic ring) is its fast and reversible photo-isomerization process. Photo-isomerization occurs when light of a particular wavelength is irradiated on the dye. Azobenzenes possess two isomerization configurations: a thermally stable trans-state and a meta-stable cis-state. For example, the azobeneze structure shown in Fig. 5.8 under goes a transition from trans-state to the cis-state under UV exposure. This is accompanied by a decrease in the size of the molecular structure (the distance between carbon 4-4' carbon decreases from 0.9 nm to 0.55 nm) [168]. The cis-state thermally returns to the more stable trans-state when the light is off or upon illumination with a visible light. The rate of state transformation is dependent on the molecule's particular substitution pattern. This remarkable photo-responsive effect provides a room for new optical devices where photo-switching and light-dependent control is needed.

In the next section the fabrication of photo-responsive (azo-dye integrated) LCE micro-actuators is presented. The polymerization process of the monomer mixtures via 3D laser lithography and the photo-mechanical deformation of the elastomers are also discussed.

5.1.5   3D-direct laser writing for liquid crystalline elastomer microstructures

Liquid crystal elastomers are made by polymerization and cross-linking of monomer mixtures. Direct laser writing (DLW) is used for the fabrication of 3D LCE structures via a two photon absorption induced polymerization process. DLW is a well-
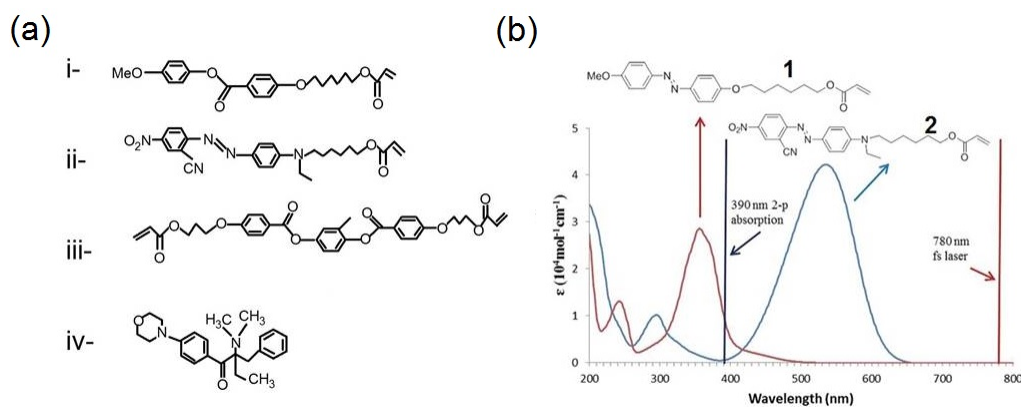
Figure 5.9: (a) Components of the monomer mixture: i- LC mesogens, ii- azo-dye, iii-cross-linker, iv- photo-initiator. (b) Absorption spectra of common azo-dye (1) and the azo-dye used for 3D DLW process (2). The absorption is tuned by changing the substituent on the aromatic ring of the dye [170].

developed technique for the fabrication of 3D structures and best suited for the fabrication of LCE structures as it maintains the designed (required) molecular alignment [170] in sub-micrometer resolution [171, 172].

The LC monomer mixtures used in this work consist of LC mesogens, cross-linkers, azo-dye and photo-initiator. The LC mesogen is used for good nematic alignment of the molecules and provide the liquid crystalline properties. Cross-linkers are used to obtain elastomeric properties in the entire polymer structure. The photo-initiator is used to trigger a chain reaction for polymerization under ultraviolet (two-photon) exposure.

The role attributed to the photo-responsive azo-dye is the enhancement of the local temperature of the LCE cylinder when it undergoes fast trans-cis isomerization via the absorption of resonant photons as discussed in the previous section. The chemical structure of the mixture is shown in Fig. 5.9 (a). Commonly commercial azo-dyes show maximum absorption for the photo-isomerization at about 350 nm [173, 174]. Hence these dyes are not suited for a DLW polymerization process as its absorption overlaps with the two photon absorption peak of the photo-initiator. For this reason the absorption maximum of the azo-dye is tuned to around 530 nm by changing the substituent on the aromatic rings [170]. Fig. 5.9 (b) shows the absorption spectra of common (commercial) azo-dye (1) and the synthesized azo-dye (2) used for DLW.

In order to align the molecules nematically, polyimide (PI1211 Nissan Chemical Industries) coated glass cell is prepared as discussed in previous section. Depending on the required orientation of the molecules the PI coated glass plates can be
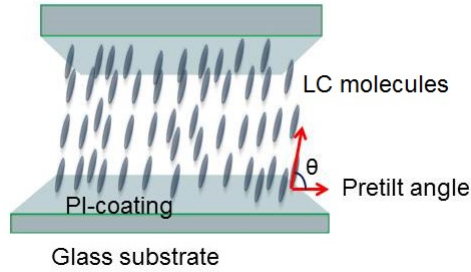
Figure 5.10: Schematic diagram of the alignment of LCs by PI coating. PI coating with out rubbing leads to an alignment with 90° pretilt angle.
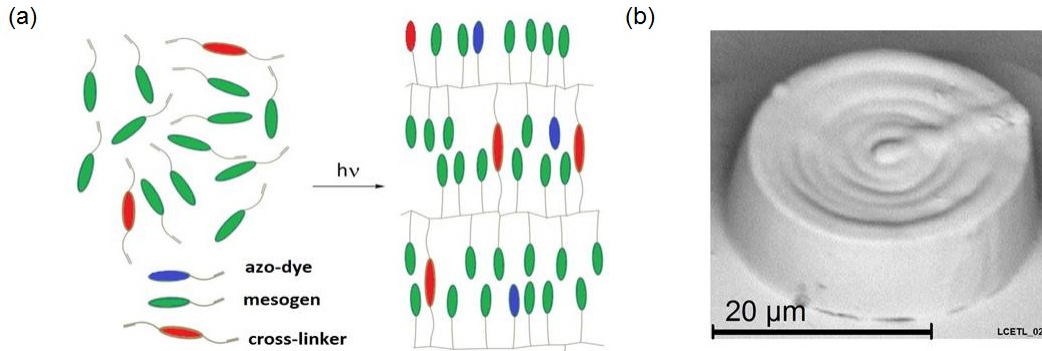

Figure 5.11: (a) Schematic diagram of the polymerization process. (b) Scanning electron micrograph image of a polymerized LCE microcylinder structure.

rubbed (no rubbing for 90° pretilt angle uniaxial alignments of the LC molecules (perpendicular to the glass substrate) as depicted in Fig. 5.10.

After preparing the glass plates for the alignment of the molecules, the LC mixture is heated upto 60 °C and infiltrated into this cell. The cell has a 50 μm gap between the glass substrates. Two photon absorption polymerization of the infiltrated LC monomer mixture was induced by a 130 femtosecond pulsed laser (with a repetition rate of 100 MHz) at 780 nm from a commercial DLW work station (Photonic Professional, Nanoscribe GmbH). The laser beam was circularly polarized and focused with a (100×, 1.4 NA) oil objective (Zeiss, Plan Apochromat). The LCE microstructures were written on the bottom inner surface of the glass plate and the sample position is controlled by a 3D piezo translational stage.

After the DLW process the sample is developed with toluene and result in LCE microstructures. Fig. 5.11(a) shows the schematic representation of the polymerization process. The scanning electron micrograph image of a LCE microcylinder structure fabricated via DLW process is depicted in Fig. 5.11(b). The structure has a cylin-
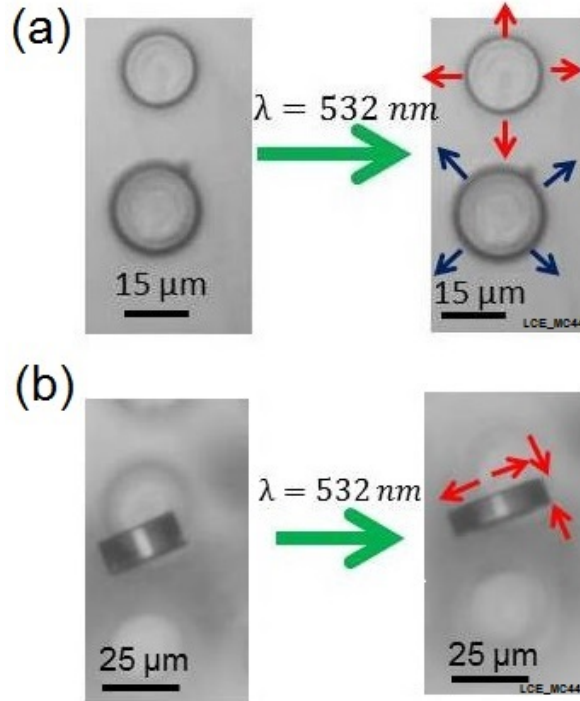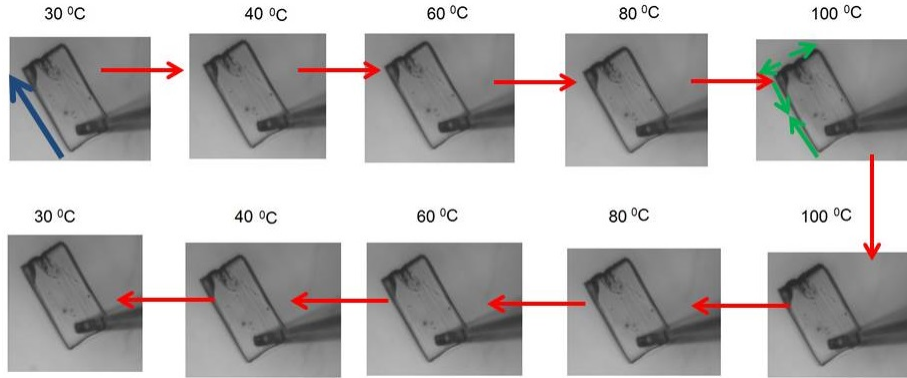
Figure 5.12: (a) Optical microscopy image of a microcylinders showing expansion along the plane perpendicular to the alignment direction. The image is taken from the top view of the LCE microcylinders. (b) Optical microscopy image of a microcylinder showing contraction and expansion along the plane parallel and perpendicular to the alignment direction respectively. The image is taken by flipping the LCE on its side.

drical shape of 25 μm diameter and 10 μm height and the molecules are nematically aligned along the z-axis of the cylinder.

Illumination of the sample with light of wavelength of 532 nm leads to the absorption of the green light by the azo-dye (followed by trans-cis isomerization and thermal relaxation). This leads to an increase in the local temperature of the LCE and the molecular order of the nematic phase of elastomer is therefore distorted which also leads to a structural deformation. The LCE microcylinder expands perpendicular to the alignment direction (along the plane perpendicular to the axis of the cylinder) as depicted in Fig. 5.12 (a) and contracts in the other transverse direction (Fig. 5.12 (b)).

The LCE mixtures can also be aligned along the plane of the glass plate (via PI-coating and rubbing) as discussed in the previous section. Similarly polymerization

Figure 5.13: Optical microscopy image of thermal-induced structural deformation of rectangular prism of size 100 μm length, 50 μm width and 10 μm hight. As the temperature increases the LCE showing contraction and expansion along the plane parallel and perpendicular to the alignment direction respectively. As the temperature decreases the nematic ordered phase is restored leading to reversibility.

of the infiltrated LC solution via two photon absorption leads to LCE structures with the director along the plane of the substrate. Fig. 5.13 shows a rectangular prism of 100 μm length, 50 μm width and 10 μm height. The director is indicated by the blue arrow. To see the deformation the sample is placed on a temperature controlled plate and monitored on a camera. The sample shows a reversible change in the shape while the temperature changes from 30°C- 100°C and vice versa during decreasing temperature. Again during heating the nematic molecular order of the LCE is distorted and the elastomer contracts along the direction of the alignment and relaxes in the transverse direction. The green arrow in Fig. 5.13 shows the corresponding size change of the LCE along and opposite to the alignment direction as the temperature of the elastomer increases.

So far the fabrication process and the photo/thermal-induced structural deformation of nematic LCE is discussed. In the next section using the photo-responsive mechanical deformation of the elastomer, the control of the resonance modes of polymeric goblet resonator are presented.

5.2   Optically Controlled Elastic Microcavities

In the following a possibility for controlled, reversible, dynamic tuning of polymeric WGM resonators is presented. This tunability is based on the integration of photo-responsive liquid crystalline elastomer microcylinder actuators into goblet resona-

tors. The integration of photo-responsive LCE microactuators into PMMA goblet resonators, its optical characterization and the tuning mechanism are the central point of this section[4] .

5.2.1   Fabrication

Polymeric WGM resonators are lithographically structured PMMA disks on a silicon chip. A subsequent thermal reflow process leads to goblet-type cavity geometry as discussed in chapter 2. These resonators are compatible with large-scale fabrication and are mechanically stable. Tuning of the cavity resonances discussed in this section is linked to the control of the resonator diameter.

In the first step Pyrromethene 597 (PM 597) dope microdisk lasers, with a dye concentration of 12 μmol/g solid PMMA, are fabricated via e-beam lithography (with a dose current of 500 pA) as presented in chapter 4.

The second constituent of each tunable resonator is the photo-responsive nematic LCE microcylinder (director along the axis of the cylinder). The LC monomer mixtures (the same chemical structures as depicted in Fig. 5.9 (a)) are composed of 71 % of LC mesogens, 2 % of photo-initiator, 26 % of cross-linker and about 1 % of azo-dye (the compositions are percentage by mass). The photo-responsive azo-dye absorption wavelength (about 530 nm) coincides with the pump wavelength of PM 597-doped laser cavities. Therefore pumping the dye-doped cavity and also LCE deformation is performed by the same laser source.

After the fabrication of LCE microcylinders by DLW they are centred on top of the PMMA microdisk resonators using a micro-positioning system. The cylinders can easily be detached from its glass substrate upon heating the sample to 100 °C for 10-15 minutes (see Fig. 5.14). Micro-tips (made from optical fibers) are used to place the LCE microcylinders (25 μm diameter, 10 μm height) on top of polymeric microdisk resonators with a diameter of 49 μm as shown in Fig. 5.15 (a). Then a thermal reflow treatment (30-40 s on a hot plate at temperature of 125 °C leads to the surface-tension induced goblet structure, smoothens the surface of the cavity and fuses the LCE into the base of the goblet resonator. After the heat reflow process the diameter of the resonator is decreased to 45 μm. Scanning electron micrograph images of a LCE/goblet resonator are shown in Fig. 5.15 (b), (c) and (d).

---

[4]The results presented in this section are submitted for publication to Light: Science and Application (2014)
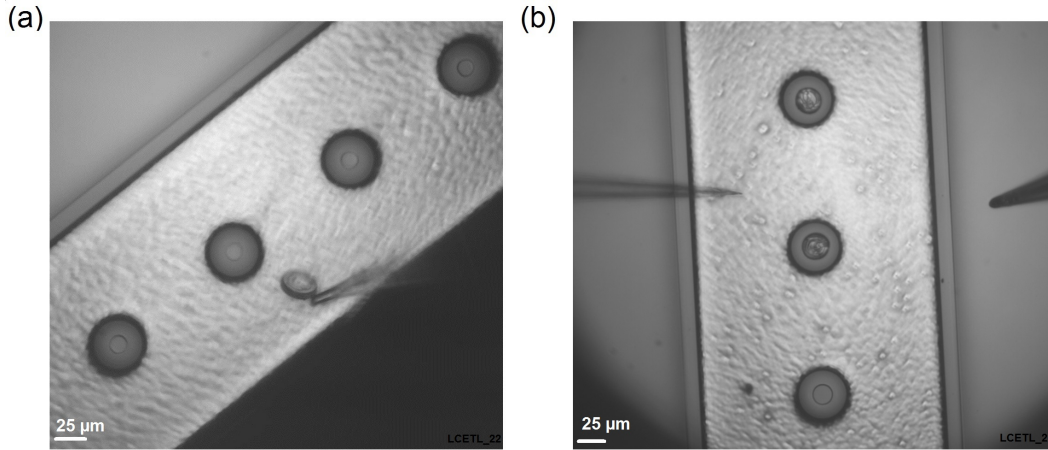
Figure 5.14: (a) Optical microscopy image of micro-positioning of LCE microcylinders on the top of polymeric microdisk resonators. The LCE microcylinders are easily detached from the glass substrate and can be handled easily using the few μm fiber tips. (b) The LCE cylinders are placed on the top-center of polymeric disk resonators.

5.2.2   Optical characterization

It is important to test whether the optical quality of the goblet resonators are affected by the integration of the LCE microcylinders. To measure the Q-factor, a tapered fiber is used to evanescently couple visible light (of wavelength from 632-637 nm from a tunable diode laser) into the LCE/ microgoblet resonator. The transmission spectrum (Fig. 5.16) collected from the coupled fiber reveals the typical WGM structures including fundamental as well as higher order resonator modes. The free spectral range ($\delta\lambda_{FSR}$), which is observed from the periodic repetition of the modal pattern, is 1.95 nm at a wavelength range around 635 nm. This is in a good agreement with the theoretically expected value of 1.90 nm for a 45 μm diameter PMMA-based microgoblet resonator. The Lorentzian fit to the resonance modes (as shown in the inset of Fig. 5.16) shows a Q-factor of about 2.14×10^4, which is in similar order of magnitude to the Q-factor achieved for dye-doped polymeric resonator without LCE (see chapter 4). This is not surprising as the WGMs are confined near the rim of the goblet resonator while the LCE is situated at the center.

5.2.3   Tuning of microgoblet lasing

Illumination of the LCE/PMMA goblet resonators with nanosecond laser pulses in the green spectral range has two impacts. On the one hand the LCE exhibits a
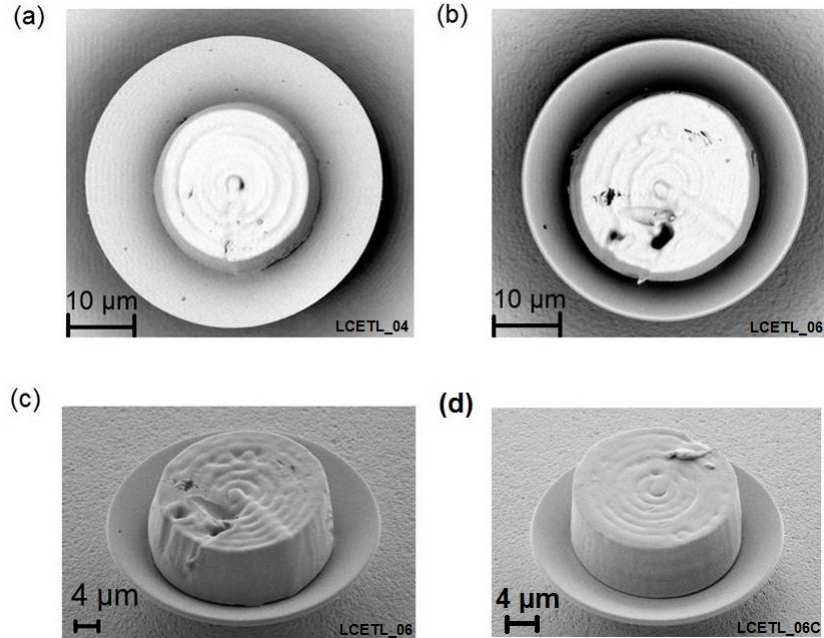
Figure 5.15: Scanning electron micrograph image of (a) LCE/microdisk resonator: a LCE micro-cylinder is centered on-top of a microdisk resonator. (b) The heat reflow process leads to surface-tension induced LCE/microgoblet resonator geometry and fuses the elastomer into the base of the resonator. The dark spots on the LCE microcylinder are defects resulting from the micro-tip handling. (c) and (d) Top-side view of LCE/goblet resonator.

pronounced photo-induced mechanical deformation. Hence the LCE microcylinder shows a radial expansion perpendicular to the alignment of the LCE molecules and a simultaneous contraction parallel to the cylinder axis (see Fig. 5.12). On the other hand, the PM 597 dye-doped polymeric cavity is excited and leading to lasing. The time scale for the thermal response of the LCE is long as compared to the temporal spacing of the pump nanosecond pulses. Hence the LCE /goblet laser system can be operated under controlled quasi-stationary conditions[5].

The LCE/PMMA microgoblet laser cavities were pumped with 10 ns pulses from a frequency-doubled Nd:YVO$_4$ laser at a pump wavelength of 532 nm and a repetition rate of 1 KHz. The pulse duration below 100 ns is essential to prevent triplet formation of the dye molecules, as discussed in chapter 4. The excitation pump

---

[5]The thermal response of LCE is occurred in the order of milliseconds, hence nanosecond pulses from the pump laser source (repetition rate in the order of KHz) cause the same effect as cw illumination.
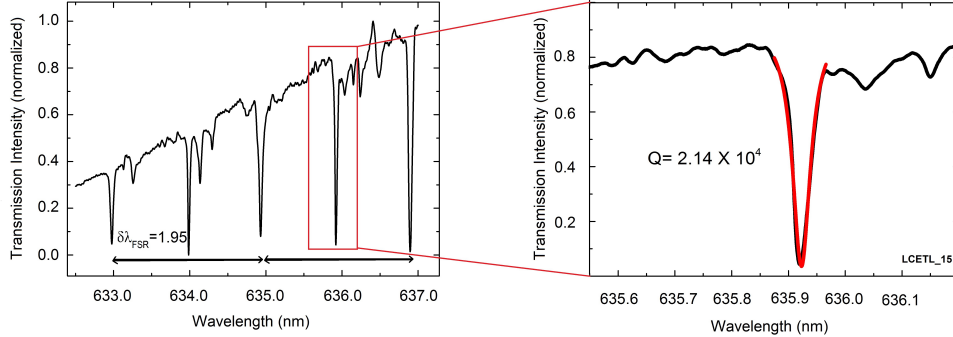
Figure 5.16: The transmission spectrum of an evanescently coupled tapered fiber shows WGM resonances with a free spectral range of $\delta\lambda_{FSR} = 1.95$ nm. LCE/goblet resonators retain a high-Q factor of 2.14×10^4 around 635.9 nm (right inset).

beam is focused in a free-space micro-photoluminescence (μ-PL) setup under an angle of 45° to a spot size of about 65 μm diameter to achieve nearly homogeneous excitation of the whole cavity. The spectrometer has a grating of 1200 lines/mm (resolution $\backsim$ 60 pm) equipped with a CCD (charge coupled device) camera. The setup also provides spatially resolved information about the emitted laser modes along the vertical diameter of the cavity utilizing the dimension of the CCD pixel array parallel to the alignment of the spectrometer entrance slit. The experimental setup is the same as the one shown in chapter 3.

The excitation energy density of the pump laser was varied using a Pockels cell along with a linear polariser. The output emission of the microcavity was then recorded as a function of the pump energy deposited on the cavity per pulse. A characteristic input-output curve of LCE/PMMA microgoblet dye laser is depicted in Fig. 5.17(a). The output intensity at certain pump energy was determined by integrating the intensity of a single lasing mode. The onset of lasing was inferred from the super-linear increase of the intensity resulting from the dominance of stimulated emission over spontaneous emission. The lasing threshold was found to be 0.15 μJ/pulse.

For pump energies well above the threshold, several narrow lasing peaks appear in the spectrum (Fig. 5.17(b)). The spectral distance between adjacent lasing peaks is below the free spectral range of the cavity (about 1.7 nm in the displayed wavelength range). This shows that besides the fundamental modes also several higher order cavity modes contribute to the lasing spectrum well above lasing threshold. By aligning the spectrometer entrance slit with the vertical diameter of the sample, as shown in Fig. 5.17(c) left, the emitted light along this direction can be spatially resolved. This measurement proves that the lasing modes are still confined near the
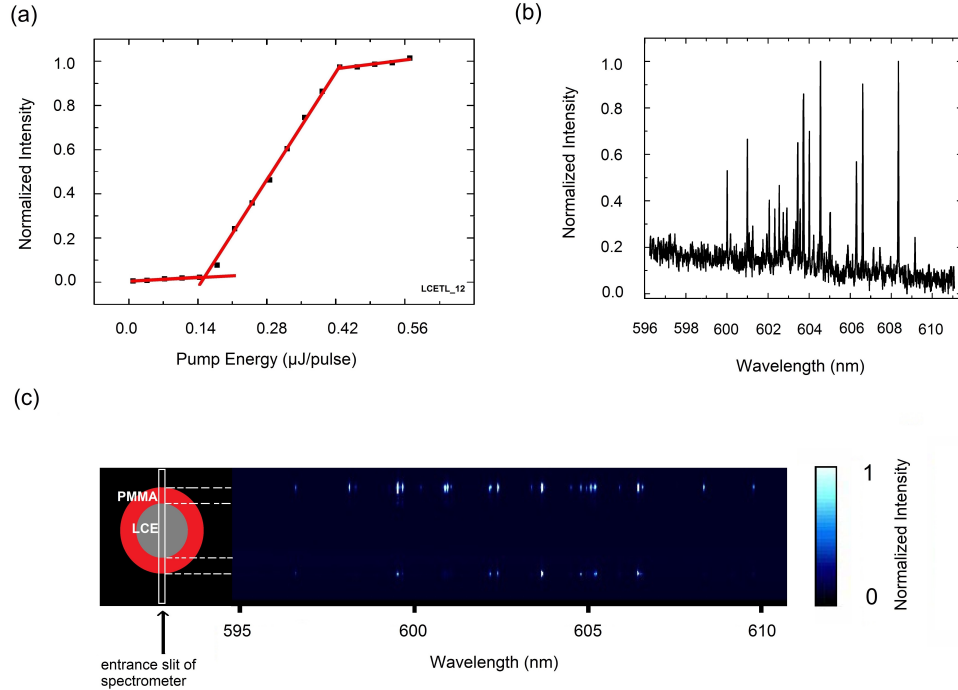
Figure 5.17: (a) Input-output curve of a PM 597 dye-doped LCE/PMMA goblet micro-laser showing a threshold energy of 0.15 μJ/pulse and a saturation above 0.42 μJ/pulse. (b) WGM laser emission from LCE/goblet resonator at pump energy of 0.28 μJ/pulse (well above the lasing threshold). (c) Image of LCE/goblet WGM lasing made by the CCD behind the spectrometer, which detects the spectrally resolved PL with a spatial resolution in the vertical direction (white rectangle). The measurement shows that the lasing modes are confined only to the rim of the resonator and the LCE cylinder has no impact on the modal structure of the PMMA goblet resonator

rim of the goblet resonator. Therefore the LCE microcylinder does not affect the modal structure of the cavity.

However, the response of the LCE to the optical pumping has significant influence on the spectral position of the cavity resonances. This is demonstrated by recording the modal spectrum for different excitation energies around the saturation level of the lasing (Fig. 5.18 (left)). It is found that a pronounced red shift of the lasing modes by more than 3 nm upon an increase of the deposited pump energy by about 0.8 μJ/pulse. This can be attributed to the shape deformation of the LCE microcylinder. Since the azo-dye is modified to efficiently absorb photons around 530 nm, the pump laser induces an increase in the local temperature of the elastomer. As a result the aligned molecular network of the LCE, which has been intentionally aligned along the
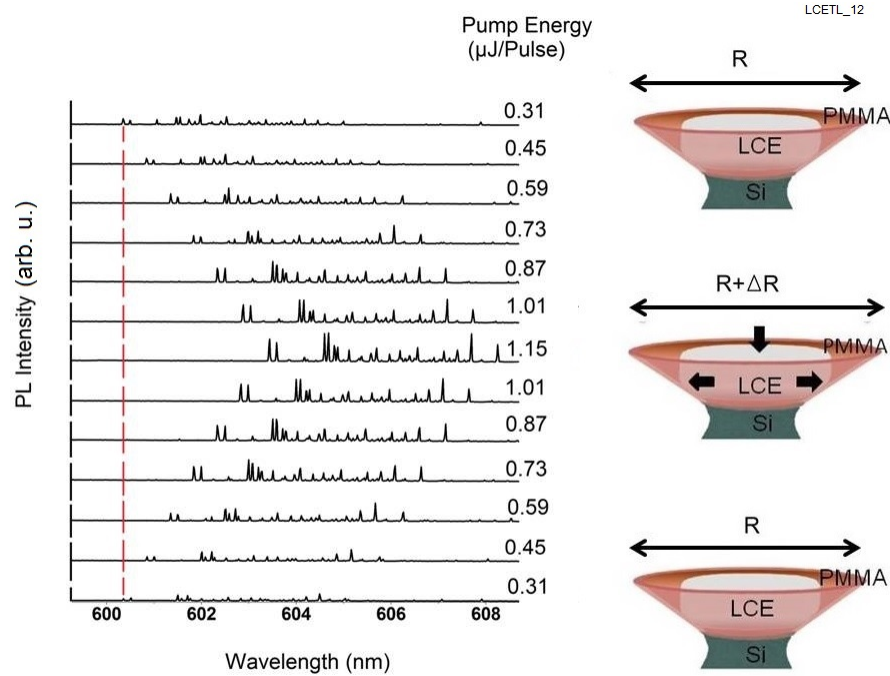
Figure 5.18: Left: Photo-induced tuning of LCE/goblet laser modes for different pump energies. Increasing the excitation energy from 0.31 μJ/pulse to 1.15 μJ/pulse leads to a red shift of the modes of about 3.1 nm. Decreasing the pump power from 1.15 μJ/pulse back to 0.31 μJ/pulse results in a reversed spectral shift (blue shift). Right: Schematic diagram of LCE/goblet resonators. Increasing the pump energy increases the disorder in the molecular network of the LCE microcylinder and leads to a symmetrical expansion of the LCE structure and the goblet resonator. Decreasing the pump power restores the ordered phase of the elastomer leading to a perfectly reversible resonator size deformation and tuning of the lasing modes.

axis of the cylinder, becomes disordered, evoking an in-plane symmetrical expansion of the microcylinder (see illustration in Fig. 5.18 (right)). This in turn leads to a symmetrical expansion of the goblet resonators and thus the red shift of the lasing modes. Imaging of the LCE/PMMA goblet resonator to a CCD camera under low repetition-rate pumping directly shows this photo-induced shape modification (see the video from [175]).

The photo-induced change in the shape of the LCE/PMMA goblets is found to be linear dependent on pump energy and perfectly reversible. As the pump energy is decreased, the decrease in the temperature of LCE microcylinder restores the nematic ordering of the LCE and the goblet shrinks back to its original size. The resulting reversal of the spectral shift is obvious in Fig. 5.18. The lasing modes

show red shift of about 0.51 nm for every increase in the excitation energy by 0.14 μJ/pulse. A decrease in the pump energy by the same amount leads to 100 % reversible spectral shift in the first two cycles. The red broken line in Fig. 5.18 shows the perfect reversibility of the first laser mode located at 600.35 nm at pump energy of 0.31 μJ/pulse. Further measurement in the excitation energy density cycles show the reversibility of the laser modes with fluctuations of the exact modal positions in the 0.1 nm range. Plotting the modal shifts as a function of deposited pump energy for the displayed cycle (Fig. 5.18) shows a perfect linear dependence with a slope of 3.64 nm/μJ. This corresponds to an expansion (contraction) of the radius of the cavity by nearly 27.3 nm for every 0.1 μJ increase (decrease) in input pump energy for the here discussed regime near the saturation level of the microlaser.

It is also demonstrated that the modification of the modal wavelengths of the polymeric cavity is not caused by heating of the cavity itself. In principle heat can cause a shift of the cavity modes due to the negative thermo-optic coefficient of PMMA. Thus the LCE microcylinders are replaced by negative photo-resist (IPL Nanoscribe GmbH) microcylinders of similar size doped with azo-dye (same concentration as in LCE mixture) and fabricated using 3D laser writing. It is found that no spectral shift of the cavity modes are observed while pumping in the energy-density range used for the photo-induced experiments. Therefore there is no direct heating of the PMMA cavity due to the pump laser and all the observed spectral shifts of LCE/goblet resonator modes is solely due to the photo-induced deformation of the LCE.

5.3   Summary and Conclusion

In this chapter a method for an optically controlled, stable and reversible tuning of whispering gallery modes in polymeric high-Q resonators over a large spectral range was shown.

For the photo-induced response of the cavity, nematic liquid crystal elastomers were used. Using a two photon absorption induced polymerization process (3D direct laser writing) uni-axially aligned LCE microcylinders were fabricated and placed on top-center of dye-doped PMMA microdisk resonators. A thermal reflow process led to smooth cavity surface, a goblet-type cavity geometry and integrated the LCE within the goblet basis. The integration technique maintained the modal structure and the high Q-factor of the resonators.

Upon optical pumping the symmetrical deformation of the LCE microcylinders led to expansion of the polymeric goblet resonators accompanied by a red shift of the

laser modes. Decreasing the pump power reverses the spectral shift. The spectral shift was linear in the change of the deposited pump energy and reproducible. The highly sturdy design of the structure allows realistic implementation on chip-devices. The demonstrated optical tuning opens a new interesting possibilities for all-optical control in circuits, enabling interaction between signal and control beams and the realization of self-tuning structures. Also photo-induced tunability of WGM resonators is highly desirable and paves a way for room temperature cavity quantum electrodynamics (c-QEDs) studies, where tuning of the cavity modes in and out of resonance with the emitter is required.

Chapter 6

Summary

This work demonstrated the fabrication and optical characterization of whispering gallery mode lasers and showed room temperature optical-control of the resonance modes of WGM cavities via photo-responsive smart materials for robust device applications.

Whispering gallery mode resonators with ultra high Q-factor reaching more than 10^7 were realized from PMMA-based polymeric cavities were fabricated via e-beam lithography. PMMA itself is a low-cost material allowing large scale production. The subsequent heat reflow process led to a a surface-tension induced smooth cavity geometry. This thermoplastic polymer has a low glass-transition temperature around 110 ℃ and makes the heat reflow process quite easy and creates significantly lower heat as compared to the reflow process used for silica [13]. This created a possibility for the integration of quantum emitters like colloidal quantum dots and laser dyes into polymeric microcavities.

For the development of low threshold quantum dot lasers and organic dye lasers the gain medium were integrated into the resonator without destroying the high-Q factor of the cavity. The emitters were integrated into the resonators via different techniques depending on the compatibility of the active medium with the polymer material.

For the incorporation of quantum dots into polymeric microresonators three different techniques were utilized: In quantum dot/polymer sandwiched resonator structures bare core CdTe QDs were integrated between PMMA layers and efficient coupling of QDs emission with the eigenmodes of the microcavity were observed. The PMMA layers shield the QDs from photo-oxidation. The integration mechanism did not require surface functionalization of the emitters and the cavity acquired a Q-factor of more than 10^4. The fluorescence measurement was conducted in a

micro-photoluminescence setup and the coupling of the cavity modes with the QDs were evidenced by the observation of periodic narrow peaks of WGMs on the bulk emission of the QDs (under cw excitation). Under pulsed excitation, by controlling the concentration of the emitters, the well known non-radiative Auger process (multi-particle process) were reduced and low threshold quantum dot lasers (with a threshold energy $\simeq 0.33\ \mu$J/pulse) were realized .

To further improve the optical properties of the QDs inorganic/organic polymer hybrid CdSe/CdS/PMMA QDs were used. These quantum emitters were colloidal CdSe/CdS QDs and were embedded into methyl methacrylat (MMA) polymer particles via a mini-emulsion polymerization process. Besides the polymer preventing the emitters from photo-oxidation and increasing its photostability, the compatibility between the polymer matrix and the encapsulated emitter opened a room for doping the QDs into the host matrix before processing the cavities. Resonators doped with CdSe/CdS/PMMA QDs showed also low threshold lasing (with a threshold energy $\simeq 0.36\ \mu$J/pulse).

Since WGMs are confined on the rim of the resonators a highly localized deposition of the emitters on the rim of the resonators was also realized via dip-pen nanolithography technique (nanopatterning), which is a scanning probe lithography technique. It uses the tip of an atomic force microscope (AFM-probe) to pattern surfaces with a variety of QD/inks. This highly localized deposition technique maintained the high Q-factor of the resonators (more than 10^4 were obtained). Free-space excitation of nanopatterned samples in a micro-photoluminescence setup showed low threshold microlasing ($\simeq 0.56\ \mu$J/pulse) in the fundamental mode of the cavity. Finite element simulations showed that only the lower order modes of the cavity were involved in lasing.

Due to their near-unity high quantum yield, low self-aggregation and their compatibility with the polymer matrix, the dye Pyrromethene 597 dye (π-conjugated organic molecules) was also used. This laser dye is soluble in PMMA solvents like anisole. Hence, additional solvents before mixing them to PMMA was not required and the dye was directly dissolved in the photoresist before processing of the cavities. Resonators doped with the Pyrromethene 597-dye acquired a Q-factor of more than 10^4. By controlling the concentration and pumping with nanosecond pulses (to prevent the triplet state formation in the dye molecules) low-threshold microlasers (threshold energy $\simeq 0.54$ nJ/pulse) were achieved.

To further improve the polymer resonators for outstanding optical properties, room temperature resonance mode control and tuning of the lasing modes, on scales compatible with on-chip integration, was introduced. This tunability was achieved by the integration of photo-responsive liquid crystalline elastomers (LCEs) into mi-

crogoblet resonators. The LCEs were fabricated via the two photon absorption induced polymerization process of direct laser writing. The integration mechanism maintained the high-Q of the resonator. The optical response of the elastomer allowed a controlled reshaping of the goblet by employing low pump power, leading to a fully reversible tuning of the modes. These optical devices can be realistically implemented in on-chip devices and pave a way for all-optical control in circuits, enabling interaction between signal and control beams and the realization of self-tuning structures. Especially in room temperature cavity quantum electrodynamics studies, the tuning of the cavity modes in and out of resonance with the emitter modes can be monitored via the presented photo-induced deformation mechanism of the LCE/goblet resonator geometry.

Publications and Contributions

Published Papers

1. **Strongly confining bare core CdTe quantum dots in polymeric microresonators**, Assegid Mengistu Flatae, Tobias Grossmann, Torsten Beck, Sarah Wiegele, and Heinz Kalt, *APL Materials* **2**, 012107, 2014.

2. **Optically controlled elastic microcavities**, Assegid Mengistu Flatae, Matteo Burresi, Hao Zeng, Sara Nocentini, Sarah Wiegele, Camilla Parmeggiani, Heinz Kalt, and Diederik Wiersma, *submitted to Light: Science and Applications* (29.08.2014).

3. **Quantum dot microlasers : Highly localized deposition of emitters using dip-pen nanolithography technique**, Assegid Mengistu Flatae, Sylwia Sekula-Neuner, Michael Hirtz, Thomas Laue, Sarah Wiegele, Fabian Ruf, Tobias Siegle, Harald Fuchs, and Heinz Kalt, *Manuscript under preparation* (2014).

4. **Opto-mechanically tunable polymeric microlasers**, Assegid Mengistu Flatae, Matteo Burresi, Hao Zeng, Sara Nocentini, Sarah Wiegele, Diederik Wiersma, and Heinz Kalt, *QELS -Fundamental Science San Jose, California, United States*, http://dx.doi.org/10.1364/CLEO-AT.2014.JW2A.58, 2014.

Contributions to conferences and invited talks

1. **Quantum dot on-chip lasers**, Assegid Mengistu Flatae, *Karlsruhe school of optics and photonics, Karlsruhe, Germany, 2014, PhD-seminar*, <u>invited talk</u>.

2. **Whispering gallery mode resonators**, Assegid Mengistu Flatae, *Institute of Applied Physics, Karlsruhe institute of technology, Karlsruhe, Germany, 2014*, <u>invited talk</u>.

3. **Opto-mechanically controlled tunable microlasers**, Assegid Mengistu Flatae, Matteo Burresi, Hao Zeng, Sara Nocentini, Sarah Wiegele, Diederik Wiersma, and Heinz Kalt, *CLEO 2014, Laser science to photonics applications. San Jose, California, USA, 2014.*

4. **Photo-induced reversibly tuned microlasers on a silicon chip**, Assegid Mengistu Flatae, *Karlsruhe school of optics and Photonics (KSOP) summer school on photonics, Bad Herrenalb, Germany, 2014.*

5. **Photo-induced tuning of polymeric photonic structures**, Sara Nocentini, Matteo Burresi, Assegid Mengistu Flatae, Hao Zeng, Sarah Wiegele, Hainz Kalt, and Diederik Wiersma, *The 11th international symposium on photonic and electromagnetic crystal structures. PECS-XI-Shanghai, China, 2014.*

6. **Photo-induced tuning of polymeric microlasers using liquid crystalline elastomers**, Assegid Mengistu Flatae, Matteo Burresi, Hao Zeng, Sara Nocentini, Sarah Wiegele, Camilla Parmeggiani, Heinz Kalt, and Diederik Wiersma, *Fotonica 2014 - Convegno Italiano delle Tecnologie Fotoniche, 16a edizione Fotonica, Napoli, Italy, 2014.*

7. **Photo-induced tuning of polymeric cavities using liquid crystalline elastomers**, Assegid Mengistu Flatae, Matteo Burresi, Hao Zeng, Sara Nocentini, Sarah Wiegele, Diederik Wiersma, and Heinz Kalt, *PLMCN2014 conference, Physics of light matter coupling in nanostructures, Montpellier, France, June 2014.*

8. **Quantum emitters in polymeric microresonators**, Assegid Mengistu Flatae, *Europhotonics 3rd spring school porquerolles, France, 2014* <u>invited talk</u>.

9. **Polymeric microresonators**, Assegid Mengistu Flatae, *European Laboratory for Non-Linear Spectroscopy (LENS) Florence, Italy, 2013,* <u>invited talk</u>.

10. **Quantum dots in whispering gallery mode resonators**, Assegid Mengistu Flatae, Felix Büchle, Tobias Grossmann, Torsten Beck, and Heinz Kalt, *Optics of excitons in confined system, OECS 13, Rome, Italy, 2013.*

11. **Quantum emitters in whispering gallery mode resonators**, Assegid Mengistu Flatae, *Physics department at the University of Stuttgart, Stuttgart, Germany, 2013,* <u>invited talk</u>.

12. **Polymeric photonic-molecule lasers**, Tobias Grossmann, Tobias Wienhold, Uwe Bog, Thorsten Beck, Assegid Mengistu Flatae, Sarah Wiegele, Timo

Mappes, and Heinz Kalt, *14th conference on physics of light-matter coupling in nanostructures, PCLMN, 14 Hersonissos, Greece, 2013.*

13. **Quantum emitters in whispering gallery mode resonators**, Assegid Mengistu Flatae, Tobias Grossmann, Torsten Beck, and Heinz Kalt, *DPG-Regensburg, Germany, 2013.*

14. **Quantum dots in polymeric microresonators**, Assegid Mengistu Flatae, Tobias Grossmann, Torsten Beck, Sarah Wiegele, and Heinz Kalt, *Europhotonics 2nd spring school, Pforzheim, Germany, 2013.*

15. **Quantum dots in polymeric microdisk/goblet resonators**, Assegid Mengistu Flatae, Tobias Grossmann, Torsten Beck, and Heinz Kalt, *CFN summer school on nanophotonics, Bad Herrenalb, Germany, 2012.*

16. **Coupled high-Q microresonators**, Assegid Mengistu Flatae, Tobias Grossmann, Torsten Beck, and Heinz Kalt, *Europhotonics 1st spring school. ICFO, Barcelona, Spain, 2012.*

17. **High-Q polymeric microcavities towards biosensing applications**, Torsten Beck, Sasika Becker, Tobias Grossmann, Patrik Rath, Assegid Mengistu Flatae, and Hainz Kalt, *DPG-Berlin, Germany, 2012.*

References

[1] B. Min, S. Kim, K. Okamoto, L. Yang, A. Scherer, H. Atwater, and K. Vahala, "Ultralow threshold on-chip microcavity nanocrystal quantum dot lasers," Applied Physics Letters **89**, 191124 (2006).

[2] J. V. Hryniewicz, P. P. Absil, B. E. Little, and R. A. Wilson, "Higher order filter response in coupled microring resonators," IEEE photonics technology letters **12**, 320–322 (2000).

[3] V. S. Ilchenko, A. A. Savchenkov, A. B. Matsko, and L. Maleki, "Whispering-gallery-mode electro-optic modulator and photonic microwave receiver," J. Opt. Soc. Am. B **20**, 333–342 (2003).

[4] F. Vollmer and S. Arnold, "Whispering-gallery-mode biosensing: label-free detection down to single molecules." Nature methods **5**, 591–596 (2008).

[5] K. J. Vahala, "Optical microcavities." Nature **424**, 839–46 (2003).

[6] T. Kippenberg, A. Tchebotareva, J. Kalkman, A. Polman, and K. Vahala, "Purcell-factor-enhanced scattering from Si nanocrystals in an optical microcavity," Physical Review Letters **103**, 1–4 (2009).

[7] R.-M. Ma, R. F. Oulton, V. J. Sorger, G. Bartal, and X. Zhang, "Room-temperature sub-diffraction-limited plasmon laser by total internal reflection." Nature materials **10**, 110–113 (2011).

[8] M. Metcalfe, A. Muller, G. S. Solomon, and J. Lawall, "Active feedback of a Fabry â Perot cavity to the emission of a single InAs / GaAs quantum dot," J. Opt. Soc. Am. B/ **26**, 2308–2314 (2009).

[9] I. D. W. Samuel and G. a. Turnbull, "Organic semiconductor lasers." Chemical reviews **107**, 1272–1295 (2007).

References

[10] T. Grossmann, M. Hauser, T. Beck, C. Gohn-Kreuz, M. Karl, H. Kalt, C. Vannahme, and T. Mappes, "High-Q conical polymeric microcavities," Applied Physics Letters **96**, 1–3 (2010).

[11] M. L. Gorodetsky, a. a. Savchenkov, and V. S. Ilchenko, "Ultimate Q of optical microsphere resonators." Optics letters **21**, 453–455 (1996).

[12] M. L. Gorodetsky and V. S. Ilchenko, "Optical microsphere resonators : optimal coupling to high- Q whispering-gallery modes," J. Opt. Soc. Am. B **16**, 147–154 (1999).

[13] T. J. Kippenberg, S. M. Spillane, D. K. Armani, B. Min, L. Yang, and K. J. Vahala, "Fabrication, coupling and nonlinear optics of ultra- high-q microsphere and chip-based toroid microcavities," in "Advanced series in Applied Physics," , vol. 5 (World scientific, 2004), chap. 5, pp. 1–65.

[14] T. Grossmann, S. Klinkhammer, M. Hauser, D. Floess, T. Beck, C. Vannahme, T. Mappes, U. Lemmer, and H. Kalt, "Strongly confined, low-threshold laser modes in organic semiconductor microgoblets." Optics express **19**, 10009–10016 (2011).

[15] A. Flatae, T. Grossmann, T. Beck, S. Wiegele, and H. Kalt, "Strongly confining bare core CdTe quantum dots in polymeric microdisk resonators," APL Materials **2**, 1–7 (2014).

[16] T. Beck, M. Mai, T. Grossmann, T. Wienhold, M. Hauser, T. Mappes, and H. Kalt, "High-Q polymer resonators with spatially controlled photofunctionalization for biosensing applications," Applied Physics Letters **102**, 1–3 (2013).

[17] T. Grossmann, T. Wienhold, U. Bog, T. Beck, C. Friedmann, H. Kalt, and T. Mappes, "Polymeric photonic molecule super-mode lasers on silicon," Light: Science & Applications **2**, e82 (2013).

[18] E. Yariv, S. Schultheiss, T. Saraidarov, and R. Reisfeld, "Effciency and photostability of dye-doped solid-state lasers in di Â erent hosts," Optical materials **16**, 29–38 (2001).

[19] T. Grossmann, "Whispering-gallery-mode lasing in polymeric microcavities," Phd dissertation, Karlsruhe Institute of Technology (2012).

[20] D. K. Vandyshev, Y. V. ; Dneprovskii, V. S. ; Klimov, V. I. and Okorokov, "Lasing on a transition between quantum-well levels in a quantum dot." JETP Lett. **54**, 442–445 (1991).

[21] J. Schafer, J. P. Mondia, R. Sharma, Z. H. Lu, a. S. Susha, a. L. Rogach, and L. J. Wang, "Quantum dot microdrop laser," Nano Letters **8**, 1709–1712 (2008).

[22] R. Sharma, "Electrodynamically confined microscale lasers," Phd dissertation, Friedrich-Alexander-UniversitÂ¨at Erlangen-NÂ¨urnberg (2009).

[23] D. J. F. Rakovich Y P , Yang L, McCabe E M, G. N. Perova T, Moore A, and R. A, "Whispering gallery mode emission from a composite system of CdTe nanocrystals and a spherical microcavity," Semicond. Sci. Techno **18**, 914– 918 (2003).

[24] V. I. Klimov, "Optical gain and stimulated emission in nanocrystal Quantum Dots," Science **290**, 314–317 (2000).

[25] Q. Chang, S. Member, Q. Li, and Z. Zhang, "A Tunable broadband photonic RF phase shifter based on a silicon microring resonator," IEEE photonics technology letters **21**, 60–62 (2009).

[26] H. C. Tapalian, J. Laine, and P. A. Lane, "Thermooptical switches using coated microsphere resonators," IEEE photonics technology letters **14**, 1118–1120 (2002).

[27] A. Majki, M. Koechlin, G. Poberaj, and P. Günter, "Optical microring resonators in fluorine- implanted lithium niobate," Optics Express **16**, 8769–8779 (2008).

[28] K. Srinivasan and O. Painter, "Optical fiber taper coupling and high-resolution wavelength tuning of microdisk resonators at cryogenic temperatures," Applied Physics Letters **90**, 031114 (2007).

[29] S. K. Y. Tang, R. Derda, Q. Quan, M. Lončar, and G. M. Whitesides, "Continuously tunable microdroplet-laser in a microfluidic channel." Optics express **19**, 2204–15 (2011).

[30] M. Saito, H. Shimatani, and H. Naruhashi, "Tunable whispering gallery mode emission from a microdroplet in elastomer." Optics express **16**, 11915–11919 (2008).

[31] V. D. Ta, R. Chen, and H. D. Sun, "Tuning whispering gallery mode lasing from self-assembled polymer droplets." Scientific reports **3**, 1362 (2013).

[32] M. Saito and K. Koyama, "Deformable microdroplet cavity fabricated by an inkjet method," Japanese Journal of Applied Physics **49**, 1–4 (2010).

References

[33] C.-T. Wang, C.-W. Tseng, J.-H. Yu, Y.-C. Li, C.-H. Lee, H.-C. Jau, M.-C. Lee, Y.-J. Chen, and T.-H. Lin, "Optical bistability in a silicon nitride microring resonator with azo dye-doped liquid crystal as cladding material." Optics express **21**, 10989–10994 (2013).

[34] M. Humar, M. Ravnik, S. Pajk, and I. Muševič, "Electrically tunable liquid crystal optical microresonators," Nature Photonics **3**, 595–600 (2009).

[35] K. a. Piegdon, S. Declair, J. Foerstner, T. Meier, H. Matthias, M. Urbanski, H.-S. Kitzerow, D. Reuter, A. D. Wieck, A. Lorke, and C. Meier, "Tuning quantum-dot based photonic devices with liquid crystals." Optics express **18**, 7946–7954 (2010).

[36] L. Rayleigh, "The problem of the whispering gallery," Philos. Mag **20**, 1001–1004 (1910).

[37] S. Papers, "Farther application's of Bessel's," Philos. Mag. **1123**, 100–109 (1913).

[38] A. N. Oraevsky, "Whispering-gallery waves," Quantum Electronics **377**, 377–400 (2002).

[39] R. D. Richtmyer, "Dielectric resonators," Journal of Applied Physics **10**, 391–398 (1939).

[40] D. K. Armani, T. J. Kippenberg, S. M. Spillane, and K. J. Vahala, "Ultra-high-Q toroid microcavity on a chip." Nature **421**, 925–928 (2003).

[41] S. M. Spillane, T. J. Kippenberg, and K. J. Vahala, "Ultrahigh- Q toroidal microresonators for cavity quantum electrodynamics," Physical Review A **71**, 1–10 (2005).

[42] C. Garrett, W. Kaiser, and W. Bond, "Stimulated emission into optical whispering modes of spheres," Physical Review **124**, 1807–1809 (1961).

[43] Y. Panitchob, G. S. Murugan, M. N. Zervas, P. Horak, S. Berneschi, S. Pelli, G. Nunzi Conti, and J. S. Wilkinson, "Whispering gallery mode spectra of channel waveguide coupled microspheres." Optics express **16**, 11066–11076 (2008).

[44] A. Ashkin and J. M. Dziedzic, "Observation of optical resonances of dielectric spheres by light scattering." Applied Optics **20**, 1803–1814 (1981).

[45] M. Borselli, T. Johnson, and O. Painter, "Beyond the Rayleigh scattering limit in high-Q silicon microdisks: theory and experiment." Optics express **13**, 1515–1530 (2005).

[46] M. Soltani, S. Yegnanarayanan, and A. Adibi, "Ultra-high Q planar silicon microdisk resonators for chip-scale silicon photonics." Optics express **15**, 4694–4704 (2007).

[47] H. Lee, T. Chen, J. Li, K. Y. Yang, S. Jeon, O. Painter, and K. J. Vahala, "Chemically etched ultrahigh-Q wedge-resonator on a silicon chip," Nature Photonics **6**, 369–373 (2012).

[48] X. Fan, I. M. White, S. I. Shopova, H. Zhu, J. D. Suter, and Y. Sun, "Sensitive optical biosensors for unlabeled targets: a review." Analytica chimica acta **620**, 8–26 (2008).

[49] X. Fan and I. M. White, "Optofluidic Microsystems for Chemical and Biological Analysis." Nature photonics **5**, 591–597 (2011).

[50] M. Hauser, "Mikroresonatoren aus Glas und Polymeren als optische Flüstergalerien," Dissertation, Karlsruhe Institute of Technology (2011).

[51] H. Fan, S. Hua, X. Jiang, and M. Xiao, "Demonstration of an erbium-doped microsphere laser on a silicon chip," Laser Physics Letters **10**, 1–4 (2013).

[52] J. D. Jackson, *Classical Electrodynamics* (Berkeley, California, 2002), 3rd ed.

[53] A. Yariv, *Optical electronics* (Saunders College Publishing, 1991), 4th ed.

[54] B. E. Little and S. T. Chu, "Estimating surface-roughness loss and output coupling in microdisk resonators." Optics letters **21**, 1390–1392 (1996).

[55] I. Agha, J. Sharping, M. Foster, and a.L. Gaeta, "Optimal sizes of silica microspheres for linear and nonlinear optical interactions," Applied Physics B **83**, 303–309 (2006).

[56] Y. Ido, Y. Masumoto, F. Sasaki, M. Mori, S. Haraichi, and S. Hotta, "Reduced Lasing Threshold in Thiophene/Phenylene Co-Oligomer Crystalline Microdisks," Applied Physics Express **3**, 1–3 (2010).

[57] B. S. Teich and M.C., *Fundamental of Photonics* (2007), 2nd ed.

[58] S. L. McCall, a. F. J. Levi, R. E. Slusher, S. J. Pearton, and R. a. Logan, "Whispering-gallery mode microdisk lasers," Applied Physics Letters **60**, 289 (1992).

References

[59] S. V. Boriskina, "Theoretical prediction of a dramatic Q-factor enhancement and degeneracy removal of whispering gallery modes in symmetrical photonic molecules." Optics letters **31**, 338–340 (2006).

[60] T. Grossmann, S. Schleede, M. Hauser, T. Beck, M. Thiel, G. von Freymann, T. Mappes, and H. Kalt, "Direct laser writing for active and passive high-Q polymer microdisks on silicon." Optics express **19**, 11451–11456 (2011).

[61] J.E.Mark, *Polymer data handbook* (Oxford University Press, Inc., 1999).

[62] Y. Okada and Y. Tokumaru, "Precise determination of lattice parameter and thermal expansion coefficient of silicon between 300 and 1500 K," Journal of Applied Physics **56**, 314–320 (1984).

[63] S. Spillane, T. Kippenberg, O. Painter, and K. Vahala, "Ideality in a fiber-taper-coupled microresonator system for application to cavity quantum electrodynamics," Physical Review Letters **91**, 1–4 (2003).

[64] A. Yariv, "universal," Electronic Letters **36**, 1–2 (2000).

[65] H. A. Haus, *Wave and fields in optoelectronics* (Prentice-Hall, 1984).

[66] T. Beck, "Polymer-Mikroresonatoren hoher Gute als optische Sensoren," Ph.D. thesis, Karlsruhe Institute of Technology (2013).

[67] T. Jan and A. Kippenberg, "Nonlinear optics in ultra-high-Q whispering-gallery optical microcavities," Ph.D. thesis, California Institute of Technology, Pasadena, Califirnia (2004).

[68] N. Holonyak, R. M. Kolbas, R. D. Dupuis, and P. D. Dapkus, "Room-temperature continuous operation of photopumped MO-CVD AlxGa1âxAs-GaAs-AlxGa1âxAs quantum-well lasers," Applied Physics Letters **33**, 73–75 (1978).

[69] H. Arakawa, Y. , Sakaki, "Multidimensional quantum well laser and temperature dependence of its threshold current," Applied Physics Letters **40**, 939–941 (1982).

[70] M. A. Kastner, "The single-electron transistor," Reviews of Modern Physics, **64**, 849–851 (1992).

[71] C. B. Murray, D. J. Noms, and M. G. Bawendi, "Synthesis and characterization of nearly monodisperse CdE (E=S, Se, Te) semiconductor nanocrystallites," J. Am. Chem. Soc. **115**, 8706–8715 (1993).

[72] A. P. Tolbert, Sarah H. and Alivisatos, "Hgh-pressure structural transformations in semiconductor nanocrystals," Annu. Rev. Phys. Chern. **46**, 595–625 (1995).

[73] A. N. Goldstein, C. M. Echer, A. P. Alivisatos, N. Series, and N. Jun, "Melting in semiconductor nanocrystals," Science, New Series, **256**, 1425–1427 (1992).

[74] M. R. J. Jortner, M. Ratner, *Molecular electronics (IUPAC Chemistry for the 21st Century)* (Blackwell Science, 1997).

[75] J. Schafer, "Lasing from nanocrystal quantum dots in levitated microdrops at low concentrations," Phd dissertation, Max Planck Forschungsgruppe, Universität Erlangen-Nürnberg (2009).

[76] R. Geick, "Lattice vibrational properties of hexagonal CdSe," Journal of Applied Physics **37**, 1994–1997 (1966).

[77] W. Nolting, *Grundkurs Theoretische Physik 5/2: Quantenmechanik - Methoden und Anwendungen* (Springer, Berlin, 2002).

[78] L. E. Brus, "Electron-electron and electron-hole interactions in small semiconductor crystallites: The size dependence of the lowest excited electronic state," The Journal of Chemical Physics **80**, 4403–4409 (1984).

[79] U. Roessler, "Energy bands of hexagonal II-VI semiconductors," Physical Review **184**, 733–738 (1969).

[80] T. Takagahara, "Effects of dielectric confinement and electron-hole exchange interaction on excitonic states in semiconductor quantum dots." Physical review. B, Condensed matter **47**, 4569–4584 (1993).

[81] D. Norris, A. Efros, M. Rosen, and M. Bawendi, "Size dependence of exciton fine structure in CdSe quantum dots," Physical Review B **53**, 16347–16354 (1996).

[82] S. a. Crooker, T. Barrick, J. a. Hollingsworth, and V. I. Klimov, "Multiple temperature regimes of radiative decay in CdSe nanocrystal quantum dots: Intrinsic limits to the dark-exciton lifetime," Applied Physics Letters **82**, 2793–2795 (2003).

[83] V. I. Klimov, "Charge carrier dynamics and optical gain in nanocrystal quantum dots : From fundamental photophysics to quantum dot lasing," (Marcel Dekker, Inc., Los Alamos National Laboratory, Los Alamos, New Mexico, U.S.A., 2004), chap. 5, pp. 174–229.

[84] A. a. Mikhailovsky, A. V. Malko, J. a. Hollingsworth, M. G. Bawendi, and V. I. Klimov, "Multiparticle interactions and stimulated emission in chemically synthesized quantum dots," Applied Physics Letters **80**, 2380 (2002).

[85] V. I. Klimov, A. A. Mikhailovsky, D. W. Mcbranch, C. A. Leatherdale, and M. G. Bawendi, "Quantization of multiparticle Auger rates in semiconductor quantum dots," Science **287**, 1011–1013 (2000).

[86] A. a. Mikhailovsky, S. Xu, and V. I. Klimov, "Femtosecond intraband modulation spectroscopy," Review of Scientific Instruments **73**, 136 (2002).

[87] S. Xu, A. Mikhailovsky, J. Hollingsworth, and V. Klimov, "Hole intraband relaxation in strongly confined quantum dots: Revisiting the âphonon bottleneckâ problem," Physical Review B **65**, 1–5 (2002).

[88] V. Klimov, D. McBranch, C. Leatherdale, and M. Bawendi, "Electron and hole relaxation pathways in semiconductor quantum dots," Physical Review B **60**, 13740–13749 (1999).

[89] a. V. Malko, a. a. Mikhailovsky, M. a. Petruska, J. a. Hollingsworth, and V. I. Klimov, "Interplay between optical gain and photoinduced absorption in CdSe nanocrystals," The Journal of Physical Chemistry B **108**, 5250–5255 (2004).

[90] L.-W. Wang, M. Califano, A. Zunger, and A. Franceschetti, "Pseudopotential theory of Auger processes in CdSe quantum dots," Physical Review Letters **91**, 1–4 (2003).

[91] X. Brokmann, G. Messin, P. Desbiolles, E. Giacobino, M. Dahan, and J. P. Hermier, "Colloidal CdSe/ZnS quantum dots as single-photon sources," New Journal of Physics **6**, 1–9 (2004).

[92] V. Esch, B. Fluegel, G. Khitrova, H. Gibbs, K. Kang, S. Koch, L. Liu, S. Risbud, and N. Peyghambarian, "State filling, Coulomb, and trapping effects in the optical nonlinearity of CdTe quantum dots in glass," Physical Review B **42**, 7450–7453 (1990).

[93] A. Y. Nazzal, X. Wang, L. Qu, W. Yu, Y. Wang, X. Peng, and M. Xiao, "Environmental effects on photoluminescence of highly luminescent CdSe and CdSe/ZnS core/shell nanocrystals in polymer thin films," The Journal of Physical Chemistry B **108**, 5507–5515 (2004).

[94] W. G. J. H. M. van Sark, P. L. T. M. Frederix, A. a. Bol, H. C. Gerritsen, and A. Meijerink, "Blueing, Bleaching, and Blinking of Single CdSe/ZnS Quantum Dots," ChemPhysChem **3**, 871–879 (2002).

[95] Y. Zhao, C. Riemersma, F. Pietra, R. Koole, C. de Mello Donegá, and A. Meijerink, "High-temperature luminescence quenching of colloidal quantum dots," ACS Nano **6**, 9058–9067 (2012).

[96] M. Kuno, D. Fromm, S. Johnson, A. Gallagher, and D. Nesbitt, "Modeling distributed kinetics in isolated semiconductor quantum dots," Physical Review B **67**, 1–15 (2003).

[97] A. Efros and M. Rosen, "Random telegraph signal in the photoluminescence intensity of a single quantum dot," Physical Review Letters **78**, 1110–1113 (1997).

[98] R. M. Waxler, D. Horowitz, and A. Feldman, "Optical and physical parameters of Plexiglas 55 and Lexan," Applied Optics **18**, 101–104 (1979).

[99] C. Negele, J. Haase, A. Budweg, A. Leitenstorfer, and S. Mecking, "Stable single-photon emission by quantum dot/polymer hybrid particles." Macromolecular rapid communications **34**, 1145–1150 (2013).

[100] M. a. Hines and P. Guyot-Sionnest, "Synthesis and characterization of strongly luminescing ZnS-capped CdSe nanocrystals," The Journal of Physical Chemistry **100**, 468–471 (1996).

[101] F. Dubois, B. Mahler, B. Dubertret, E. Doris, and C. Mioskowski, "A Versatile strategy for quantum dot ligand exchange," Journal of the American Chemical Society **129**, 482–483 (2007).

[102] A. C. Wisher, I. Bronstein, and V. Chechik, "Thiolated PAMAM dendrimercoated CdSe/ZnSe nanoparticles as protein transfection agents," Chemical Communications pp. 1637–1639 (2006).

[103] S. T. Selvan, T. T. Tan, and J. Y. Ying, "Robust, non-Cytotoxic, Silica-coated CdSe quantum dots with efficient photoluminescence," Advanced Materials **17**, 1620–1625 (2005).

[104] Y. Gao, S. Reischmann, J. Huber, T. Hanke, R. Bratschitsch, A. Leitenstorfer, and S. Mecking, "Encapsulating of single quantum dots into polymer particles," Colloid and Polymer Science **286**, 1329–1334 (2008).

[105] R. D. Piner, ""Dip-Pen" Nanolithography," Science **283**, 661–663 (1999).

[106] L. Huang, A. B. Braunschweig, W. Shim, L. Qin, J. K. Lim, S. J. Hurst, F. Huo, C. Xue, J.-W. Jang, and C. a. Mirkin, "Matrix-assisted dip-pen nanolithography and polymer pen lithography." Small **6**, 1077–1081 (2010).

References

[107] R. Guo, Y. Yu, Z. Xie, X. Liu, X. Zhou, Y. Gao, Z. Liu, F. Zhou, Y. Yang, and Z. Zheng, "Matrix-assisted catalytic printing for the fabrication of multiscale, flexible, foldable, and stretchable metal conductors." Advanced materials **25**, 3343–3350 (2013).

[108] M. Hirtz, A. M. Greiner, T. Landmann, M. Bastmeyer, and H. Fuchs, "Click-Chemistry Based Multi-Component Microarrays by Quill-Like Pens," Advanced Materials Interfaces **1**, 1–7 (2014).

[109] M. Hirtz, R. Corso, S. Sekula-Neuner, and H. Fuchs, "Comparative height measurements of dip-pen nanolithography-produced lipid membrane stacks with atomic force, fluorescence, and surface-enhanced ellipsometric contrast microscopy." Langmuir : the ACS journal of surfaces and colloids **27**, 11605–11608 (2011).

[110] S. Sekula, J. Fuchs, S. Weg-Remers, P. Nagel, S. Schuppler, J. Fragala, N. Theilacker, M. Franzreb, C. Wingren, P. Ellmark, C. A. K. Borrebaeck, C. A. Mirkin, H. Fuchs, and S. Lenhert, "Multiplexed lipid dip-pen nanolithography on subcellular scales for the templating of functional proteins and cell culture." Small **4**, 1785–1793 (2008).

[111] S. Sekula-Neuner, J. Maier, E. Oppong, A. C. B. Cato, M. Hirtz, and H. Fuchs, "Allergen arrays for antibody screening and immune cell activation profiling generated by parallel lipid dip-pen nanolithography." Small (Weinheim an der Bergstrasse, Germany) **8**, 585–591 (2012).

[112] S. Lenhert, F. Brinkmann, T. Laue, S. Walheim, C. Vannahme, S. Klinkhammer, M. Xu, S. Sekula, T. Mappes, T. Schimmel, and H. Fuchs, "Lipid multilayer gratings." Nature nanotechnology **5**, 275–279 (2010).

[113] K. Mitsakakis, S. Sekula-Neuner, S. Lenhert, H. Fuchs, and E. Gizeli, "Convergence of dip-pen nanolithography and acoustic biosensors towards a rapid-analysis multi-sample microsystem." Analyst **137**, 3076–82 (2012).

[114] M. Hirtz, A. Oikonomou, T. Georgiou, H. Fuchs, and A. Vijayaraghavan, "Multiplexed biomimetic lipid membranes on graphene by dip-pen nanolithography." Nature communications **4**, 1–8 (2013).

[115] S. Forget and S. Chénais, *Organic solid-state lasers*, vol. 175 of *Springer Series in Optical Sciences* (Springer Berlin Heidelberg, Berlin, Heidelberg, 2013).

[116] I. D. W. Ribierre, J. C. ; Tsiminis G.; Richardson, S., Turnbull, G. A.; and Samuel, "Amplified spontaneous emission and lasing properties of bisfluorene-cored dendrimers," Applied Physics Letters **91**, 1–3 (2007).

[117] G. Ishow, E., Brosseau, B., Clavier, P. Nakatani, K., Tauc, S. Fiorini-Debuisschert, CeÂ´line , Neveu, and A. Sandre, O., and LeÂ´austic, "Multicolor emission of small molecule-based amorphous thin films and nanoparticles with a single excitation wavelength," Chem. Mater. **20**, 6597–6599 (2008).

[118] "Orbital picture of bonding: orbital combinations, hybridization theory, and molecular orbitals," .

[119] F. P. Schafer, *Dye lasers* (Springer, 1990).

[120] C. Wells, *Introduction to molecular photochemistry* (Chapman and Hall Chemistry Textbook Series, New york, 1972).

[121] O. Svelto, *Principles of lasers*, vol. 1 (Plenunm Press, 2007).

[122] J. de Atkins, Peter; and Pauls, *Physical Chemistry* (Oxford University Press, Newyork, 2006), 8th ed.

[123] B. Valeur, *Molecular Fluorescence*, vol. 8 (Wiley-VHC Verlag GmbH, 2001).

[124] S. Forget, S. Chenais, D. Tondelier, B. Geffroy, I. Gozhyk, M. Lebental, and E. Ishow, "Red-emitting fluorescent organic light emitting diodes with low sensitivity to self-quenching," Journal of Applied Physics **108**, 1–6 (2010).

[125] S. J. Strickler and R. a. Berg, "Relationship between absorption intensity and fluorescence lifetime of molecules," The Journal of Chemical Physics **37**, 814 (1962).

[126] W. Holzer, a. Penzkofer, and T. Tsuboi, "Absorption and emission spectroscopic characterization of Ir(ppy)3," Chemical Physics **308**, 93–102 (2005).

[127] F. Schafer, "Dye Lasers," in "Topics in Applied Physics," (Springer Berlin, 1973), Vale 1973, p. 285, vol. 3, ed.

[128] C. Vannahme, M. B. k. Christiansen, T. Mappes, and A. Kristensen, "Optofluidic dye laser in a foil." Optics express **18**, 9280–9285 (2010).

[129] A. Kurian, N. a. George, B. Paul, V. P. N. Nampoori, and C. P. G. Vallabhan, "Studies on fluorescence efficiency and photodegradation of Rhodamine 6G doped PMMA using a dual beam thermal lens technique," Laser Chemistry **20**, 99–110 (2002).

[130] G. Kranzelbinder, G. and Leising, "Organic solid-state lasers," Report on Progress in Physics **63**, 729–762 (2000).

[131] J. Fischer, M; Georges, "Fluorescence quantum yield of rhodamine 6G in ethanol as a function of concentration using thermal lens spectrometry," Chemical Physics Letter **2614**, 0–3 (1996).

[132] C. Grivas and M. Pollnau, "Organic solid-state integrated amplifiers and lasers," Laser & Photonics Reviews **6**, 419–462 (2012).

[133] F. Ldpez, P. Ruiz, and I. Ldpez, "The fluorescence quenching mechanisms Rhodamine 6g in concentrated ethanolic solution," Journal of Photochemistry and Photobiology, A: Chemistry, **45**, 313–323 (1988).

[134] V. T. J, *Laser Electrodynamics*, vol. 13 (Prentice-Hall, 1995), 3rd ed.

[135] M. M. Mazumder, G. Chen, R. K. Chang, and J. B. Gillespie, "Wavelength shifts of dye lasing in microdroplets: effect of absorption change." Optics letters **20**, 878–880 (1995).

[136] H.-J. Moon, Y.-T. Chough, J. B. Kim, K. An, J. Yi, and J. Lee, "Cavity-Q-driven spectral shift in a cylindrical whispering-gallery-mode microcavity laser," Applied Physics Letters **76**, 3679–3681 (2000).

[137] L. Cerdan, A. Costela, I. Garcia-Moreno, O. Garcia, and R. Sastre, "Waveguides and quasi-waveguides based on pyrromethene 597-doped poly(methyl methacrylate)," Applied Physics B **97**, 73–83 (2009).

[138] J. B. Prieto, F. L. Arbeloa, V. M. Martinez, T. A. Lopez, and I. Arbeloa, "Photophysical Properties of the Pyrromethene 597 Dye : Solvent Effect," J. Phys. Chem. A **108**, 5504–5508 (2004).

[139] M. Ahmad, T. A. King, D.-k. Ko, B. Heon, and J. Lee, "Photostability of lasers based on pyrromethene 567 in liquid and solid-state host media," Optics Communications **203**, 327–334 (2002).

[140] A. Flatae, M. Burresi, H. Zeng, S. Nocentini, S. Wiegele, D. Wiersma, and H. Kalt, "Opto-Mechanically Tunable Polymeric Microlasers," in "CLEO: Applications and Technology," , vol. 26 (San Jose, California United States, 2014), vol. 26, pp. 1–2.

[141] B. Clough and A. Blumstein, "Structure and thermal expansion of some polymers with mesomorphic ordering," Macromolecules **9**, 123–127 (1976).

[142] H. Baumgaertel, H., Franck, E. U., Gruenbein, W., Stegemeyer, *Liquid crystals* (Springer, New york, 1994).

[143] L. Demus, D.; Richter, *Textures of liquid crystals* (Leipzig, Germany, 1979), 2nd ed.

[144] D. Iqbal and M. Samiullah, "Photo-Responsive Shape-Memory and Shape-Changing Liquid-Crystal Polymer Networks," Materials **6**, 116–142 (2013).

[145] V. P. Shibaev, N. A. Plate, Y. A. S. Freidzon, and P. Chemistry, "Thermotropic liquid crystalline polymers . I . Cholesterol-containing polymers and copolymers," Journal of Polymer Science **17**, 1655–1670 (1979).

[146] S. Chandrasekhar, *Liquid crystals* (Cambridge University Press, 1993), 2nd ed.

[147] J. Stoehr, M. G. Samant, A. Cossy-Favre, J. Diaz, Y. Momoi, S. Odahara, and T. Nagata, "Microscopic origin of liquid crystal alignment on rubbed polymer surfaces," Macromolecules **31**, 1942–1946 (1998).

[148] S. Wu, C.-S. Wu, M. Warenghem, and M. Ismaili, "Refractive index dispersions of liquid crystals," Optical Engineering **32**, 1775–1780 (1993).

[149] X. J. Wang, "Theoretical description of nematic polymers, networks and gels," Prog. Polym. Sci., **22**, 735–764 (1997).

[150] E. M. Terentjev, "Liquid-crystalline elastomers," J. Phys.: Condens. Matter **239** (1999).

[151] H. R. Brand, H. Pleiner, and P. Martinoty, "Selected macroscopic properties of liquid crystalline elastomers," Soft Matter **2**, 182–189 (2006).

[152] J. Wei and Y. Yu, "Photodeformable polymer gels and crosslinked liquid-crystalline polymers," Soft Matter **8**, 8050–8059 (2012).

[153] C. Ohm, M. Brehmer, and R. Zentel, "Liquid crystalline elastomers as actuators and sensors." Advanced materials **22**, 3366–3387 (2010).

[154] P. De Gennes, "Réflexions sur un type de polymères nématiques," C. R. Acad. Sci. B **281**, 101–103 (1995).

[155] J. Kiipfec and H. Finkelrnann, "Nematic liquid single crystal elastomers," Makromol. Chem., Rapid Commun **726**, 717–726 (1991).

[156] H. Finkelmann and G. Rehage, "Investigations on liquid crystalline polysiloxanes, 1 synthesis and characterization of linear polymers," Makromol. Chem., Rapid Commun. **4**, 31–34 (1980).

References

[157] A. Komp and H. Finkelmann, "A new type of macroscopically oriented smectic-A liquid crystal elastomer," Macromolecular Rapid Communications **28**, 55–62 (2007).

[158] M. Petr and P. T. Hammond, "Room temperature rapid photoresponsive azobenzene side chain liquid crystal polymer," Macromolecules **44**, 8880–8885 (2011).

[159] B. Donnio, H. Wermter, and H. Finkelmann, "A Simple and versatile synthetic route for the preparation of main-chain, liquid-crystalline elastomers," Macromolecules **33**, 7724–7729 (2000).

[160] Y. Xia, R. Verduzco, R. H. Grubbs, and J. a. Kornfield, "Well-defined liquid crystal gels from telechelic polymers." Journal of the American Chemical Society **130**, 1735–1740 (2008).

[161] J. Naciri, A. Srinivasan, H. Jeon, N. Nikolov, P. Keller, and B. R. Ratna, "Nematic elastomer fiber actuator," Macromolecules **36**, 8499–8505 (2003).

[162] X. Li, R. Wen, Y. Zhang, L. Zhu, B. Zhang, and H. Zhang, "Photoresponsive side-chain liquid crystalline polymers with an easily cross-linkable azobenzene mesogen," Journal of Materials Chemistry **19**, 236–245 (2009).

[163] R. Zentel, G. F. Schmidt, J. Meyer, and M. Benalia, "X-ray investigations of linear and cross-linked liquid-crystalline main chain and combined polymers," Liquid Crystals **2**, 651–664 (1987).

[164] A. Komp, J. Rühe, and H. Finkelmann, "A versatile preparation route for thin free-standing liquid single crystal elastomers," Macromolecular Rapid Communications **26**, 813–818 (2005).

[165] O. Prucker, C. A. Naumann, W. Knoll, and C. W. Frank, "Photochemical attachment of polymer films to solid surfaces via monolayers of benzophenone derivatives," J. Am. Chem. Soc. **121**, 8766–8770 (1999).

[166] P. Beyer, L. Braun, and R. Zentel, "(Photo) crosslinkable Smectic LC Main-Chain Polymers," Macromol. Chem. Phys. **208**, 2439–2448 (2007).

[167] M. Lavric, "Liquid crystal elastomers," Tech. Rep. december, University of Ljubljana, Faculty of Mathematics and Physics (2011).

[168] T. I. Yanlei Yu, Makoto Nakano, "Directed bending of a polymer film by light," Nature **425**, 145 (2003).

[169] C. J. Barrett, J.-i. Mamiya, K. G. Yager, and T. Ikeda, "Photo-mechanical effects in azobenzene-containing soft materials," Soft Matter **3**, 1249–1261 (2007).

[170] H. Zeng, D. Martella, P. Wasylczyk, G. Cerretti, J.-C. G. Lavocat, C.-H. Ho, C. Parmeggiani, and D. S. Wiersma, "High-resolution 3D direct laser writing for liquid-crystalline elastomer microstructures." Advanced materials **26**, 2319–2322 (2014).

[171] S. Maruo and J. Fourkas, "Recent progress in multiphoton microfabrication," Laser & Photonics Review **2**, 100–111 (2008).

[172] G. von Freymann, A. Ledermann, M. Thiel, I. Staude, S. Essig, K. Busch, and M. Wegener, "Three-dimensional nanostructures for photonics," Advanced Functional Materials **20**, 1038–1052 (2010).

[173] M. Kondo, Y. Yu, and T. Ikeda, "How does the initial alignment of mesogens affect the photoinduced bending behavior of liquid-crystalline elastomers?" Angewandte Chemie **118**, 1406–1410 (2006).

[174] T. Ikeda, J.-i. Mamiya, and Y. Yu, "Photomechanics of liquid-crystalline elastomers and other polymers." Angewandte Chemie (International ed. in English) **46**, 506–528 (2007).

[175] A. Flatae, M. Burresi, H. Zeng, S. Nocentini, S. Wiegele, H. Kalt, and D. Wiersma, "Optically controlled elastic microcavities," Submitted to - Light: Science & Applications (2014).

Acknowledgements

This work was mainly performed at the Institute of Applied Physics (APH) at the Karlsruhe Institute of Technology (KIT) (Karlsruhe, Germany) (in the semiconductor optics and photonics research group of Prof. Dr. Heinz Kalt). The work on photo-induced tuning of resonators was performed in close collaboration with European Laboratory for Non-Linear Spectroscopy (LENS), at the University of Florence (Florence, Italy) (in the optics of complex-systems research group of Prof. Dr. Diederik Wiersma). Without the help of the scientific staffs in these two excellent research groups, I could not have finished this work. Hence, I would like to express my gratitude to

- Prof. Dr. Heinz Kalt for giving me the chance to work on this beautiful and challenging area. Above all the scientific environment, time unlimited discussions and the freedom he gave to look into different directions, and wonderful supervision of my work and allowing me to grow as a research scientist.

- Prof. Dr. Diederik Wiersma for being optimistic and work hard to the collaboration work to integrate the field of photonics and smart materials (liquid crystal elastomers). And also work hard on organising the examination committee from LENS for my PhD defence.

- Dr. Matteo Buressi for supporting me in all aspects during my half year stay in LENS, and taking a huge role to get success in the lab. All the scientific discussions, new ideas, facilitating the lab activities and his professional trust in the work helped me a lot.

- Dr. Tobias Grossmann and Dr. Torsten Beck for their assistance, helpful discussions during the first two years of my PhD work. They gave my project a good ground and I benefited so much from them.

- Tobias Siegle for creating a friendly and stimulating working atmosphere with many fruitful discussions and correcting my thesis.

Assegid Mengistu Flatae

Karlsruher Institut für Technologie (KIT)
Institut für Angewandte Physik
Wolfgang-Gaede-Straße 1
76131 Karlsruhe

www.aph.kit.edu
assegid.flatae@kit.edu
asokamen1977@yahoo.com